Observational Signatures of Super-Eddington Accretors: Views from Radiation Hydrodynamics/Radiation Transfer Simulations

Takumi Ogawa

Department of Astronomy
Kyoto University

Supervisor: **Prof. Shin Mineshige**

This dissertation is submitted for the degree of
Doctor of Philosophy

January 2020

Acknowledgements

I would like to thank Prof. Mineshige who provided carefully considered feedback and valuable comments despite my slow-starting of writing this paper troubling him again (it was the same at the time of my master thesis). His tolerance allows me to study freely anything I am interested in. I would also like to thank my collaborators Ken Ohsuga, Hiroyuki Takahashi, and Tomohisa Kawashima (in the theoretical group of National Astronomical Observatory of Japan) whose opinions and information have helped me very much throughout the production of this study. They taught me everything from the ABC to the recent studies for numerical simulations. I'm glad them to help me also in future. Numerical computations were carried out on Cray XC50 at Center for Computational Astrophysics, National Astronomical Observatory of Japan. I am deeply grateful to my family. Though I have had caused them anxiety until now, I will become better than ever before.

Abstract

Super-Eddington accretors exhibit various kinds of unique observational signatures. In this thesis, we study their unique radiation properties by performing radiation hydrodynamic (RHD) and transfer simulations.

We first perform two-dimensional RHD simulations of super-Eddington accretion flow and the accompanying outflow to investigate how they will be observed from various viewing directions. We consider gas flow around a 10 $M_\odot$ black hole for a mass injection rates of $\dot{M}_{\rm inj}/\dot{M}_{\rm Edd} = 10^2$,$10^3$, and 10^4 (in the unit of $\dot{M}_{\rm Edd} \equiv L_{\rm Edd}/c^2$ with $L_{\rm Edd}$ and c being the Eddington luminosity and the speed of light, respectively), and solve gas dynamics and radiation transfer around the black hole, taking into account inverse-Compton scattering. We confirm a tendency that the higher the mass accretion rate is, the larger the relative importance of outflow over accretion flow becomes. The observational appearance of the super-Eddington flow is distinct, depending whether it is viewed from the edge-on direction or from the face-on direction. This is because nearly edge-on observers can only see the outer cooler ($\sim 10^6$ K) surface of the inner vertically inflated part of the flow. Observational properties are briefly discussed in the context of the ULXs, the extreme ULXs (E-ULXs), and the ultra-luminous supersoft sources (ULSs). We find that the extremely high luminosities of E-ULXs ($L \sim 10^{41}$ erg s^{-1}) can be explained when the flow onto the black hole with $\gtrsim 20M_\odot$ with a very high accretion rate, $\dot{m}_{\rm acc}$ ($\equiv \dot{M}_{\rm acc}/\dot{M}_{\rm Edd}$) $\gtrsim 10^3$, is observed from the nearly face-on direction. The high luminosity $\sim 10^{39}$ erg s^{-1} and the very soft blackbody-like spectra with temperatures around 0.1 keV, as are observed in the ULSs, can be explained, if the super-Eddington flow with $\dot{m}_{\rm acc} \sim 10^2 - 10^3$, is viewed from large viewing angles, $\theta \gtrsim 30^\circ$.

Next, we investigate the radiation fields around the super-Eddington accretion flow, in which multiple inverse-Compton scattering plays a principal role, by using a newly developed code of the Boltzmann radiation transfer in the Schwarzschild space-time. We apply this code to the post-processing spectral calculations based on the general relativistic, radiation-magnetohydrodynamic simulation data to obtain X-ray spectra seen from various viewing angles. The radiation fields are distinctively separated to a funnel region with an opening angle of $\sim 30^\circ$, which is full with hot (with gas temperature of $T > 10^8$ K), tenuous and high-velocity plasmas, and surrounding cooler (with $T \sim 10^7$ K) and optically thick outflow regions. Accordingly, there

is a clear tendency that the smaller the viewing angle is, the harder become the spectra. In particular, hard photons with several tens of keV are observable only by observers at the viewing angles less than $\sim 30^\circ$, consistent with past spectral studies based on the simulations. Further, we investigate how the spectra vary by a flare occurring at the innermost region, finding that the variation amplitude grows as the photon energy increases and that the harder photons emerge more quickly than softer photons. The observational implications on the long-term spectral variability of Ultra-Luminous X-ray sources are briefly discussed.

The work in this thesis is established by the numerical calculations, the analysis and code development of some parts of Boltzmann solver done by the author and the discussions with co-authors.

TABLE OF CONTENTS

CHAPTER 1

General Introduction

It is well known that numerous stars and galaxies shine the dark sky in the optical light. If we observe the sky with X-rays, however, we obtain a distant view of the universe; that is, we selectively see black holes both in binary systems and in galactic nuclei. In fact, accreting black holes are one of the most energetic phenomena in the universe. Since the large amount of energy is provided via release of gravitational potential energy of accreting gas, and since the accretion power is so enormous that it can give large impacts to the environments, it is very important to study the accretion, outflow, and radiative processes of black hole objects in order to understand the high energy phenomena in universe. Also for the formation of galaxies and large-scale structure in the universe, accreting black holes and its outflow seem to play an essential role since black holes centered in galaxies are fed and grow by gas accretion or merger of two galaxies.

In this chapter, we first overview the observational properties of the representative black hole objects, in general, and then introduce several types of super-Eddington, accretion sources and describe their generic features.

1.1 What are accreting black holes?

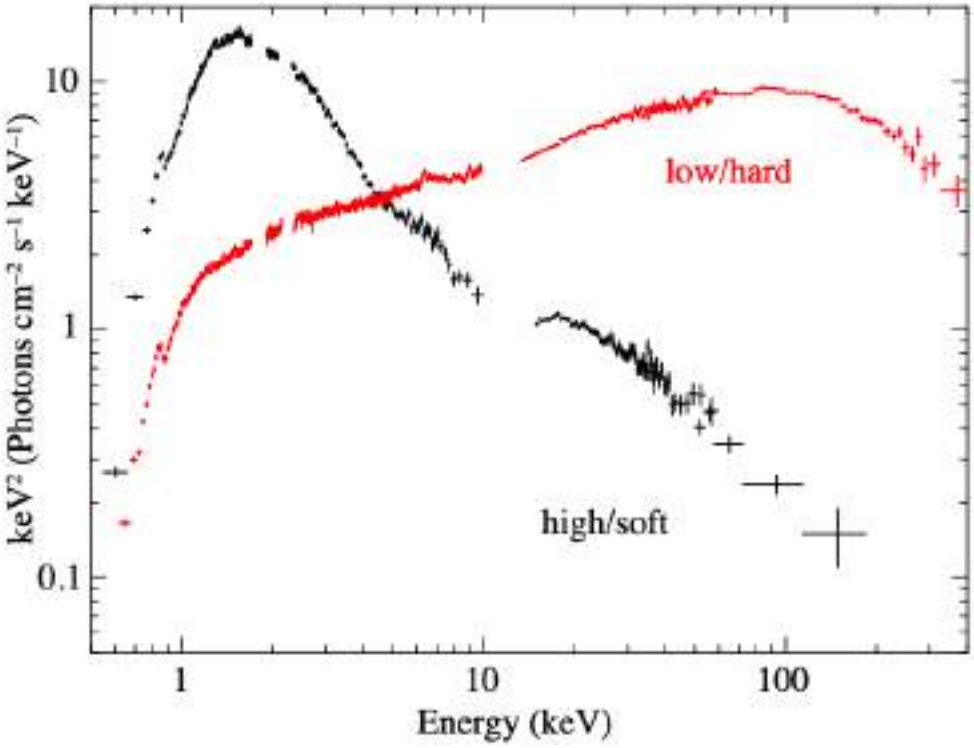

Fig. 1.1 X-ray spectra in the two different states of Cyg X-1. The spectrum from top left to bottom right in this figure shows the spectrum of high/soft state and from bottom left to top right shows low/hard state. In the high/soft state, the spectrum can be fitted well by blackbody with the temperature 1 keV. In the low/hard state, a power-law like spectrum is shown. (cited from Yamada et al. 2013)

There are two main classes of black hole objects known to date: stellar-mass black holes in binary systems and supermassive black holes at the center of galaxies. In addition, intermediate-mass black holes may exist, although they receive no wide consensus.

The former class called "black hole binaries" shows several spectral states: low/hard state with low luminosity ($\sim 10^{-3} - 10^{-2} L_{\rm Edd}$ where $L_{\rm Edd}$ is the Eddington luminosity) and with a hard, power-low like spectrum (see figure 1.1) , high/soft state with high luminosity ($\sim 10^{-2} - 10^{-1} L_{\rm Edd}$) and with a soft, blackbody-like spectrum (see figure 1.1; e.g., Tananbaum et al. 1972; Dolan et al. 1979) , very high state with very high luminosity and both characters of thermal soft blackbody and power-law (e.g., Miyamoto et al. 1993; van der Klis 1994; Gilfanov et al. 1993). These can be lain out in order of luminosity and also accretion rate (see figure 1.4; e.g., Esin et al. 1997). There is a theoretical model for each state:

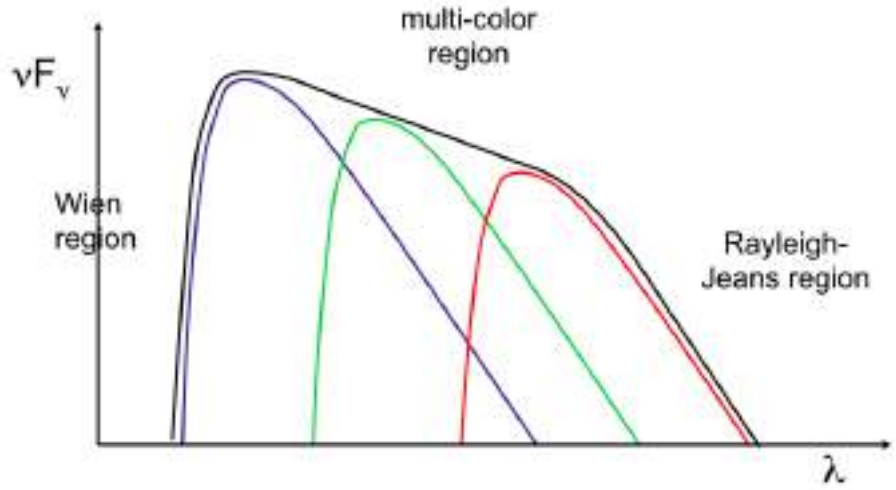

Fig. 1.2 The observed radiation of standard disk. This emission is the sum of the blackbody radiation from each radius r. The Wien region emission corresponds to the radiation from the innermost region of the disk, and The Rayleigh-Jeans region corresponds to the radiation from the outer region. The power-law index in multi-color region is dependent on the r-profile of effective temperature $T_{\rm eff}(r)$.

(a) high/soft state

The standard disk model is widely accepted to explain this state. This is the most well known model proposed by Shakura & Sunyaev (1973). Assuming that the disk is optically thick and geometrically thin and the process of angular momentum transport (which is always unknown and difficult to understand) is imposed on parameter α (which is now well-known as α-viscosity), they achieved the solution of disk properties. Because the effective temperature $T_{\rm eff}$ is different by the position r as

$$T_{\rm eff} \propto r^{-p} \tag{1.1}$$

from the standard disk model and the blackbody radiation is emitted from each position, the observed spectrum is the sum of the blackbody radiation from every position (so-called "multi-color blackbody"; see figure 1.2). The spectrum from standard disk tells us many information such as the temperature of innermost region (corresponding to the Wien region on figure 1.2) and the temperature of outer region (corresponding to the Rayleigh-Jeans region on figure 1.2) and the r-dependence of temperature p (corresponding to the steepness of the power-law in the multi-color region on figure 1.2). This model is reasonable to explain the high/soft state because (i)the high/soft state has higher luminosity (and simultaneously, has higher accretion rate) and thus the gas can be optically thick (ii) the high/soft state has spectrum explained well by multi-color blackbody emission.

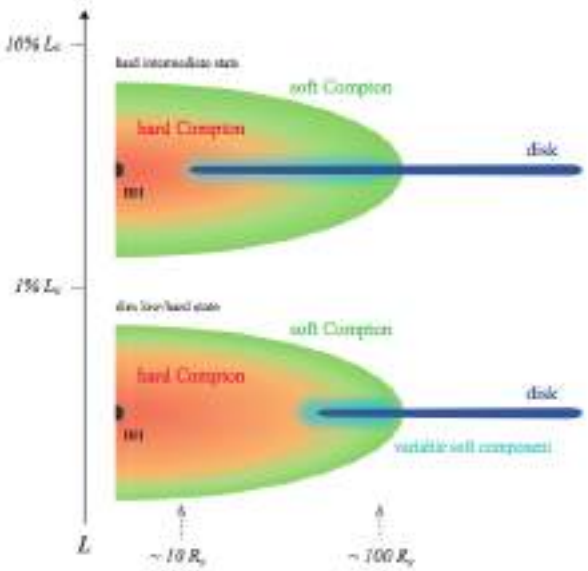

Fig. 1.3 Schematic diagram for RIAF. Near the black hole, the disk truncates and instead the gas with high temperature resides. The high energy gas induce Compton up-scattering to soft photons from the disk. $\dot{m}$ means the Eddington ratio $\dot{M}_{\rm acc}/\dot{M}_{\rm Edd}$.(cited from Yamada et al. 2013).

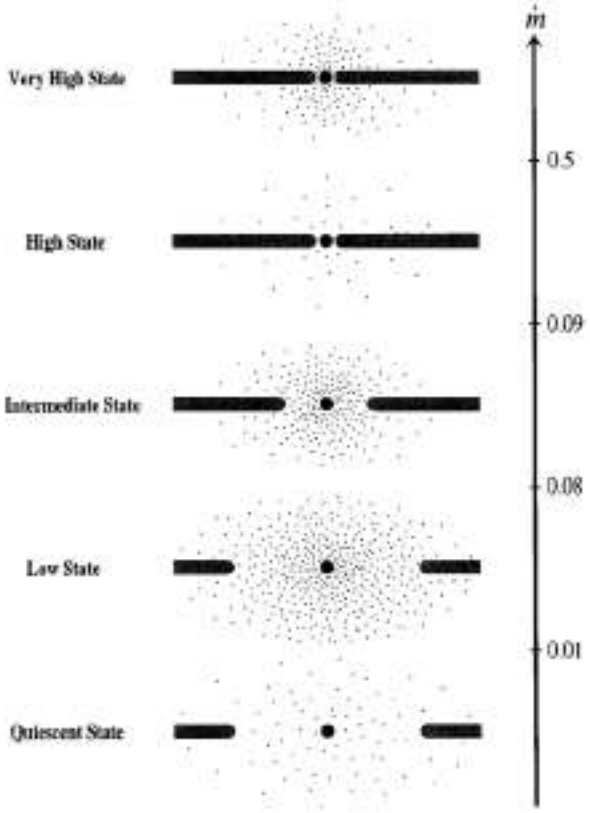

Fig. 1.4 The spectral states of black holes can be in order of accretion rate. (cited from Esin et al. 1997).

(b) low/hard state

The Radiation Inefficient Accretion Flow (RIAF) model is considered to proposed to explain the low/hard state (studied by Ichimaru 1977; Rees et al. 1982; Narayan & Yi 1994; Abramowicz et al. 1995). RIAF is radiation inefficient because the disk around the black hole is optically thin and geometrically thick due to its low accretion rate (see figure 1.3). The gas flow (no longer called "disk") has high temperature by viscous heating and therefore can produce non-thermal emission by Compton scattering in X-ray to gamma-ray and synchrotron emission in radio to optical bands. Since the flow at very low accretion rate is considered to be radiatively inefficient, and since the overall SED (spectral energy distribution) can roughly reproduced by the RIAF model, it is considered to be a reasonable model for describing the flow in the low/hard state (see figure 1.1).

1.2 Microquasars

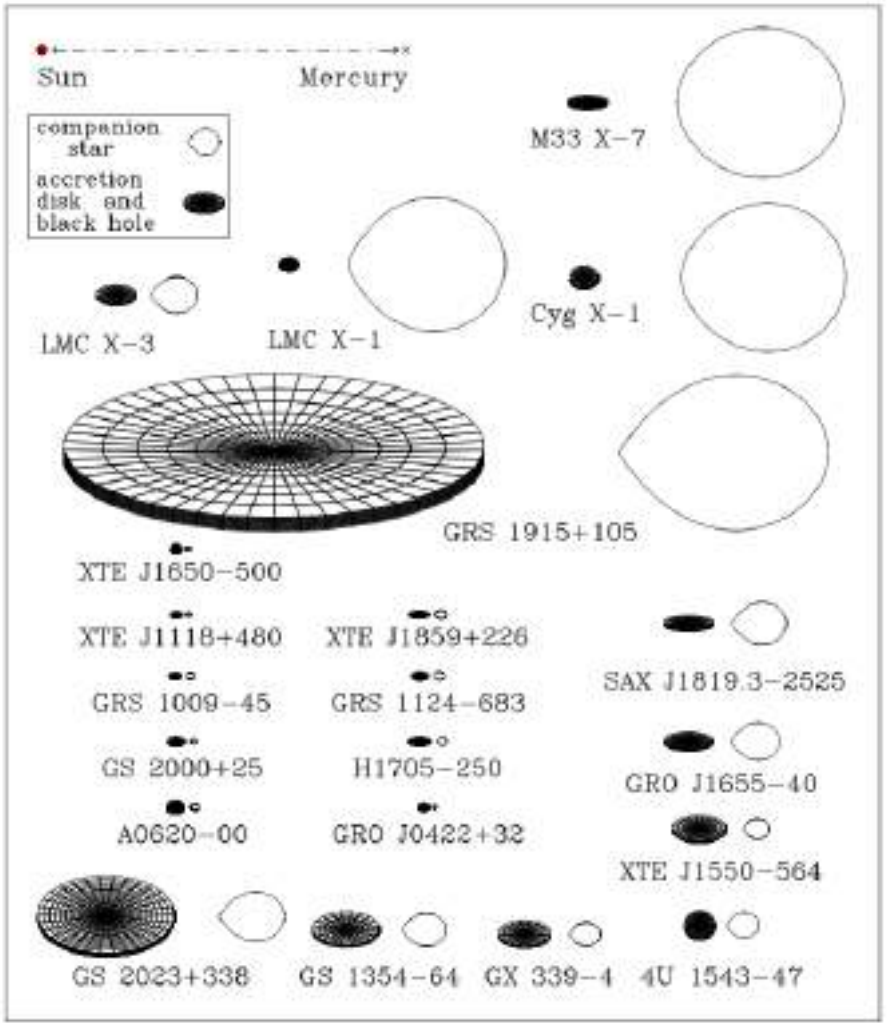

Fig. 1.5 Scale drawings of 21 black hole binaries. The size of the Sun and the Sun- Mercury distance (0.4 AU) are indicated at the top. The systems range in size from the giant GRS 1915+105 with an orbital period of 30.8 days to tiny XTE J1118+480 with an orbital period of 0.2 days. The shapes of the tidally distorted stars are accurately rendered, and the black hole is located at the center of the accretion disk (see key in inset). The inclination of the binary to our line of sight is indicated by the tilt of the accretion disk; an inclination angle of i = 0° corresponds to a system whose accretion disk lies in the plane of the sky and is viewed face on (e.g., i = 21° for 4U 1543–47 and i = 75° for SAX J1819.3-2525).

A microquasar is a subclass of galactic X-ray binaries and is characterized by intense emission from relativistic jets. Microquasar GRS1915+105 is one of the most well-studied source since not only it is a galactic X-ray binary and thus easy to observe but also has interisting features, such as very high luminosity and peculiar timing properties. It was shown to host a 10-18 $M_{\odot}$ black hole from the measurements of the binary motion (whose period $\approx$ 30.8 days) and thus to have the luminosity with about 0.2-1.2$L_{\rm Edd}$. Therefore GRS1915+105 is the place where the (mildly or marginally) super-Eddington accretion occurs (e.g., Greiner et al. 1996; Vilhu 1999; Vierdayanti et al. 2010). As results of analysis from its observations, GRS1915+105 has a very

large accretion disk (McClintock et al. 2011, see figure 1.5). This is also an evidence for the super-Eddington accretion.

1.3 ULXs (Ultra-Luminous X-ray sources)

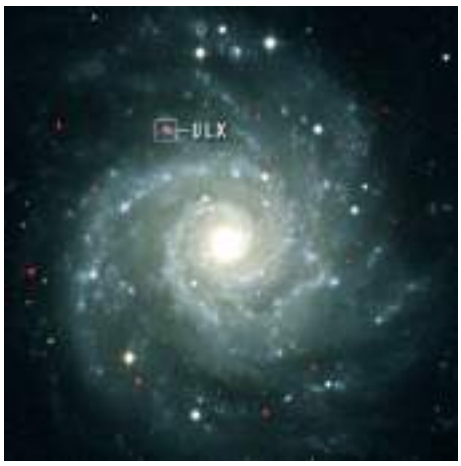

Fig. 1.6 The optical (grey) and X-ray (red) images of M74 galaxy (Credit: X-ray: NASA/CXC/U. of Michigan/J.Liu et al.). The ULX in the box is apart form the galactic center.

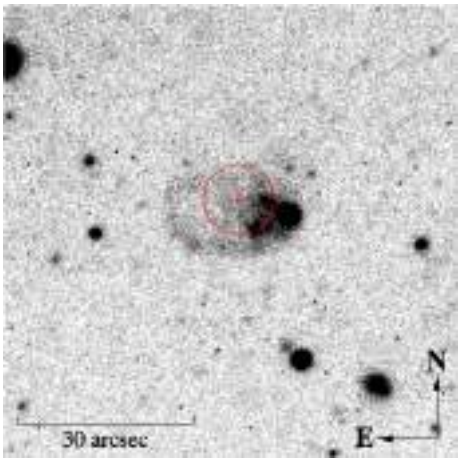

Fig. 1.7 Hα image of NGC 1313 X-2. The error circle of the variable ULX is centered on the center of the bubble nebula and marginally excludes a relatively bright stellar object at the western edge. (cited from figure 5 of Pakull & Mirioni 2002).

In recent years, objects called 'Ultra-Luminous X-ray Sources (ULXs)' have been successively discovered (Fabbiano et al. 1989; Makishima et al. 2000; Liu 2011; Walton et al. 2011). The ULX is a point X-ray source defined as it has very large X-ray luminosity ($L_X \gtrsim 10^{39}$erg s^{-1}; one of the brightest ULX (M101-X1) has the luminosity of $\sim 10^{41}$ergs^{-1} except for HLX-1) and its position is offset from the galactic center (see figure 1.6).

The spectral shape of ULXs looks strange (see figure 1.8 and figure 1.9) and can be divided into two groups: those that are consistent with a simple power-law, and those that are more complex (Makishima 2007). The latter mainly refers to a mild broad curvature (convex shape) over the whole band, a break or steepening above 2 keV, or a soft excess below 2 keV. A typical ULX spectral shape of the latter is sketched in figure 1.9. For this observational facts, ULXs are suspected to be in a new spectral state other than usual galactic X-ray binaries are (Gladstone et al. 2009; Kawashima et al. 2012).

Since the luminosity of ULX exceeds the Eddington luminosity of a stellar mass black hole (for $M_{\rm BH} = 10M_\odot$, the Eddington luminosity $L_{\rm Edd} \sim 10^{39}$erg s^{-1}), there are two most reasonable scenarios to explain this nature:(i) hosting a stellar mass black hole accreting at super-Eddington rate, (ii) hosting an intermediate mass black hole (IMBH) accreting at sub-Eddington rate.

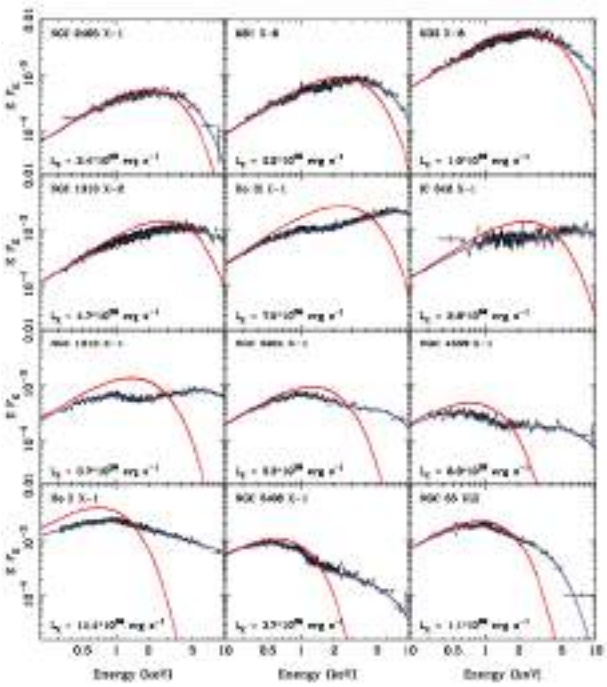

Fig. 1.8 Several examples of the spectrum of ULXs. The black is observational data, the red is only multi-color blackbody emission from its accretion disk, the blue is the reasonable model where Compton up-scattering soft photon from the disk by marginally optically thick ($\tau \sim 1$) colona is taken into account. (cited from Gladstone et al. 2009).

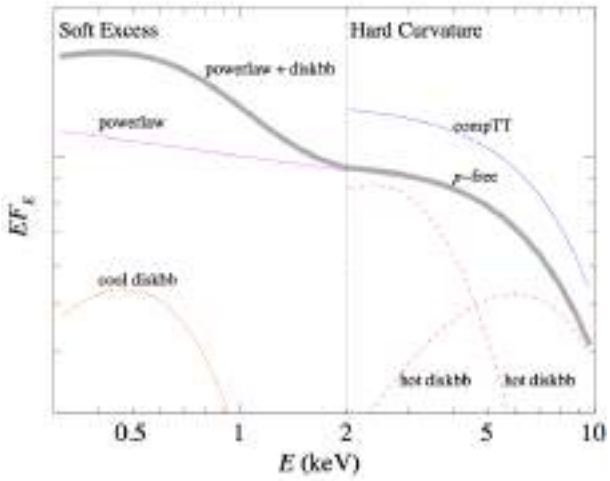

Fig. 1.9 A typical ULX spectral shape (grey) in 0.3-10 keV, with a soft excess below 2 keV and a hard curvature above 2 keV. The soft excess can be modeled by a cool thermal component, over the power-law extension of the hard component. A slim disk model (p-free) or a warm, thick Comptonization model can adequately fit the hard curvature.(cited from Feng & Soria 2011).

In the former case, the mechanism of large luminosity of ULXs can be explained by the large Eddington luminosity because of its large mass $M_{\rm BH} \gtrsim 10^2 M_\odot$. In observation, Some of ULXs show the quasi-periodic oscillation (QPO) whose frequency is about 1-100 mHz. Since there is a good correlation between black hole masses and these QPOs from observation of galactic X-ray binaries (but all of these X-ray binaries are stellar mass black hole binaries), Some of ULXs should host an inter-mediate mass black if the same correlation holds for ULXs. Physical explanation is the following: if this QPO is due to rotational motion around the inner-most stable circular orbit[1] (ISCO), the black hole mass $M_{\rm BH}$ is simply calculated from Keplarian rotation, resulting about $10^2 - 10^4 M_\odot$. Although, there is a difficulty in making such a black hole heavier than $100 M_\odot$. However, some people suggest that IMBH can be formed in dense globular clusters (Miller & Hamilton 2002) or in stellar evolution of very massive star in early universe (Crowther et al. 2010; Yusof et al. 2013).

[1] the position of ISCO is dependent on the black hole mass $M_{\rm BH}$ and its spin parameter a^*.

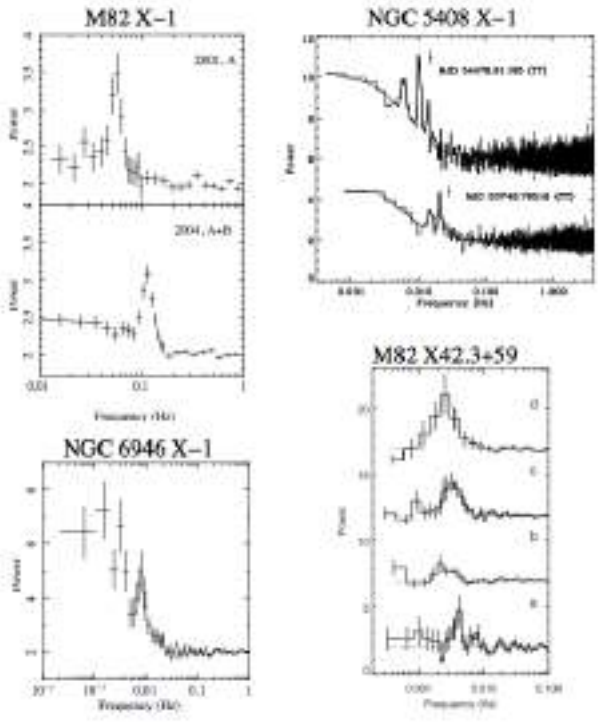

Fig. 1.10 Power spectra of four ULXs. There is a peak structure in each power spectrum which is so-called QPO (Quasi-Periodic Oscillation) around 1-100 mHz.(Feng & Soria 2011))

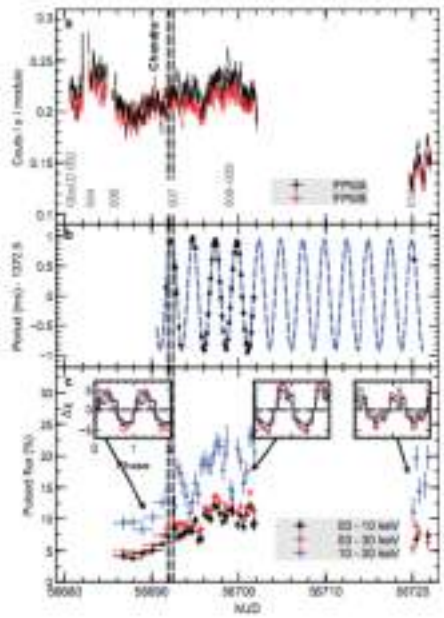

Fig. 1.11 The X-ray lightcurve and pulsations of M82X-2 from the region containing NuSTAR J095551+6940.8. Panel a: the background-subtracted 3-30 keV lightcurve. Panel b: detections of the pulse period (black points) fit using the best sinusoidal ephemeris (grey dashed line). The mean period is 1.37252266(12) seconds, with an orbital modulation period of 2.51784(6) days. Panel c shows the fraction of pulsed flux to total flux. The inserts show the pulse profile. (from Bachetti et al. 2014)

In the case of super-Eddington model, the mechanism of large luminosity of ULXs can be explained by the model of a super-Eddington accretion onto a stellar mass black hole (e.g., Watarai et al. 2001; Ohsuga et al. 2005, see Ohsuga & Mineshige (2014) for a concise review). Some robust observational evidence for super-Eddington accretion are discovered in recent year:

(1) Some of ULXs are confirmed to host stellar mass black holes.
Motch et al. (2014) investigated the mass function of P13 in the galaxy NGC 7793 from observation and concluded that the black hole mass is less than 15 $M_{\odot}$, and therefore a super-Eddington accretion onto a stellar mass black hole is confirmed.

(2) Discovery of a super-Eddington accreting neutron star
Bachetti et al. (2014) investigating M82 X-2 have demonstrated that there is a pulse component in its emission (see figure 1.11) and the period is decreasing (i.e. spinning up) , and thus concluded this ULX is a accreting neutron star system. This is the first evidence that the super-Eddington accretion is also possible at a neutron star accretor.

(3) ULX bubbles
A significant amounts of ULXs are surrounded by highly ionized nebula (so-called "ULX nebula"

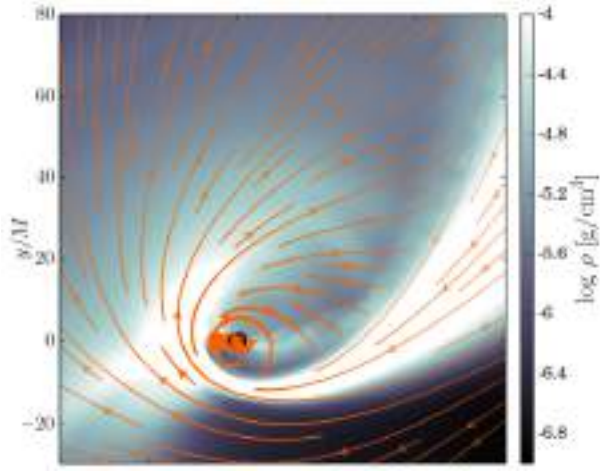

Fig. 1.12 A density contour map of the accretion disk of the fragment of a disrupted star at the simulation in Sądowski et al. (2015). The arrows show gas velocity.

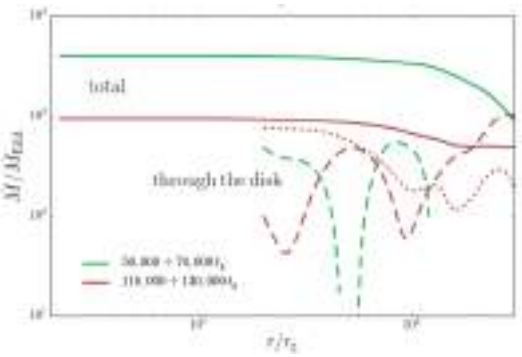

Fig. 1.13 Radial profiles of the mass accretion rate integrated over the total domain (solid lines) or only inside $\pi/4$ wedge near the equatorial plane (dashed lines). (From Sądowski et al. 2015)

or "ULX bubble", see figure 1.7; Pakull & Mirioni 2002, 2003; Soria et al. 2014) which is excited by kinetic shock and X-ray and therefore is evidence of a large amount of outflow and luminosity from the central accretor. Because the super-Eddington accretion induce very large amounts of outflow and luminosity, this observational fact may agree with the super-Eddington model for ULXs.

For this reason, the further study of properties of super-Eddington accretion flow is needed in order to understand the physics of ULXs.

1.4 Other candidates for super-Eddington accretion

The super-Eddington accretion may occur in phenomena other than ULXs as following:

(a) Tidal disruption events (TDEs)

(b) Ultra-luminous supersoft sources (ULSs)

(c) The formation of supermassive black hole in the early universe

(a) TDE

The TDE occurs when a star approaches a black hole (or super-massive black hole in ordinary case) close enough to disrupted by tidal force from central black hole. the fragments of disrupted star forms very massive disk ($\gtrsim 1M_{\odot}$) and cause super-Eddington accretion onto the central black hole. Several numerical simulations for TDE also confirms super-Eddington accretion (Cheng & Bogdanović 2014; Sądowski et al. 2015). For example, Sądowski et al. (2015) performed a general relativistic hydrodynamics (GRHD) simulation which solve the tidal disruption event consistently from a star approaching the black hole to accretion process by means of switching GR-SPH (Smoothed Particle Hydrodynamics)

code with GR-MHD code.

(b) ULS

ULS is a newer population of X-ray binary which has following properties:

- very high luminosity ($\sim 10^{39}\mathrm{ergs}^{-1}$; same order as the Eddington luminosity for $10M_\odot$)
- supersoft thermal spectrum $T \lesssim 0.1\mathrm{keV}$ (Di Stefano & Kong 2003)

Some of ULSs have blueshifted, broadline Hα emission in their spectra and thus there is a relativistic jet or outflow (Liu et al. 2015). Similar to the case of ULXs, since ULSs have very high luminosity around the Eddington luminosity for a stellar mass black hole, there are two theoretical models, one of which is sub-Eddington accretion onto an intermediate black hole, the other of which is super-Eddington accretion onto stellar mass black hole. Gu et al. (2016) proposes that a super-Eddington accretion disk viewed from a large inclination angle can be seen as a ULS (we will see later at §2.4.2).

(c) Formation of supermassive black holes

Considering the formation of the super-massive black hole in the early universe (for example, a super massive black hole with $M_{\mathrm{BH}} \sim 10^{10}M_\odot$ is found at $z \sim 6.4$ e.g., Wu et al. 2015), the existence of the epoch of the super-Eddington accretion is required to achieve its large mass. The reason is the following:

As a result of studies for the formation of the first stars (so-called Population Ⅲ star), the mass of first star is about 10^2-$10^3M_\odot$(Hirano et al. 2014; Susa et al. 2014) and then 10^2-10^3 black holes are formed by the pair instability at $z \sim 20$ (≈ 0.188 years old). Assuming the radiation efficiency is η and luminosity is fixed to L_{Edd}, the black hole mass at the time t is written as

$$M_{\mathrm{BH}}(t) = M_{\mathrm{seed}} \exp\left(\frac{1-\eta}{\eta}\frac{t}{0.45\mathrm{Gyr}}\right) \tag{1.2}$$

where M_{seed} is the black hole mass at $t = 0$. Substituting $M_{\mathrm{seed}} = 10^2M_\odot$,$\eta = 0.1$ and $M_{\mathrm{BH}} = 10^{10}$ (≈ 0.802 years old), we get the time needed to grow from $10^2M_\odot$ to $10^{10}M_\odot$ and resulting $t = 0.92\mathrm{Gyr}$. Since the growth at the Eddington rate can't reach the mass of supermassive black hole observed in the early universe, the super-Eddington accretion onto the seed black hole is needed.

Despite the importance of super-Eddington processes, its observational signatures have not been so well understood yet.

1.5 Past numerical studies of super-Eddington accretion flow

In order to study the super-Eddington accretion processes, the simulation with higher dimensions and radiative processes must be needed, because the accretion disk at the super-Eddington phase is a radiation pressure dominated and very fat disk. Further, multidimensional motion ,such as internal motion (convection) and significant outflow, are essential. So, we will introduce some of simulations studying super-Eddington accretion flow.

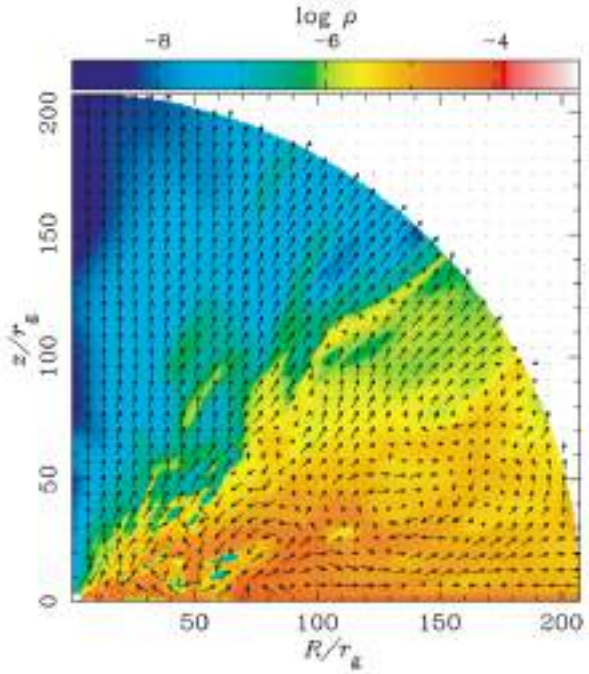

Fig. 1.14 Gas density contour map and gas velocity vector field map. At the origin, a black hole resides. (cited from Ohsuga et al. 2005)

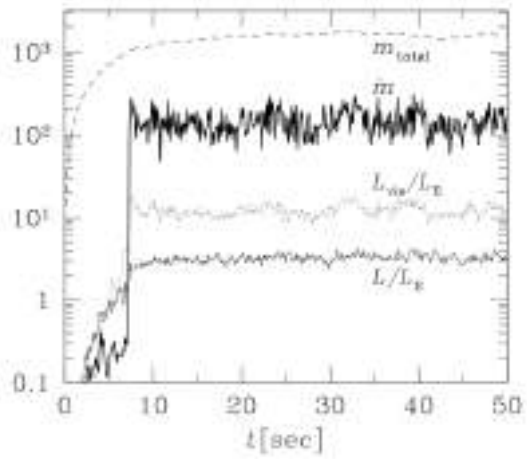

Fig. 1.15 time dependence of accretion rate onto the central black hole.

The first numerical study for super-Eddington accretion is in Ohsuga et al. (2005), where they performed axisymmetric 2D radiative hydrodynamics (RHD) simulations and revealed that super-Eddington accretion onto a black hole is possible (see figure 1.15) . Figure 1.14 shows density map and velocity vector map. A large convective region appears in the fat accretion disk and the board outflow region is shown near the outer region. The outflow is driven by radiation-pressure force and the outflow is considered to Compton up-scattering (=inverse Compton scattering) soft photons from the super-Eddington accretion disk. The summary of their revealing properties for super-Eddington accretion flow is the following:

- A geometrically and optically thick disk
- A large amount of strong outflow driven by the radiation-pressure force
- photon trapping effect[2]

[2]In the very optically thick accretion disk, since the diffusion velocity of photos are less than the accretion velocity, a large fraction of the photons generating in accretion disk accrete into the black hole together with matters.

- convective motion within the disk
- isotropic radiation flux (e.g., the luminosity from the face-on angle can exceeds the Eddington luminosity)

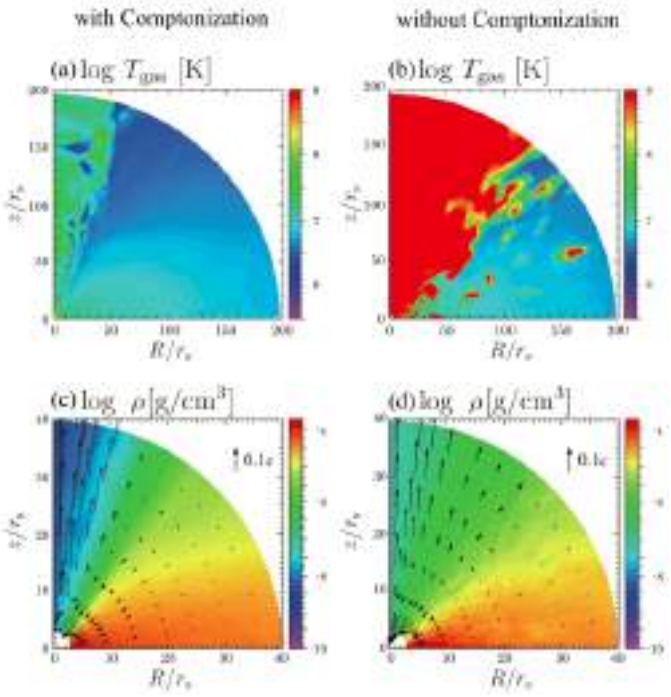

Fig. 1.16 Distribution of temperature (top) and mass density averaged over time(bottom). (Left) Model including Comptonization. (Right) Model without Comptonization. Arrows represent velocities of fluid motions.

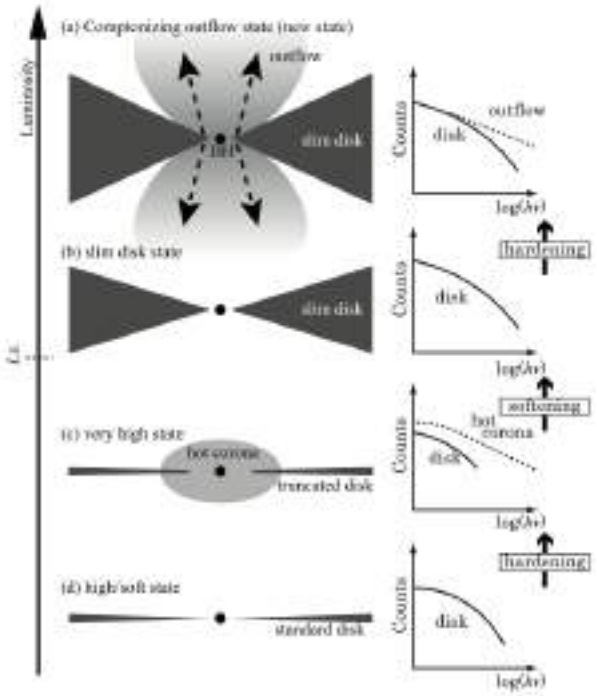

Fig. 1.17 Schematic pictures of the states of accretion disks. From top to bottom:(a)Comptonizing outflow state, which consists of super-Eddington accretion flows (i.e., slim disks) and Comptonizing outflows, (b) slim disk state, (c) very high state, and (d) high/soft state. The SED of the new state is harder than that of the slim disk state, because the new state includes a hot outflow which up-scatters seed photons from the underlying disk.

After Ohsuga et al 2005, another axisymmetric 2D RHD simulation including thermal Compton effects, which is supposed to be important because of large amounts of hot outflow from super-Eddington accretion flow, was performed in Kawashima et al. (2009) (see figure 1.16). They demonstrated that there appears a new hard spectral state at higher photon luminosities than that of the slim-disk state. In this state, as the photon luminosity increases, the photon index decreases and the fraction of the hard emission increases. Moreover, they said that the result of this simulation can explain the observed spectral hardening of the ULX NGC 1313 X-2 in its brightening phase, and thus supports the model of supercritical accretion onto stellar-mass black holes in this ULX. Another study for applying the spectrum of super-Eddington accreting black holes to that of ULXs was discussed in Kawashima et al. (2012). They computed the spectrum from super-Eddington accretion flow and its outflow by using Monte-Carlo method by post-processing the results of axisymmetric radiation hydrodynamic simulations, which

takes into account thermal/bulk Comptonization, free-free absorption and photon trapping, performed in Kawashima et al. (2012). They demonstrated that the spectrum of the emission from the super-Eddington accreting black hole can explain the spectrum of some of ULXs (see figure 1.18). The optically thick and cooler outflow surrounding the jet plays an important role for creating a characteristic double-peak like spectrum (usually said "roll over" around 5keV) of ULXs (see figure 1.19).

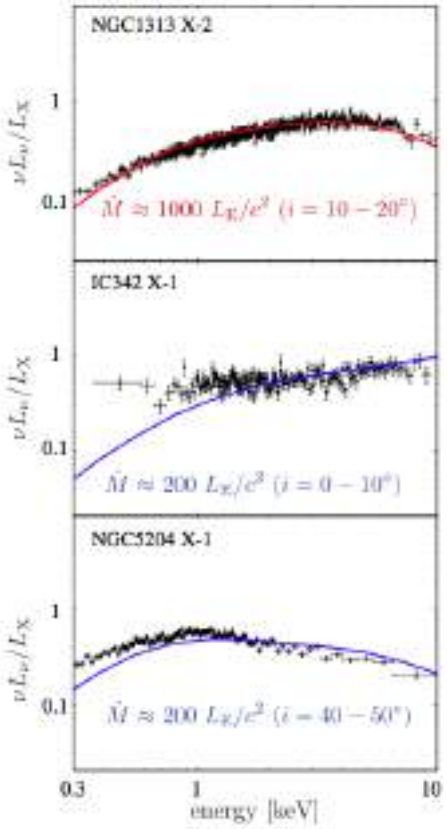

Fig. 1.18 Comparison of SEDs obtained from the radiation hydrodynamic simulations (performed in Kawashima et al. 2012) with those of ULXs. The black is the data of ULXs and the blue is the result of simulation.These are well fitting to observation. (cited form Kawashima et al. 2012)

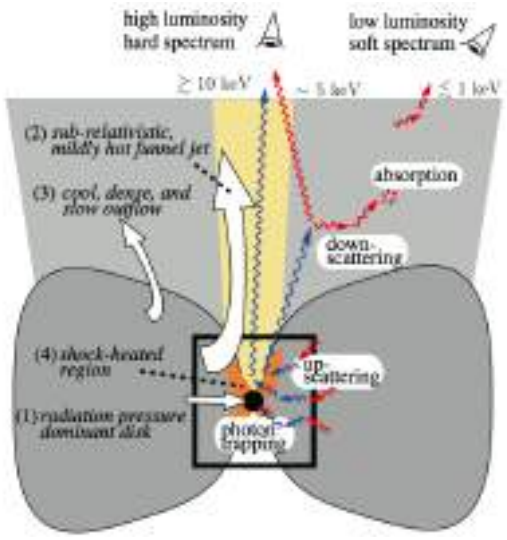

Fig. 1.19 Schematic picture of a supercritical accretion flow consisting of (1) a radiation pressure dominant accretion disk, (2) a sub-relativistic, mildly hot funnel jet, (3) a cool, dense, and slow outflow, and (4) a shock-heated region. This show the overall structure of a supercritical accretion flow obtained by our simulations.The shock-heated regions are formed because the accreting gas near the rotation axis is bounced by the centrifugal barrier. Photons are upscattered by electron scatterings in the converging inflow (bulk Compton scattering) and the thermal Comptonization by hot electrons in the shock-heated region.

There is another interesting study for super-Eddington accretion. Takeuchi et al. (2013) performed axisymmetric two-dimensional Radiation MagnetoHydroDynamics (RMHD) simulations of super-Eddington accretion flow with high resolution and large simulation domain as never before. That was the time of the discovery of the clumpy outflow. The clumpy structure appears in the outer region where the radiation pressure force overcomes gravity (see figure 1.20). The mechanism of forming clumpy structure is the radiative Rayleigh-Taylor instability

(RT) where the strong radiation force instead of gravity in usual RT works the density profile thiner toward outer direction (Takeuchi et al. 2014, see figure 1.21).

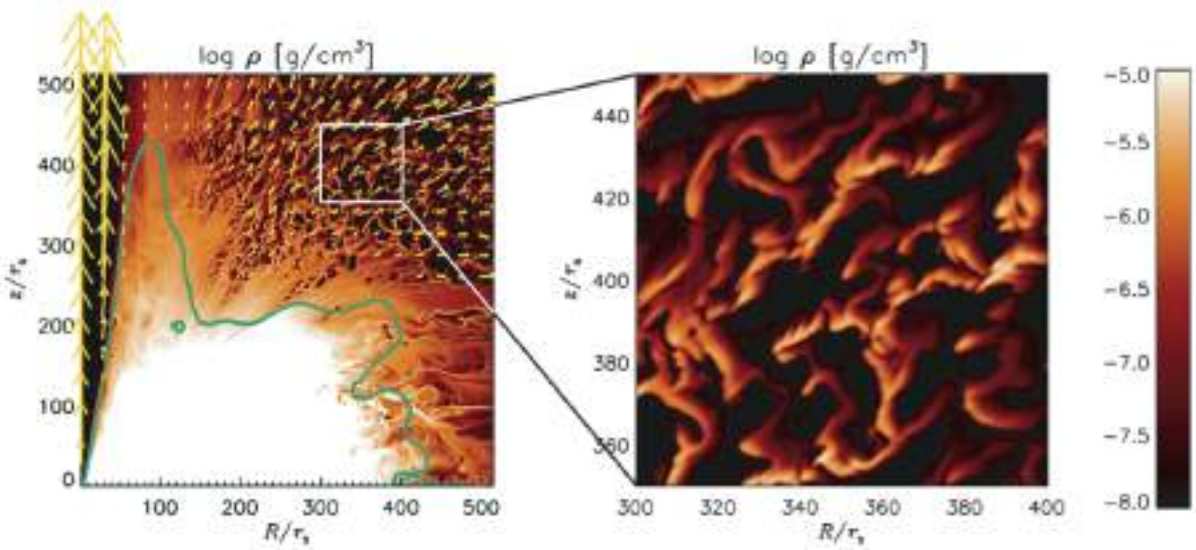

Fig. 1.20 A snapshot of density contour map. The yellow vector is gas velocity vector plotted in the case of its velocity greater than escape velocity and the green line shows the position where the radiation-pressure force (toward outer direction) equals to the gravitational force (toward inner direction). We can see the clumpy structure outside the green line. (cited from Takeuchi et al. 2013)

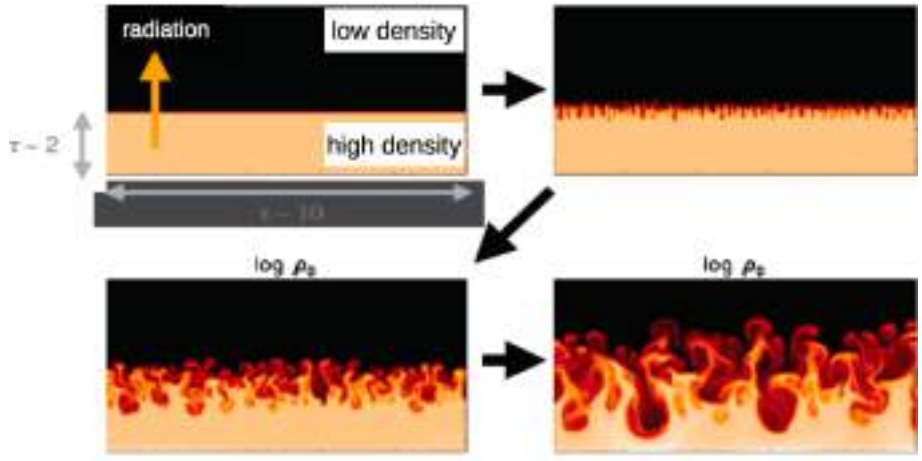

Fig. 1.21 Time variance of density map in radiative Rayleigh-Taylor instability. The strong radiation upward is instead of gravity in usual Rayleigh-Taylor instability. (modified figure in Takeuchi et al. 2014).

1.6 Importance of Comptonization

How to accurately solve radiation transfer equations? This is one of the most fundamental issues in astrophysics, since we can obtain rich information mainly via detecting electro-magnetic wave radiation from astrophysical objects. Radiation is, however, not only means of observations but it can also transport energy and momentum, thereby being able to give significant impact on

the environment around a radiating source and even on the media inside the source. Radiation can heat up gas (if absorbed and/or Compton up-scattered) or cool down gas (if Compton down-scattered). It can also push material by asserting radiation-pressure force or line-driven force. Good examples are stellar wind, which affects stellar evolution, and accretion disk outflow, which controls disk activities, and so on.

Let us focus on the cases of accretion disks around black holes. Then we soon notice that it is impossible to discuss X-ray emission properties without Comptonization. Seed photons emitted from a cool and dense disk body are up-scattered by hot electrons existing around the disk to produce characteristic spectral features, such as hard power-law components and/or spectral humps. Two main sites are known to produce hard X-rays via inverse Compton scattering: low accretion-rate flow or the so-called radiatively inefficient accretion flow (RIAF, see chapter 9 in Kato et al. (2008) and references therein), and accretion disk coronae above and below sub-Eddington flow (see e.g., Liang & Nolan 1984; Haardt & Maraschi 1991; Kato et al. 2008). In both cases, the system has high temperature (corresponding to photon energy of ~ 100 keV) ionized gases around the central object. The Thomson optical depth is typically $\tau_{\rm es} \sim 1$ and the Compton y-parameter is on the order of unity.

We wish to note that Comptonization should be critical also in the super-Eddington accretors, since the strong radiation from the disk can blow off a large amount of gas to form mildly relativistic, uncollimated hot outflow so that the photons emitted from the underlying disk body can experience inverse-Compton scattering when passing through the hot outflow (Kawashima et al. 2009). By contrast with the two sites mentioned above (i.e., RIAFs and disk coronae), the Comptonizing outflow is characterized by (relatively) low temperature ($\sim$ a few keV), optically thick ($\tau_{\rm es} \sim 2-5$) Comptonization (e.g., Kitaki et al. 2017). Therefore, multiple scatterings dominate over single scatterings there.

1.7 Goal of this thesis

As we have reviewed above, there are plenty of works done in the field of super-Eddington accretion flow and outflow. However, systematic study of such flow for a variety of mass injection rates has never been attempted. In this thesis, we hence examine how the results depend on the mass injection rates. We wish to address the following questions:

- How large can the accretion rate and luminosity grow?
- How do the observable quantities (luminosity, kinetic luminosity, outflow rate, etc) depend on the accretion rate?
- How do the spectral properties vary with inclination angles?
- What kinds of (long-term and short-term) spectral variations are expected?

To answer to these questions, we perform two-dimensional axisymmetric radiation hydrodynamic/transfer simulations by taking into account thermal Compton scattering effects, and discuss the unique properties of super-Eddington accretion flow.

The plan of this thesis is as follows. In next chapter (chapter 2) we discuss how the super-Eddington accretor looks like when changing the viewing angles and accretion rates via

(grey) RHD simualtions. After summarizing possible links between super-Eddington accretors and ultraluminous sources, we discuss spectral properties (such as observational images and time variabilities) by using a newly developed Boltzmann radiation solver in chapter 3. In chapter 4, we summarize the conclusions and discuss remaining issues of this thesis.

CHAPTER 2

RADIATION HYDRODYNAMIC SIMULATIONS OF A SUPER-EDDINGTON ACCRETOR AS A MODEL FOR ULTRA-LUMINOUS SOURCES

2.1 Introduction to Chapter 2

Accreting black holes are known to exhibit various luminous and energetic phenomena in the universe. This is made possible, because they extract enormous energy from accreting material and/or utilize the rotation energy of the black holes themselves. Among various types of astrophysical black holes super-Eddington (or super-critical) accretors have attracted much attention recently, since they can produce extremely large luminosities and strong outflow so that their power should give great impacts to their environments. Super-Eddington accretors are thus suggested to play essential roles in yielding various active phenomena e.g., relativistic baryon jets and huge ionized nebulae. It is, hence, of great importance to investigate the basic processes, as well as their observational signatures, of the super-Eddington accretion flow and associated outflow. Such study will be beneficial also for understanding how supermassive black holes have grown up and what influence they should have given to their host galaxies.

As mentioned in Chapter 1, that robust observational evidences supporting the super-Eddington scenario for the ULXs are accumulated in recent years. Motch et al. (2014), for example, investigate ULX P13, which is observationally suggested to have 64 day period binary motion. They modeled the strong optical and UV modulations due to X-ray heating of the B9Ia donor star and conclude that this ULX hosts a stellar mass black hole whose mass is less than 15 $M_{\odot}$. Since the X-ray luminosity of P13 ranges from 1.6×10^{39} erg s^{-1} to 4×10^{39} erg s^{-1}, P13 is suggested to be a super-Eddington source. Moreover, Bachetti et al. (2014) investigating M82 X-2 have demonstrated that this ULX is emitting the pulse component whose period is about 1.37s and thus it hosts a neutron star accretor. Because the luminosity of this ULX ($L_{\rm X} \gtrsim 10^{39}$ erg s^{-1}) is much greater than Eddington luminosity of a neutron star

($L_{\rm Edd} \lesssim 10^{38.5}$ erg s^{-1} for the mass of a neutron star, $M_{\rm NS} < 3M_\odot$), the central accretor must be super-Eddington.

In addition to ULXs, we also pay particular attention to another type of enigmatic objects called ultra-luminous supersoft sources (ULSs) which were recently discovered and are extensively studied (Di Stefano & Kong 2003; Kong et al. 2004; Liu 2008). They produce very high X-ray luminosities ($L_{\rm X} \gtrsim 10^{39}$erg s^{-1}) similarly to the ULXs, but nevertheless their X-ray spectra are very soft and is thus distinct from those of the ULXs. More precisely, they are characterized by exhibiting blackbody-like spectra whose blackbody temperature is less than 0.1 keV (Di Stefano & Kong 2003). Because of their very high luminosities (above the Eddington luminosity of stellar mass black holes), ULSs are also considered to be either super-Eddington sources hosting stellar mass black holes or sub-Eddington sources hosting intermediate mass black holes. Urquhart & Soria (2016) propose a unified scheme, in which the ULSs are super-Eddington accretion systems accreting at high Eddington rate about $10^3\dot{M}_{\rm Edd}$ viewed from large polar angles of 20-90° (see also Gu et al. 2016).

In view of such diversity in possible super-Eddington objects we perform more extensive and systematic study of super-Eddington accretors to clarify their observational signatures for a variety of mass accretion rates and of viewing angles.

Multi-dimensional simulations are indispensable, since the super-Eddington accretion disk is known to be very fat and full of multi-dimensional gas motion, such as internal circulation and strong outflow. Radiation hydrodynamic (RHD) simulations are also needed, since intense interactions between gas and radiation are essential. As a first step of systematic study, we perform simulations in the Newtonian dynamics in the present study to discuss the overall properties of the super-Eddington accretion flow, such as accretion rate, outflow rate, luminosity, the impact onto circumstances, and so on. We take into account thermal Compton scattering effects, since the optically thick outflow in the super-Eddington accretion phase suffers thermal Comptonization (Kawashima et al. 2009). More details of numerical methods and calculated models are explained in the next section (§2.2). We then show our results in §2.3. The last section in this chapter is devoted to discussion.

2.2 Methods of calculations and calculated models

In the present study we use the two dimensional axisymmetric RHD code developed by Kawashima et al. (2009). We inject mass to an almost empty region around a black hole (with a mass of $M_{\rm BH} = 10M_\odot$) from the outer boundary at a constant rate ($\dot{M}_{\rm inj}$) and solve how gas accretes onto the central black hole and how much radiation is produced and propagated to reach distant observers.

2.2.1 Basic Equation

We adopt the polar coordinates (r, θ, φ) (where r is the radius from the central black hole, θ is polar angle from the rotational axis of the disk and φ is the azimuthal angle but this component vanishes because of the axisymmetricity) with the origin being at the central black hole and $\theta = \pi/2$ being the equatorial plane, on which mass is injected (see §2.2.2). The α viscosity

prescription and the Flux Limited Diffusion (FLD) approximation (Levermore & Pomraning 1981) are adopted for solving radiation transfer. Further, thermal Compton effects are taken into account in the energy equation. The general relativistic effects are incorporated by adopting the Paczyński-Wiita potential $\Phi_{\rm PW} = -GM_{\rm BH}/(r - r_{\rm S})$, where $r_{\rm S}$ is the Schwarzschild radius of the central black hole. By the assumption of axisymmetry, we set $\partial/\partial\varphi = 0$, while retaining the φ-components of the velocity and the viscous force. All other φ-components of vector quantities are set to zero.

The basic equations are then given by

$$\partial_t \rho + \nabla \cdot (\rho \boldsymbol{v}) = 0 \tag{2.1}$$

$$\partial_t \rho v_r + \nabla \cdot (\rho v_r \boldsymbol{v}) = -\partial_r p + \rho \left(\frac{v_\varphi^2}{r} + \frac{v_\theta^2}{r} - \frac{GM}{(r - r_{\rm S})^2} \right) + f_r \tag{2.2}$$

$$\partial_t (\rho r v_\theta) + \nabla \cdot (\rho r v_\theta \boldsymbol{v}) = -\partial_\theta p + \rho v_\varphi^2 \cot\theta + r f_\theta \tag{2.3}$$

$$\partial_t (\rho r v_\varphi \sin\theta) + \nabla \cdot (\rho r v_\varphi \boldsymbol{v} \sin\theta) = r q_\varphi \sin\theta \tag{2.4}$$

$$\partial_t e + \nabla \cdot (e\boldsymbol{v}) = -p\nabla \cdot \boldsymbol{v} - 4\kappa\pi \mathrm{B} + c\kappa E_0 + \Phi_{\rm vis} + \Gamma_{\rm Comp} \tag{2.5}$$

$$\partial_t E_0 + \nabla \cdot (E_0 \boldsymbol{v}) = -\nabla \cdot \boldsymbol{F_0} - \nabla \boldsymbol{v} : \boldsymbol{P_0} + 4\kappa\pi \mathrm{B} - c\kappa E_0 - \Gamma_{\rm Comp} \tag{2.6}$$

where ρ, $\boldsymbol{v}$= $(v_r, v_\theta, v_\varphi)$, p, e and κ, are the mass density, velocity of gas, gas pressure, the internal energy density of gas, (Rosseland-mean) absorption opacity measured in the fluid co-moving frame, respectively, ∂_t, ∂_r, ∂_θ, and ∂_φ are the differential operators with respect to t, r, θ, and φ, respectively, and $\nabla = (\partial_x, \partial_y, \partial_z)$ is the natural vector differential operator, q_φ is the viscous force calculated based on the α viscosity model, $\boldsymbol{f}$, E_0, $\boldsymbol{F_0}$ and $\boldsymbol{P_0}$ are the radiation force, the radiation energy density, the radiation flux, and the radiative stress tensor, respectively. The subscript 0 indicates the value measured in the fluid co-moving frame. The radiation force $\boldsymbol{f}$ is calculated by using the total opacity $\chi = \kappa + \rho\sigma_{\rm T}/m_{\rm p}$ (with $\sigma_{\rm T}$ being the cross section of Thomson scattering and $m_{\rm p}$ being the proton mass) as

$$\boldsymbol{f} = \frac{\chi}{c} \boldsymbol{F}_0 \tag{2.7}$$

and $\boldsymbol{F_0}, \boldsymbol{P_0}$ can be described by the radiation energy density E_0 and its first derivative from the FLD approximation. The quantities $\mathrm{B}, \Phi_{\rm vis}$, and $\Gamma_{\rm Comp}$ are Planck function, the heating rate by viscous dissipation, and the heating rate by thermal Compton scattering, respectively. The term $\Gamma_{\rm Comp}$ is described as

$$\Gamma_{\rm Comp} = 4\pi\sigma_{\rm T} c \frac{k_{\rm B}(T_{\rm rad} - T_{\rm gas})}{m_{\rm e} c^2} \left(\frac{\rho}{m_{\rm p}} \right) E_0, \tag{2.8}$$

where $k_{\rm B}$,$m_{\rm e}$, $T_{\rm gas}$, and $T_{\rm rad}[\equiv (E_0/a)^{1/4}]$ (a is the radiation constant) are the Boltzmann constant, the electron mass, gas temperature, and radiation temperature, respectively. Finally, we need the equation of state to close the set of the basic equations: $p = (\gamma - 1)e$ with $\gamma = 5/3$ being the specific heat ratio.

2.2.2 Setup, Initial and Boundary Conditions

The simulation domain has the shape of a quarter circle on the $r-\theta$ plane set by $2r_{\rm S} \leq r \leq r_{\rm out}$ and $0 \leq \theta < \pi/2$. As to the boundary conditions, we set as follows: The outer boundary at $r = r_{\rm out}$ and $\theta < 0.45\pi$ is an outflow boundary where the radiation and gases can go through freely and any information never goes into computational domain. The outer boundary at $r = r_{\rm out}$ and $\theta > 0.45\pi$ is the boundary from which we inject gas into computational domain at the constant rate $\dot{M}_{\rm inj}$ with a fixed value of angular momentum mentioned later. Finally, the inner boundary at $r = 2r_{\rm S}$ is an absorbing boundary with a damping layer where the physical quantities are smoothly damped to the constant values near to the inner boundary. We only solve the upper half domain of the gas flow, imposing the reflective boundary condition on the equatorial plane at $\theta = \pi/2$.

For the initial condition, we start with an empty space around the black hole, but for the numerical reason, we put the thin isothermal ($T_{\rm iso} = 10^{11}$K) corona in the domain, which is in hydrostatic equilibrium.

In our simulation code, we use the Godunov method for hydrodynamics solver. During the simulation run, we continuously inject mass from the equatorial edge ($r = r_{\rm out}$, $\theta \in [0.45\pi, 0.5\pi]$) at a constant rate of $\dot{M}_{\rm inj}$. We assume that the injected mass has an angular momentum with its vector orientation being perpendicular to the equatorial plane and its absolute value being the same as that of the Keplerian rotation at $r = r_{\rm rot}$. Throughout the present study we fix $r_{\rm rot} = 100r_{\rm S}$. After the viscous timescale, an accretion disk is formed around the central black hole and the disk size is determined by $r = r_{\rm rot}$. We can control the mass accretion rate ($\dot{M}_{\rm acc}$) onto the central black hole by changing the mass injection rate $\dot{M}_{\rm inj}$. Hereafter, we use the normalized mass injection rate as $\dot{m}_{\rm inj} \equiv \dot{M}_{\rm inj}/\dot{M}_{\rm Edd}$. Super-Eddington accretion flow appears when $\dot{m}_{\rm inj} \gtrsim 10^2$. Likewise the mass accretion rates are normalized as $\dot{m}_{\rm acc} \equiv \dot{M}_{\rm acc}/\dot{M}_{\rm Edd}$

In this paper, we simulated three models for a variety of the mass injection rate (see Table 2.1). In Table 2.1, the symbols $\dot{m}_{\rm inj}$, $\dot{m}_{\rm acc}$, $\dot{m}_{\rm outflow}$, $\ell_{\rm iso}$, $\ell_{\rm tot}$, $\ell^{\rm iso}_{\rm kin}$ and $\ell_{\rm kin}$ are the value of $\dot{M}_{\rm inj}$, $\dot{M}_{\rm acc}$, $\dot{M}_{\rm outflow}$, $L_{\rm iso}$, $L_{\rm tot}$, $L^{\rm iso}_{\rm kin}$ and $L_{\rm kin}$ with the Eddington unit ($\dot{M}_{\rm Edd}$ for mass flow rates or $L_{\rm Edd}$ for energy flow rates) , respectively. Here the accretion rate $\dot{M}_{\rm acc}$ and the outflow rate $\dot{M}_{\rm outflow}$ are the integral of the inward mass flux crossing the inner boundary $r = 2r_{\rm S}$ and the integral of the outward mass flux crossing the outer boundary $r = r_{\rm out}$, respectively, and are numerically calculated by

$$\dot{M}_{\rm acc} = -\int_{r=2r_{\rm S}} \min(\rho v_r, 0)\, dS, \tag{2.9}$$

$$\dot{M}_{\rm outflow} = \int_{r=r_{\rm out}, v>v_{\rm esc}} \rho v_r\, dS \tag{2.10}$$

where dS is the surface element of the domain of integral and $v_{\rm esc}$ is the escape velocity at $r = r_{\rm out}$. Note that our definition of the outflow rates is different from that in Yuan & Narayan (2014), in which the outflow rate is calculated by integrating the entire outgoing gas (with $v_r > 0$). Also note that our estimate of outflow rates seems to be underestimated because the gas is pushed by radiation force so that the outflow rate should gradually increase as the gas travels farther from the black hole (Hashizume et al. 2015) Here $L_{\rm iso}$ means the isotropic

luminosity viewed from the direction with the inclination angle of $i \sim 3^\circ$ and $L_{\rm tot}$ means the total luminosity integrated over the whole solid angle;

$$L_{\rm iso} = 4\pi r_{\rm out}^2 F_r\big|_{r=r_{\rm out},\theta\sim 3^\circ}\,, L_{\rm tot} = \int_{r=r_{\rm out}} F_r\, dS \tag{2.11}$$

and $L_{\rm kin}^{\rm iso}$ and $L_{\rm kin}$ are calculated by

$$L_{\rm kin}^{\rm iso} = 2\pi r_{\rm out}^2 \rho\, \left[\max(v_r, 0)\right]^3\Big|_{(r,\theta)=(r_{\rm out},3^\circ)}\,, \tag{2.12}$$

$$L_{\rm kin} = \int_{r=r_{\rm out}, v>v_{\rm esc}} \rho v_r^3/2\, dS. \tag{2.13}$$

2.3 Results

In all the calculated models, we could finally achieve the quasi-steady states (Ohsuga et al. 2005). Hereafter, we only use the simulation data in the quasi-steady state. The elapsed times spent to reach the quasi-steady state are 40s (model 1), 170s(model 2) and 90s (model 3), respectively.

Table 2.1 Calculated three models. Here, $\dot{m}_{\rm inj}$ is denoted by mass injection rate. As for the definition of other quantities, see text. Such as mass accretion rate, mass outflow rate, isotropic luminosity, and etc, see equations (2.9)-(2.13)

model	$\dot{m}_{\rm inj}$	$r_{\rm out}[r_{\rm S}]$	$\dot{m}_{\rm acc}$	$\dot{m}_{\rm outflow}$	$\ell_{\rm iso}\ (\theta = 3^\circ)$	$\ell_{\rm tot}$	$\ell_{\rm kin}^{\rm iso}$	$\ell_{\rm kin}$
Eqn.#			(2.9)	(2.10)	(2.11)	(2.11)	(2.12)	(2.13)
1	10^2	500	70	2	2	1.5	10^{-4}	10^{-2}
2	10^3	5000	2×10^2	7×10^2	13	3	14	0.7
3	10^4	5000	4×10^2	1.7×10^3	50	3	70	0.9

2.3.1 Simulation overview

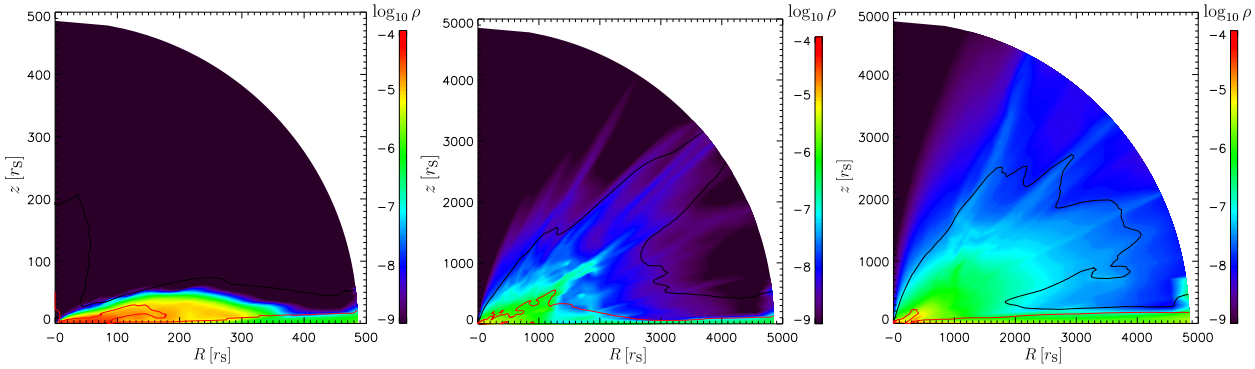

Fig. 2.1 Time-averaged density contour maps averaged on the logarithmic scale for mass injection rates of $\dot{m}_{\rm inj} = 10^2$ (left), 10^3 (center), and 10^4 (right) , respectively. Here, the horizontal (R) axis and the vertical (z) axis denote the cylindrical coordinates, respectively. Note different length scales between the left panel, and the middle and right panels. The black line in each panel indicates the location, where gas velocity is equal to the escape velocity, and the red line indicates the location, where the radial component of the velocity vanishes (that is, the gas in the region enclosed by the red line is falling onto the black hole).

We first overview the density structure of the super-Eddington flow in figure 2.1 for $\dot{m}_{\rm inj} = 10^2$, 10^3, and 10^4 from the left panel to the right, respectively. There is a fat and dense disk at $2r_{\rm S} \leq r \leq 100r_{\rm S}$ around the black hole for the right two models. The disk is optically and geometrically thick and is supported mainly by radiation pressure force. By comparing three panels we find a clear tendency that the higher the mass injection rate is, the narrower becomes the jet funnel. This is because the high-velocity jet is confined, being pressed by the pressure force by the surrounding fat disk.

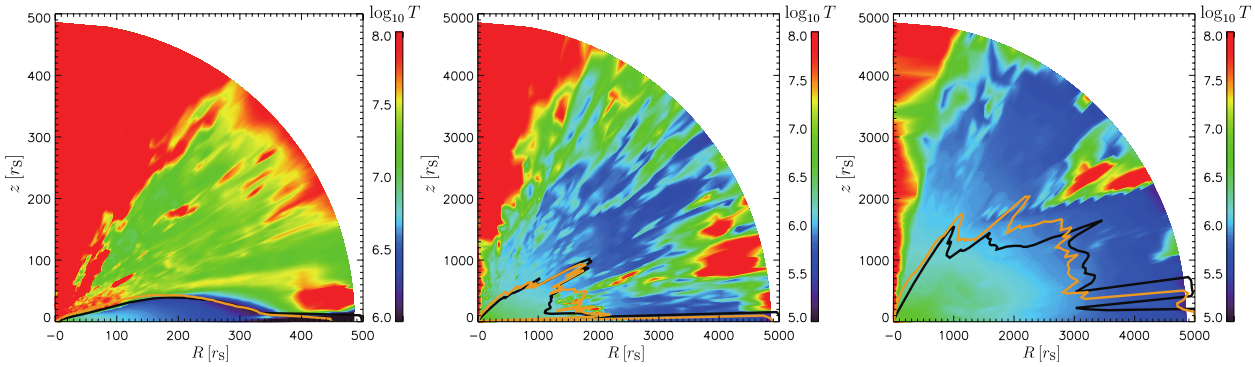

Fig. 2.2 Same as figure 2.1 but for the contour map of the gas temperature. The black line in each panel indicates the location of a photosphere on which $\tau_{\rm eff} = 1$ holds when integrated from the outer boundary, and the red line is for the Compton sphere $y_{\rm Comp} = 1$ calculated from the outer boundary as equations 2.16 and 2.17.

In figure 2.1 we see the blow up of a collimated jet with a very high speed ($\sim 0.7c$ for $\dot{m}_{\rm inj} = 10^3$) in the polar direction. We also see an uncollimated outflow blowing out within the a large opening angle ($\sim 80°$). This broad outflow is significantly Compton-cooled by copious soft photons emanating from the underlying gas inflow so that the gas temperature should be

close to radiation temperature (Kawashima et al. 2009). There is characteristic inflow structure at the angle of about $\sim 45°$ toward the center (see the region surrounded by the inner one of the two lines in figure 2.1). This is convective inflowing gas produced by the convective motion of gas.

Figure 2.2 shows the locations of the photosphere and Compton sphere plotted on the temperature contours in quasi-steady state. We can see that the temperatures on the Compton sphere and photosphere become low ($\sim 10^6$K) in the relatively high accretion rate case ($\dot{m}_{\rm acc} \gtrsim 10^2$). However, we can also see several high temperature parts (1 - 10 keV) in the outer region. These hot parts appear within intermittently blowing outflow.

Figure 2.3 shows the radial dependance of the mass inflow rates $\dot{M}_{\rm in}(r)$, the mass outflow rates $\dot{M}_{\rm out}(r)$, and the net flow rates $\dot{M}_{\rm net}(r)$ of each model;

$$\begin{aligned} \dot{M}_{\rm in}(r) &\equiv \int \rho \min(v_r, 0) r^2 {\rm d}\Omega, \quad \dot{M}_{\rm out}(r) \equiv \int \rho \max(v_r, 0) r^2 {\rm d}\Omega, \\ \dot{M}_{\rm net}(r) &\equiv \dot{M}_{\rm out}(r) + \dot{M}_{\rm in}(r). \end{aligned} \tag{2.14}$$

Although the net flow rate for models 2 and 3 is roughly constant at the regions of $r \lesssim 1000 r_{\rm S}$ and $r \gtrsim 3000 r_{\rm S}$, it is found that the rate varies with the radius at $r \sim 1000 - 3000 r_{\rm S}$. We also find the similar tendency in the model 1, in which the net flow rate is almost kept constant at $r \lesssim 100 r_{\rm S}$ and $r \gtrsim 300 r_{\rm S}$ and decreases with the radius at the region of $r \sim 100 - 300 r_{\rm S}$. This implies that the resulting inflow-outflow structure is not in actual steady state. To estimate the difference from the actual steady state, we continue the long term simulation for model 2 (about 5 times longer than model 2), in which we restart simulation from the end time of model 2 by resetting $\dot{m}_{\rm inj}$ to be 700. The dashed line in the middle panel of figure 2.3 shows the result of this long term simulation. We achieved a nearly steady state (the net flow rate is constant within 40% (see the black dashed line in this figure)). In this time, the accretion rate onto black hole and outflow rate from the outer boundary are almost same as model 2 and our main result for ULSs and ULXs (we will see this in §2.3.2) is not altered. Therefore we can rely on the results of model 1,2,3 although they have not reached their actual steady state yet. We must note that the outflow rates may be slightly overestimated due to the energy released by the accretion shock at $r = r_{\rm rot}$(but this energy is not so large when comparing the energy released by the disk accretion).

2.3.2 Observed luminosity and temperature

Next, we see the observed luminosity and temperature. Figure 2.4 shows the θ-dependance of observed temperature $T_{\rm obs}$ and isotropic luminosity $\ell_{\rm iso}$, where the observed temperature $T_{\rm obs}$ is evaluated between the photosphere and the Compton sphere (see figure 2.2). The photosphere and the Compton sphere are the place where the effective optical depth is $\tau_{\rm eff} = 1$ and Compton y parameter is $y_{\rm Comp} = 1$ calculated from the outer boundary of the simulation box, $r = r_{\rm out}$,

where $\tau_{\rm eff}$ and $y_{\rm Comp}$ are numerically evaluated by

$$\tau_{\rm es}(r) \equiv \int_r^{r_{\rm out}} \rho\sigma_{\rm T}/m_{\rm p}\, dr, \tag{2.15}$$

$$\tau_{\rm eff}(r) \equiv \int_r^{r_{\rm out}} \sqrt{\kappa(\rho\sigma_{\rm T}/m_{\rm p}+\kappa)}\, dr, \tag{2.16}$$

$$y_{\rm Comp}(r) \equiv \tau_{\rm es}\int_r^{r_{\rm out}} \frac{4kT_{\rm gas}}{m_e c^2}\rho\sigma_{\rm T}/m_{\rm p}\, dr, \tag{2.17}$$

respectively.

From the top panel of figure 2.4, we can understand that the observed temperature viewed from the angle $\theta < 20°$ is greater than several keV, typical temperature of ULX derived from the X-ray spectrum. At the angle greater than 35°, on the other hand, the observed temperature is less than or equal to 0.1 keV, the typical temperature of ULS. Despite such low temperatures, the observed luminosity is greater than Eddington luminosity in good agreement with the observations of ULS and ULX. Importantly, the luminosity viewed by nearly face-on observers is greater than that viewed by edge-on observers. This is consistent with the fact that the category of ULXs is typically more luminous than that of ULSs.

2.4 Discussion

2.4.1 Brief summary

In the present study we investigated the observable properties of supercritical accretion flow for a variety of accretion rates ($\dot{m}_{\rm inj}$) and viewing angles (θ), taking into account inverse Compton scattering effects. We pay particular attention to the distinct observational appearances of nearly face-on sources and of nearly edge-on sources. This is a marked difference from the cases of sub-Eddingtion source (either of standard-type disks or RIAF), in which the overall appearance is similar, not critically depending on the viewing angle. In short, nearly face-on observers will see supercritical accretors as luminous objects with large kinetic luminosities (comparable to the radiation luminosity), high ($\sim$ 1 keV) blackbody temperatures, and compact emitting regions with area on the order of $\sim r_{\rm S}^2$. The nearly edge-on observer will see them as, luminous but low-temperature ($\sim$ 0.1 keV) objects with large emitting area (much greater than $r_{\rm S}^2$) and with less kinetic luminosities. Such differences are remarkable above $\dot{m}_{\rm acc} \sim 10^2$ and are the results of high optical depth of accretion flow and significant outflow. We also confirm the clear tendency that the opening angle of high-velocity jets decreases with the increase of the mass accretion rate. In the following subsections we will discuss more about such unique features of super-Eddington flow.

2.4.2 Super-Eddington model for Ultra-Luminous Supersoft sources

In this subsection we discuss if our simulations support the hypothesis that the ultra-luminous supersoft sources (ULSs) may be a subgroup of the super-Eddington sources.

Some authors (Gu et al. 2016; Urquhart & Soria 2016) proposed a model of ULSs which unifies ULSs and normal ultraluminous X-ray sources, where the different observational characteristics

are probably related to the inclination angle and the mass accretion rate. They concluded that there are two necessary conditions for ULSs, i.e., high mass accretion rates $\dot{m}_{\rm acc} \gtrsim 30$ and not small inclination angles $\theta \gtrsim 25°$. For the other cases with super-Eddington accretion, the sources are likely to appear as normal ULXs.

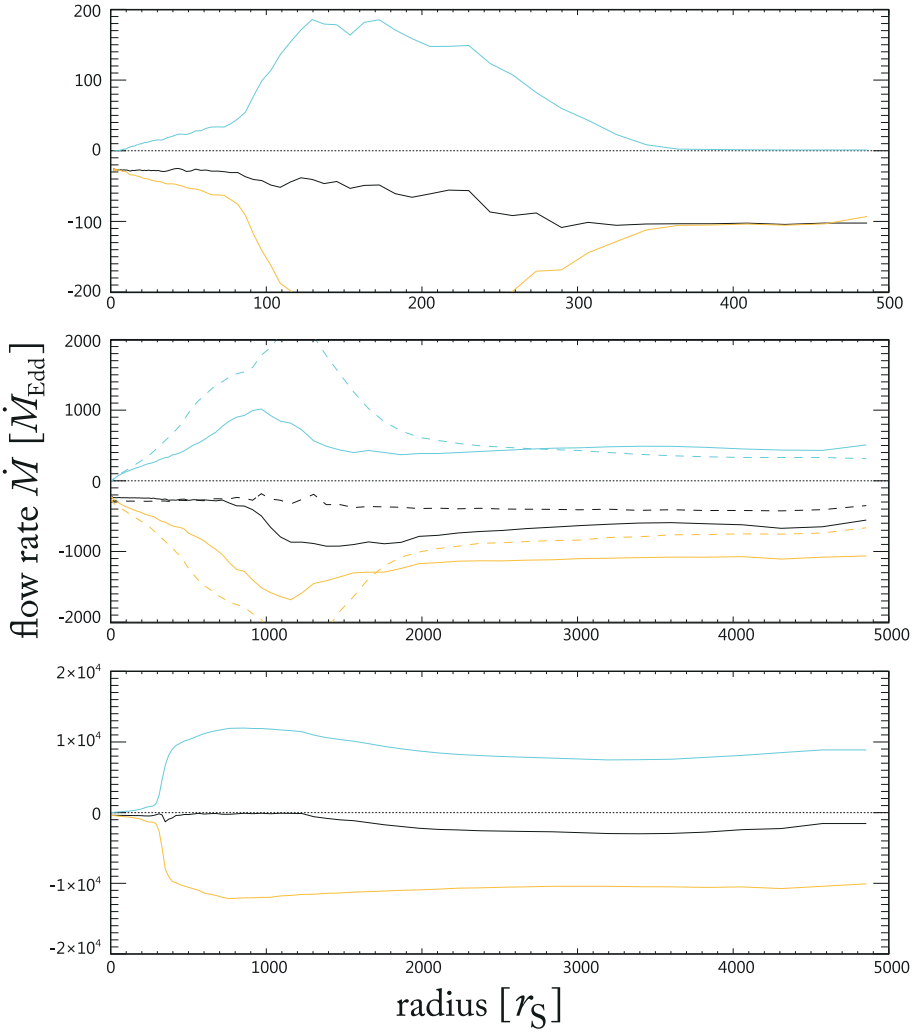

Fig. 2.3 radial dependance of the mass inflow rate (yellow solid line), mass outflow rate (blue solid line) and the net flow rate (black line) of models 1 to 3 from the top to the bottom, respectively. The dashed line in the middle panel shows the result of the long term simulation for model 2.

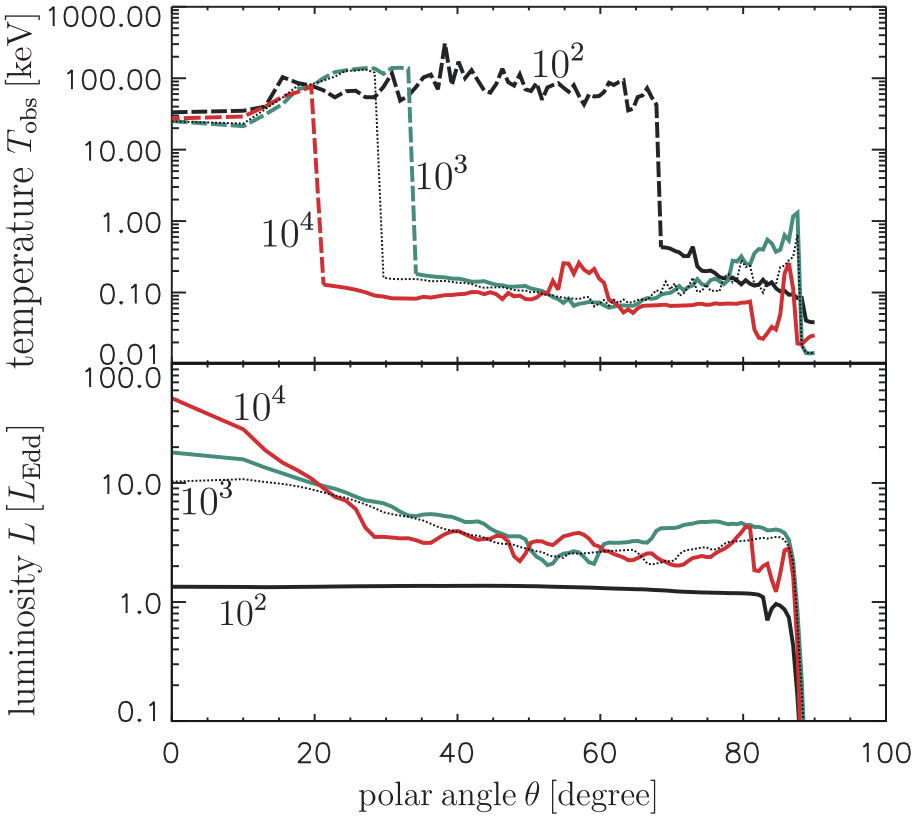

Fig. 2.4 Viewing angle (θ) dependence of observed temperature $T_{\rm obs}$ (top panel) and isotropic luminosity L defined by equation (2.18) (bottom panel) for various mass injection rates, $\dot{m}_{\rm inj} = 10^2$, 10^3 and 10^4. The horizontal axis is the polar angle θ [degree] and the vertical axes are temperature [keV] (top panel) and normalized isotropic luminosity [$L_{\rm Edd}$] (bottom panel), respectively. The dashed lines on the top panel indicate the temperature on the inner boundary in the case that the optical thickness is less than unity. The dotted line of each figure shows the result of the long term simulation for model 2.

We thus examine our simulation data to see if they support the super-Eddington hypothesis. We found that the temperature and luminosity are in the reasonable ranges for explaining the ULSs, if we adopt $\dot{m}_{\rm acc} \sim 400$ and $\theta \gtrsim 25°$. Figure 2.4 shows the θ-dependence of the isotropic luminosity at the outer boundary, calculated by

$$L(\theta) \equiv 4\pi r_{\rm out}^2 F_r(r = r_{\rm out}, \theta) \tag{2.18}$$

and the observed temperature $T_{\rm obs}$ which can be considered to be the temperature on the outer sphere between the Compton sphere and the photosphere, respectively. When the photosphere viewed from an angle vanishes, the observed temperature is set as the temperature on the inner boundary (see the dashed line on figure 2.4). Since the luminosity of ULSs are about $10^{39}{\rm erg\,s^{-1}} \sim 1L_{\rm Edd}$ for $10M_\odot$, the reasonable viewing angles are whole angles for model 1, $\theta \gtrsim 45°$ for model 2 and $\theta \gtrsim 25°$ for model 3, respectively. Since the blackbody temperature of the ULSs are around 0.1 keV, the reasonable range of the viewing angle is $\theta \gtrsim 65°$ for model 1, $\theta \gtrsim 35°$ for model 2 and $\theta \gtrsim 20°$ for model 3, respectively. We thus conclude that the basic observed properties of the ULSs can be expained for the viewing angle of $\theta \gtrsim 30°$

for $10^2 \lesssim \dot{m}_{\rm acc} \lesssim 10^3$. Moreover, our result shows that, the more the accretion rate is, the more likely a ultraluminous source is to be observed as a ULS. This fact is consistent with the classification of ULSs and ULXs in Urquhart & Soria (2016).

We can roughly understand why the observed temperature of supercritical accretor is ~ 0.1 keV for an edge-on observer in the following way. From the relationship $L \sim 4\pi r^2 \sigma T^4$ we find

$$T(r) \sim 1(M/10M_\odot)^{-1/4}(r/3R_{\rm s})^{-1/2}\,{\rm keV}, \tag{2.19}$$

for $L \sim L_{\rm Edd}$ due to the photon trapping effect (Begelman & Meier 1982). When we see the supercritical flow from large angles, we see the outer surface of the inflated region. Further, the size of the inflated region is approximately the trapping radius

$$R_{\rm tra} \sim \dot{m} R_{\rm s} \tag{2.20}$$

(see Kato et al. 2008, Chapter 10). We thus find

$$T(R_{\rm trap}) \sim 0.1(\dot{m}/300)^{-1/2}\,{\rm keV} \tag{2.21}$$

From this relationship we also understand the tendency that the higher $\dot{m}$ is, the lower becomes the observed temperature, in good agreement with figure 2.4.

We have two remarks here. First, since the outflow blowing out is optically thick even at the outer boundary, we might have overestimated the luminosity and the temperature. Second, when the mass injection rate is high (in the model 2 for example), the outflow going along the disk is accelerated and heated by radiation and thus the temperature is relatively high ($\sim 10^7$K or higher). This may be because the disk has a steep edge facing to the equatorial direction due to the low angular momentum of injected gases and the photons from the edge can effectively accelerate the gas toward the equatorial direction. This is an artifact resulting from our assumed (relatively small) specific angular momentum; that is, larger specific angular momentum is needed in the injected gas. We, hence, need more extensive study with a larger computation box to establish the super-Eddington scenario.

2.4.3 Application to the Extreme Ultra-Luminous X-ray sources

The Extreme Ultra-Luminous X-ray sources (EULXs), which have higher luminosities ($L_{\rm X} \gtrsim 10^{41}{\rm erg\,s^{-1}} \sim 10^3 L_{\rm Edd}$ for a 10 $M_\odot$ black hole) than normal ULXs, were discovered recently. Since such huge luminosity is not easy to explain by the super-Eddington accretion scenario, it is considered as the most promising candidate for the intermediate-mass black hole. Our results demonstrate, however, that even such huge isotropic luminosities as those of EULXs can also be accounted for by supercritical accretion (see model 3, in Table 1; the luminosity viewed by face-on observers can reach nearly 100 times greater than Eddington luminosity.). We thus support that EULXs may also be super-Eddington accretors.

Note, however, that the luminosity of the EULXs can be reproduced only when the mass injection onto the accretion disk is huge; $\dot{m}_{\rm inj} \gtrsim 10^4$ and the central black holes is slightly heavier,

$M_{\rm BH} \gtrsim 20 M_\odot$. Note also that special relativistic effect is not considered and thus the relativistic beaming is neglected in our simulation. In other words, the isotropic luminosities could be underestimated when $\dot{m}_{\rm acc}$ is high. This needs to be confirmed in future GR simulations.

2.4.4 Very strong outflow

One of the most remarkable observational features of the super-Eddington sources should be emission from their environmental gas (or nebula) which shines by receiving a significant impact by the strong outflow. This will explain the so-called ULX bubbles. In fact, our simulation demonstrates the emergence of very strong outflow at high $\dot{m}_{\rm acc} \gtrsim 10^2$. Furthermore, the outflow rate overcomes the accretion rate at $\dot{m}_{\rm acc} \gtrsim 10^2 - 10^3$. Such strong outflow inevitably causes some significant impacts on its circumstances. It should be noted that the outflow rate cannot exceed the mass injection rate (from the calculation boundary) but CAN exceed the accretion rate (onto the black hole) (see also Hashizume et al. 2015). Note also that the sum of the outflow and accretion rates is by about one order of magnitude less than the mass injection rate, meaning that the mass is continuously accumulated within the simulation domain with the time. In future work we plan to perform longer simulations with a larger $r_{\rm rot}$ to see an actual steady-state flow structure.

Outflow from radiation-pressure dominated disk is likely to become clumpy above the photosphere (Takeuchi et al. 2013). Although we cannot resolve the clumpy structure in our simulation because of lack of resolution (note that the size of each clump is about one optical depth; see Takeuchi et al. 2014), we can easily check whether the outflow from super-Eddington accretion flow calculated in our simulation could be clumpy or not by using the condition found by Takeuchi et al. (2014). Basically, the condition is so simple; clumpy outflow appears if the radiation force overcomes the gravitational force.

2.4.5 How to achieve high injection rates?

In our simulation, we consider the mass injection rate $\dot{M}_{\rm inj}$ as a parameter. Here, we discuss how a large amount of gas can be injected into the accretion disk from a companion (in the case of binary system).

A population synthesis study for binary systems by Wiktorowicz et al. (2015) shows that a $10 M_\odot$ black hole is fed by a massive ($\sim 10 M_\odot$) Hertzsprung gap donor with Roche lobe overflow (RLOF) rate of $10^{-3} M_\odot {\rm yr}^{-1}$ ($\approx 2600 \dot{M}_{\rm Edd}$) and the maximum RLOF rate reaches $10^{-2} M_\odot {\rm yr}^{-1}$ ($\approx 3 \times 10^4 \dot{M}_{\rm Edd}$).

There should be some circumstances, in which feeding sufficient gas at a super-Eddington rate (up to $\sim 10^4 \dot{M}_{\rm Edd}$) to the vicinity of the black hole is feasible.

2.4.6 Difference from other numerical simulations

Our simulations do not take into account the effects of general relativity. The effects of general relativity become very important when considering the physics at the vicinity of the event horizon and the spin of black holes. The general relativistic radiation hydrodynamical simulations performed by Sądowski et al. (2015) show that the outgoing mass flow rate is by an

order of magnitude greater than the accretion rate for $\dot{M}_{\rm acc} \approx 100\dot{M}_{\rm Edd}$ when the black hole spin is high, $a = 0.9$, while they are on the same order, if $a = 0$. Thus the general relativistic simulation tends to show more significant outflow than Newtonian simulation, probably because more gravitational potential energy is available in general relativity than in Newtonian or post-Newtonian gravity, especially in the case of highly prograde rotating black hole. In table 2.1, the outflow rate at $\dot{M}_{\rm acc} \approx 200\dot{M}_{\rm Edd}$ is an order of magnitude lower than the result of the relativistic simulation. The higher the black hole spin is, the closer ISCO is to the event horizon, so the more the released energy of the spinning black hole is (at maximum about 10 times higher than the non-spinning case). Moreover, another mechanism, so-called Blandford-Znajek process, works to increase the released energy for magnetized spinning black holes. For this reason, we must also perform the general relativistic radiation magnetohydrodynamical simulations in order to do more precise and realistic studies.

CHAPTER 3

VARIABILITY OF COMPTONIZED X-RAY SPECTRA OF SUPER-EDDINGTON ACCRETOR: APPROACH BY BOLTZMANN RADIATION TRANSPORT

3.1 Introduction to Chapter 3

Precise modeling of Compton scattering process should be a critical issue, but it is not an easy task especially for relativistic plasmas under strong gravity. Several semi-analytic or simple numerical approaches are known for calculating radiation transfer with Compton scattering in accretion flow (see Rybicki & Lightman 1979, and references therein). However, more accurate and more realistic transfer calculations are required recently, since high resolution spectral data are now available thanks to the rapid progress in observational instrumentations (e.g., NuStar etc).

The Monte-Carlo method is the most widely used, powerful tool for calculating radiation transfer with Compton scattering (e.g., Pozdnyakov et al. 1977; Dolence et al. 2009; Kawashima et al. 2012; Mościbrodzka et al. 2014). The great advantage of this method is that it can relatively easily calculate the scattering process, which is very complex in high temperature gas layers and/or in moving scattering medium with relativistic speed. In this method, we deal with statistics of the trajectory of photon packets in the phase space; that is, photons experience Compton scattering with electrons, obeying the *a priori* prescribed statistics. The disadvantage of the Monte-Carlo approach is, however, that the precision is limited by photon statistics. This limitation appears to be most severe, when we handle the photons with much higher energy than that of the seed photons, since the number of the former (up-scattered) photons could be very small, leading to rather poor statistics. Other disadvantages are difficulty in time-dependent calculation, lack of stimulated Compton scattering, and spatial resolution of physical quantities.

Another approach is solving the Boltzmann radiation transport equation to obtain the distribution function of photons in 6-dimensional space (3-dimensional (3-D) real space and 3-D momentum space; see, e.g., Sumiyoshi & Yamada 2012; Nagakura et al. 2014; Takahashi & Umemura 2017). The merit of this approach is its capability of simulating time evolution of the medium, since we know the distribution function at all the spatial points and can thus calculate feedback effects on the interacting medium. Another advantage is that this method can naturally be connected to the radiation hydrodynamics (RHD) simulation codes, which will make it possible to perform frequency-dependent RHD simulations in future. The weak point of this method is a difficulty in calculating the Compton scattering process, since it is highly complicated when bulk and/or thermal velocities are relativistic or when we consider high energy regime. Another concern is the treatment of multiple scatterings. The scattering timescale is generally much shorter than that of the fluid or light crossing time. Usually, the time interval Δt is determined by the light crossing time and so the gas-radiation interaction term should be calculated by the implicit method. Then, the number of experiencing scattering in one time-step should be much smaller than that in the realistic case, however, since the scattering kernel describes only a single scattering. That is, the multiple scattering cannot be precisely calculated by the Boltzmann-solver calculations, especially when the time interval Δt is taken to be much longer than the scattering timescale.

To summarize, the Monte-Carlo method is easier to handle with but has a difficulty in solving time-dependent problems, while the Boltzmann method is advantageous in solving the time-dependent problems but is not easy to properly calculate multiple scattering processes. In the present study, therefore, we propose a new methodology how to combine these two methods and apply our method to solve the problem of low-temperature, optically thick Comptonization as is realized in super-Eddington flow. On the basis of the probability function of a single scattering calculated by the Monte-Carlo method, we can reconstruct the probability function of the multiple scattering. The time evolution is then solved by the Boltzmann equation and the source term is calculated by the probability function of multi-scatterings. This enables us to calculate time-dependent radiation fields with multiple thermal/bulk Compton scatterings. The present study will mark an important milestone towards the construction of a frequency-dependent GRRMHD simulation code of accretion flow in general context. We first explain the basic methodology in §3.2 and then show the results of typical cases in §3.3. The final section is devoted to discussion.

3.2 Method

We developed a new code of the grid-based Boltzmann solver of the radiation transfer, incorporating the Compton scattering process, in the curved space-time described by the Schwarzschild metric and calculate the observed spectra of super-Eddington accretion flow and outflow by the post-processing. In the present paper, we set G=c=1 so that the unit of the length scale is $1M = 15(M/10M_\odot)$ km and that of the timescale is $1M = 5 \times 10^{-5}(M/10M_\odot)$ s.

3.2.1 GRRMHD Data for Background

We use the GRRMHD data, $(\rho, T, \boldsymbol{v})$, for calculating the radiation field in our simulation where ρ is the density, T is the temperature, $\boldsymbol{v}$ is the velocity of the fluid. These data are obtained by the 2-D axisymmetric simulations by Takahashi et al. (2018) who solve the GRRMHD equations in the polar coordinates on the basis of the Kerr-Schild metric around a non-spinning black hole. Here, we summarize the properties of the used GRRMHD simulation data:

- The simulation domain $(r[M], \theta[\mathrm{rad}]) \in [1.96, 245] \times [0, \pi]$ is divided into 264×264 cells. They put a 10 $M_\odot$ black hole at the origin ($r = 0$).
- They started the simulation from an equilibrium torus composed of pure hydrogen plasmas and threaded with single poloidal magnetic fields. The inner edge of the initial torus is at $r = 20\ M$ and the pressure maximum is at $r = 33\ M$,
- They could reproduce the super-Eddington accretion flow and radiatively driven outflows. The mass accretion rate onto the central black hole is about $300 L_{\mathrm{Edd}}$ in the quasi-steady state, which is achieved after the elapsed time of $3000M$.
- In the quasi-steady state, no unphysical flares (which are occasionally observed in the simulations based on the M1 scheme) nor artificial abrupt heating do not occur.

We employ the simulation data which are time averaged over the time span of $t = 3000 - 3300M$ (in the quasi-steady state). Figure 3.1 shows, from the left to the right, the contour maps of the density, temperature, and velocities overlaid with the velocity vectors, respectively. We see two-phased structure composed of dense, low-temperature torus region and tenuous, high-temperature outflow region.

Before performing the radiation transfer calculation, we transformed the values described in the Kerr-Schild metric into those in the Schwarzschild metric. We also reduced the numerical resolution of the data from 264×264 grid points to 32×64 grid points because of the limitation from the calculation resource. The electron temperature in our calculation is assumed to be equal to the proton temperature, for simplicity (this approximation will be discussed in §3.4.3).

3.2.2 Basic equation

The basic equation that we solve in the present paper is the conservative form of the Boltzmann equation in the Schwarzschild coordinates (t, r, θ, φ) derived by Shibata et al. (2014),

$$\begin{aligned}
&\left(1-\frac{2M}{r}\right)^{-1/2}\frac{\partial f}{\partial t}+\frac{1}{r^2}\frac{\partial}{\partial r}\left[f\cos\bar{\theta}\, r^2\left(1-\frac{2M}{r}\right)^{1/2}\right]\\
&+\frac{1}{r\sin\theta}\frac{\partial}{\partial\theta}\left(f\sin\theta\sin\bar{\theta}\cos\bar{\varphi}\right)\\
&+\frac{1}{r\sin\theta}\frac{\partial}{\partial\varphi}\left(f\sin\bar{\theta}\sin\bar{\varphi}\right)\\
&-\frac{1}{\nu^2}\frac{\partial}{\partial\nu}\left[f\nu^3\cos\bar{\theta}\,\frac{M}{r^2}\left(1-\frac{2M}{r}\right)^{-1/2}\right]\\
&-\frac{1}{\sin\bar{\theta}}\frac{\partial}{\partial\bar{\theta}}\left[f\sin^2\bar{\theta}\,\frac{r-3M}{r^2}\left(1-\frac{2M}{r}\right)^{-1/2}\right]\\
&-\frac{\partial}{\partial\bar{\varphi}}\left(f\frac{\cot\theta}{r}\sin\bar{\theta}\sin\bar{\varphi}\right)=S_{\rm rad}
\end{aligned}\tag{3.1}$$

where f, M and $S_{\rm rad}$ are the distribution function of photons, the mass of a central black hole and the source term via gas-radiation interactions, respectively. The set $(\nu, \bar{\theta}, \bar{\varphi})$ represents the coordinates in the momentum space of photons, in which ν is the frequency of photons measured by an Eulerian observer, $\bar{\theta}$ is the angle between the direction of the photon propagation and the r-direction, and $\bar{\varphi}$ is the angle between the θ-direction and the projected photon momentum vector on the plane perpendicular to the r-direction. Note that we use the fluid data provided by 2-D axisymmetric simulation so that the derivative $\partial/\partial\varphi$ vanishes.

We solve the left-hand-side of the equation (3.1) (i.e., the advection term) by the second order upwind method with the min-mod limiter (although it is slightly modified as will be shown in appendix B.3.1). The right-hand-side which is the source term of gas-radiation interactions is solved with using the interaction tables (see appendix B.3.2).

3.2.3 Simulation setup

We perform the radiation transfer simulations within the 5-dimensional (5-D) simulation domain of $r[M] = 2.1$-250, $\theta = 0$-π, $h\nu$[keV] $= 0.01$-500, $\bar{\theta} = 0$-π, and $\bar{\varphi} = 0$-2π. The grid points are uniformly distributed in the θ-, $\bar{\theta}$-, and $\bar{\varphi}$-directions, and uniformly distributed in the logarithm in the ν- and r-directions, respectively. The number of grid points are $(N_r, N_\theta, N_\nu, N_{\bar{\theta}}, N_{\bar{\varphi}}) = (32, 64, 50, 9, 8)$. As the opacity sources, the Bremsstrahlung by a pure hydrogen plasma and the electron scattering (with Klein-Nishina cross-section) are included.

At the inner and outer boundaries, $r[M] = 2.1$ and 250, we employ the free (no-gradient) boundary conditions for the outgoing radiation and the incoming radiation is set to be zero. We use the reflective boundary condition at $\theta = 0$ and π as well as at $\bar{\theta} = 0$ and π. At the boundaries of the frequency grid we employ the dumping boundary condition (i.e., we assign small values there). We use the periodic boundary condition at $\bar{\varphi} = 0$ and 2π.

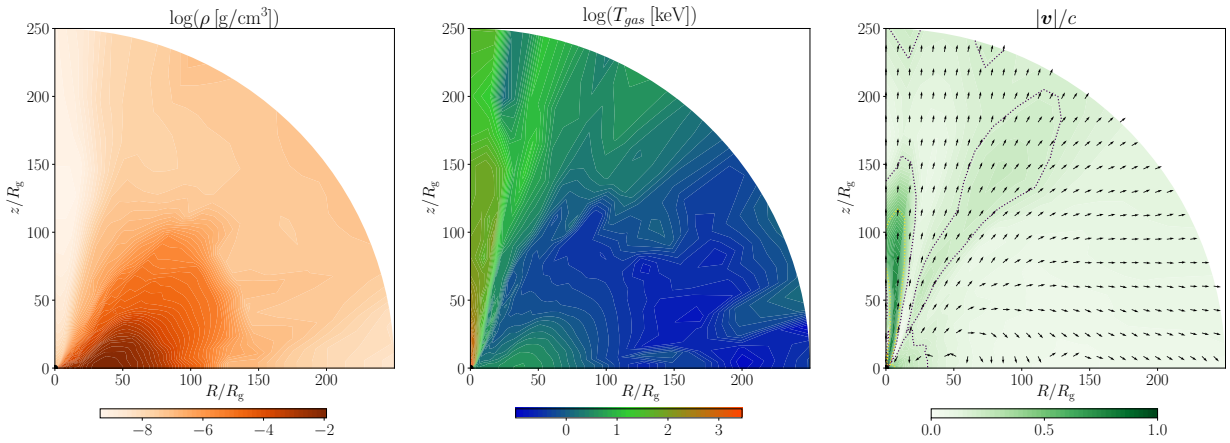

Fig. 3.1 The GRRMHD simulation data used in the present study. Color contours of the gas density, the gas temperature, and the gas velocity are displayed in the left, middle, and right panels, respectively. The right panel is overlaid with the velocity vectors. The black (yellow) dotted contour lines in the right panel indicate the loci of $|\boldsymbol{v}/c| = 0.2(0.5)$.

Initially we assume no radiation field in the whole simulation domain and calculate the time evolution of the radiation fields by solving the equation (3.1).

3.3 Results

3.3.1 Simulation Overview

We calculate the observed luminosity at frequency ν seen from the viewing angle of $\theta_{\rm view}$, $L_\nu(\theta_{\rm view}, t)$, and the bolometric luminosity, $L_{\rm bol}(t)$, by

$$L_\nu(\theta_{\rm view}, t) = 4\pi \int_{\{\theta,\bar{\theta},\bar{\varphi}\}\in\Lambda(\theta_{\rm view})} I_\nu(t, r = r_{\rm out}, \theta, \bar{\theta}, \bar{\varphi}) dS \tag{3.2}$$

where the set $\Lambda(\theta_{\rm view})$ contains all elements $(\theta, \bar{\theta}, \bar{\varphi})$ satisfying the condition where the direction determined by $(\theta, \bar{\theta}, \bar{\varphi})$ is parallel to the direction of observer $(\theta_{\rm view})$ and where it is outward-directing on the outer boundary of the simulation domain, and the area element dS is that on the screen of the distant observer, and

$$L_{\rm bol}(t) = \frac{1}{2} \iint L_\nu(\theta_{\rm view}, t) d\nu d(\cos\theta_{\rm view}), \tag{3.3}$$

at each time, respectively. Here, we assume that the photons go straight without being suffered from the gravitational redshift at the outside the computational box, since the distance from the black hole is sufficiently far that the GR effect is negligibly small. We plot how the bolometric luminosity grows, starting from the initial zero-luminosity state, in the left panel of figure 3.2. The bolometric luminosity reaches $\sim 10^{40}$erg s^{-1}($\sim 10\ L_{\rm Edd}$) in four light crossing times (where we define the light crossing time to be $t_{\rm cross} \equiv r_{\rm out}/c = 250\ M$). We see that the radiation field settles down in a quasi-steady state at $t > t_{\rm qss} \equiv 4t_{\rm cross}$ (see the left panel of figure 3.2).

The right panel of figure 3.2 shows the observed spectra in the quasi-steady state, $L_\nu(\theta_{\rm view}, t = t_{\rm qss})$ for various viewing angles. We see a clear trend that the larger the inclination angle is,

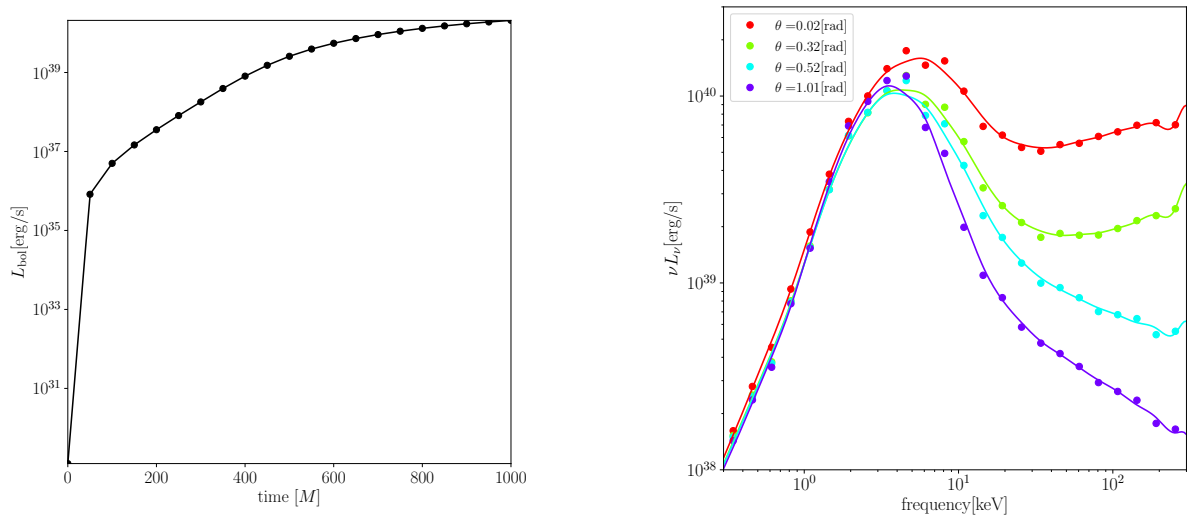

Fig. 3.2 *Left* panel: Time evolution of the total luminosity over time span of $0 - 1000M$. *Right* panel: Observed spectra (in the quasi-steady state) viewed from a distant observer located at angles of $\theta_{\rm view}$ [radian]$= 0.02$ ($\sim 0°$, red), 0.32 ($\sim 20°$, green), 0.52 ($\sim 30°$, blue), and 1.01 ($\sim 60°$, purple), respectively. The closed circles denote the calculated data points, whereas the curves represent the spline fits to the three-point average of the data points.

the lower becomes the hard X-ray component, and, hence, the softer becomes the spectrum. This can be easily understood, since the high energy photons (with energy > 10 keV) are mostly generated in the funnel region. Therefore, they can be observed only by a nearly face-on observer (with a viewing angle $\theta_{\rm view} \leq 30°$) and are not seen by a nearly edge-on observer, for whom they are effectively blocked by optically thick outflow. The lower energy photons (with energy < 10 keV), by contrast, originate from much wider region surrounding the funnel and disk, and, hence, always observable: they can directly propagate even to an edge-on observer.

We next examine the two-dimensional distributions of the radiation energy density in the simulation box. The upper left panel of figure 3.3 shows the color contours of the total radiation energy density (integrated over photon energy) overlaid with the total energy flux vectors, while the other three panels of figure 3.3 illustrate the color contours of the energy density of radiation with $\nu = 1$ (upper right), 10 (lower left), and 100 keV (lower right), respectively. Loci of the effective optical depth of $\tau_{\rm eff}$ =1 and 10 are indicated by the black solid and black dotted lines, respectively, while those of the Thomson optical depth of $\tau_{\rm es}$ =1 and 10 are indicated by the yellow solid and yellow dashed lines, respectively.

The strongest is the 10 keV emission from the optically thick disk region. (This is the reason why the total radiation energy density reaches its maximum value there). Further, we find in the lower two panels that the high energy photons with $\gtrsim 10$ keV emerge from hot regions within the jet funnel region. Here, by the funnel region we mean the region which is full with hot ($T > 10^8$ K), tenuous (with Thomson optical depth of $\tau_{\rm es} < 1$), and rapidly outflowing (with $v > 0.1\ c$) gas (Kitaki et al. 2017). Crudely, this funnel region has an opening angle of $30°$ (the region above the black dashed line in the upper-left panel) and is surrounded by the slower (with velocity $v < 0.1\ c$) and denser outflow region. Such high energy photons propagate

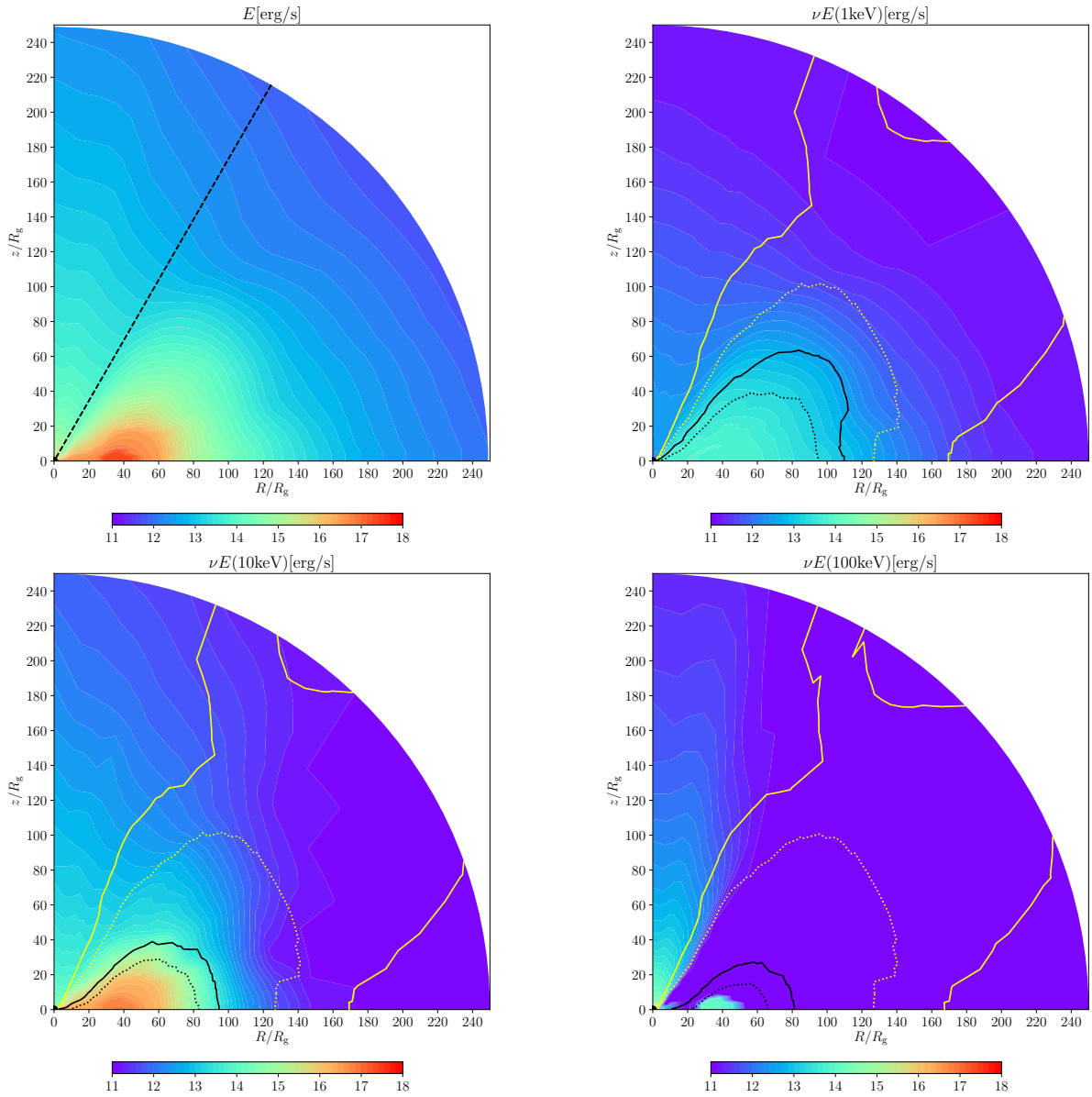

Fig. 3.3 Contour maps of the total radiation energy density (upper left) and the radiation density at different energy bins: 1 keV (upper right), 10 keV (bottom left), and 100 keV (bottom right), respectively. The lines in the last three panels indicate the loci of $\tau_{\rm eff} = 1$ and 10 (black solid and dotted lines), and $\tau_{\rm es} = 1$ and 10 (yellow solid and dotted lines), respectively. The dashed line in the upper left panel is the line with the polar angle of $\theta = 30°$, which indicates the approximate position of the funnel wall.

along the polar axis or are advected by the optically thick outflow, which is launched from the inner hot region and propagate toward the direction of the polar angle of $20^\circ - 40^\circ$. The 10 keV photons are produced mostly within the disk and some in the funnel, whereas the 1 keV photons originate in much wider space in and around the disk. The photons emitted from the disk can effectively lose their energy via Compton scattering, whereas those from the funnel can partly leak into the slower and denser outflow region.

3.3.2 Dependence of intensity map on viewing angles and photon energies

We next show in figure 3.4 how the super-Eddington accretion flow and outflow look like in X-rays to distant observers at different viewing angles (measured from the polar axis), $\theta_{\rm view}$. The upper panels show the images of the flow seen from the viewing angle of $\theta_{\rm view} \sim 0^\circ$ at photon energy of 1 keV, 10 keV, and 100 keV from the left to the right panels, respectively. In all the panels the polar cap region around $(x, y) = (0, 0)$ is brightest and the region around $\theta \sim 50^\circ$ is the second brightest, about one third of the former. Although the emission from the latter is not so strong, it has a much wider area than the former.

The three panels in the middle row show the same but seen from $\theta_{\rm view} \sim 20^\circ$. A large fraction of hard photons (with $\gtrsim 10$ keV) comes from the funnel region, whereas lower energy ones originates from more or less entire region. The brightest region at 1 keV is off-polar regions of $\theta = 20^\circ - 50^\circ$. The same trend can be seen in the bottom panels for the cases with $\theta_{\rm view} \sim 30^\circ$. Since gas is rotating around the black hole, radiation tends also to go around the polar axis after undergoing multi-scattering, especially in the optically thick region. This effect can be clearly seen in the middle and lower rows in figure 3.4. From all the panels in figure 4 we understand that the very high-energy emission (above a few tens of keV) is very sensitive to the viewing angle, while softer emission is not so sensitive to the viewing angle.

3.3.3 Spectral variability caused by a flare

It is well known that black hole objects commonly exhibit significant degree of variabilities on various timescales. Such variabilities were already known in the dawn of X-ray astronomy (e.g., Oda et al. 1971) but their origin remains to be an open issue until now (see, e.g., Done et al. 2007; Falanga et al. 2015, and reference therein). One of the most promising possibility is assembly of flare-like events (Galeev et al. 1979). Frequent occurrence of magnetic flares is very likely in hot accretion flow like RIAF and in accretion disk corona, since both seem to be composed of hot magnetized plasmas, like solar coronae. This has led to the idea of the lamp post model, in which a compact hard X-ray emitting source above a black hole illuminates a surrounding accretion disk (e.g., Martocchia & Matt 1996; Miniutti & Fabian 2004). It is thus curious to see how spectra change with time in response to a flaring event occurring in the innermost region.

Prompted by such consideration, we calculated the spectral variation of a super-Eddington accretor in response to a sudden heating of the innermost zone caused by a flaring event (i.e., magnetic reconnection). Using the simulation data at $t_0 = 1000\ M$, in which a quasi-steady

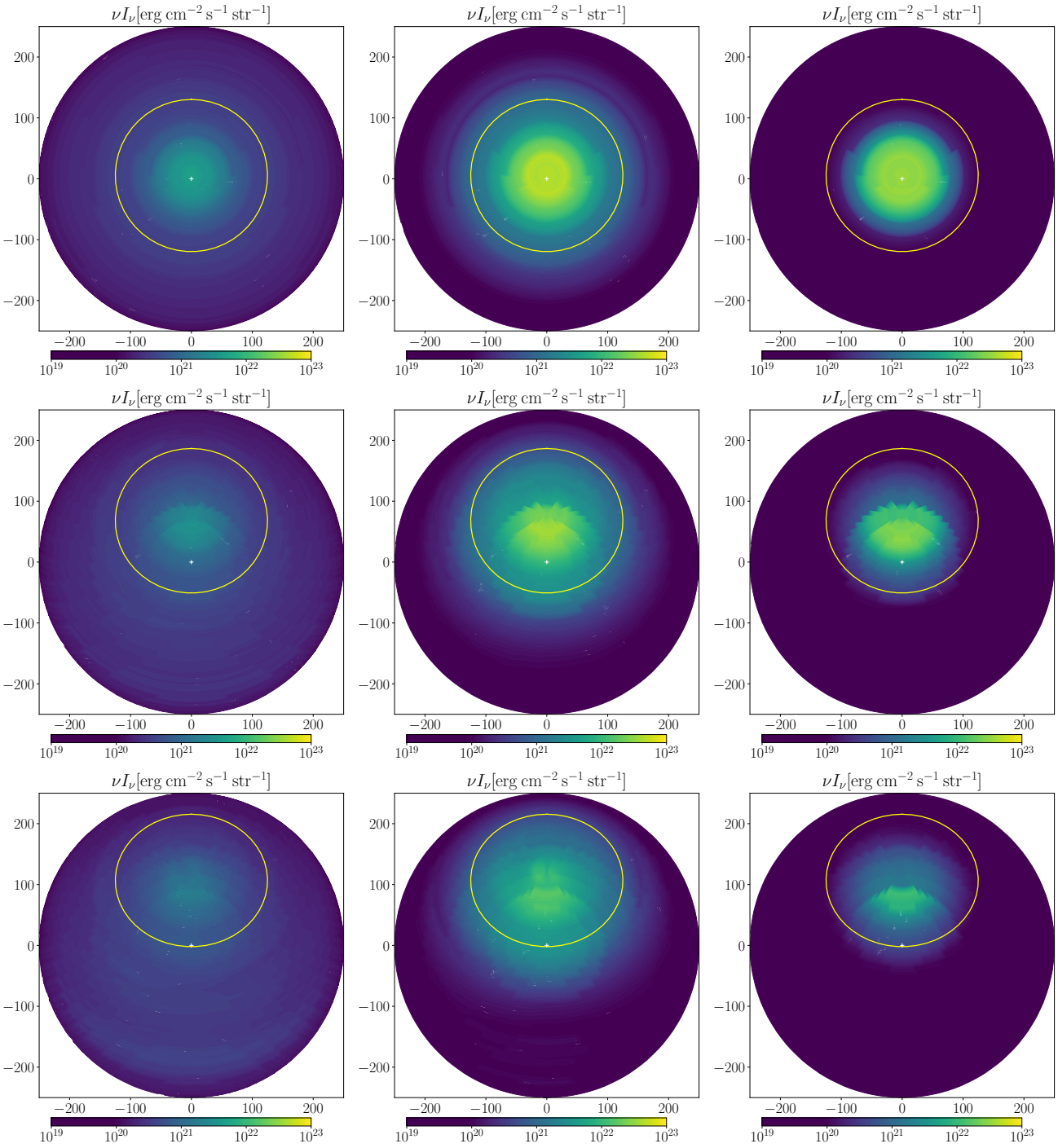

Fig. 3.4 Observed images by a distant observer located at viewing angles (measured from the polar axis) of 0° (upper row), 20° (middle row), and 30° (bottom row) for the photon energy of 1 keV (left column), 10 keV (middle column), and 100 keV (right column), respectively. The yellow line represents the intersection between the funnel wall (defined by the polar angle of $\theta = 30°$, see figure 3.1) and the outer boundary of the simulation box. The plus marker indicates the position of the origin, where the black hole is located.

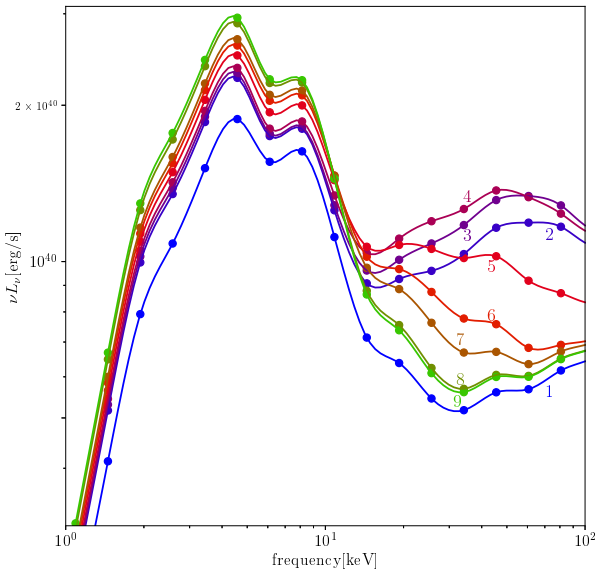

Fig. 3.5 Time evolution of the observed spectra in response to a flare that occurred at $t = t_0$ in the innermost zone viewed by a face-on observer (with $\theta_{\rm view} = 0°$). The color of the line changes from blue, red, to green, as time goes on. The number near each line indicates the order of the time evolution; that is, $t - t_0\ [M] = 50, 300, 350, 400, 450, 500, 550, 800$, and 1000 for the number, 1 to 9, respectively, Note that the time of $1000M$ corresponds to $\sim 0.05(M/10M_\odot)$ sec).

state is achieved, we suddenly raise the gas temperature $T_{\rm gas}$ in the innermost funnel region ($r < 20\ M$ and $\tau_{\rm es} < 10$ where $\tau_{\rm es}$ is the optical depth by electron scattering calculate from the polar axis) by a factor of 10 for a time interval of $200M$ (corresponding to the 10 light crossing time of the flare region), and then suddenly drop the gas temperatures to their original values. We calculate how the spectrum changes with time by the occurrence and termination of the flare and show the results in figure 3.5.

As is clearly shown in this figure, spectra are largely deformed during the flare, especially in the hard X-ray range above $\sim$ 20 keV. Notably, such variations are sensitive to the viewing angle; the smaller the view angle is, the larger becomes the variation amplitude. In the face-on case, the high energy photon ($\gtrsim$ 20 keV) counts begin to increase at $t = 1250\ M$ ($\sim t_0 + t_{\rm cross}$, between the number 1 and 2 in figure 3.5), reach their maximum value at $t \sim 1400\ M$ (between the number 4 and 5 in figure 3.5), and then decay to the steady-state values. The maximum amplitude of the variation is by a factor of $\sim$ 3 at photon energy of $\sim$ 60 keV.

Then, why is the variability amplitude larger in hard X-rays to a face-on observer? This is because hard X-ray emitting region is much more compact than the soft X-ray emitting region (see figure 3.3) and because the hard X-rays can only reach nearly face-on observers and are blocked to large viewing-angle ($\theta_{\rm view}$) observers (see the right panel of figure 3.2, see also figure 3.4).

Another noteworthy feature is the time delay in response among different energy bands: that is, 60-100 keV photons rise more quickly than 15-30 keV photons, but the decay is similar among different energy bins. This time delay between the arrival of harder and softer photons

shown in figure 3.5 indicates that the hard photons generated in the funnel area close to the black holes are down-scattered at the funnel wall during the propagation to the outer boundary and thus the arrival is delayed. This mechanism is the same as that claimed in Kitaki et al. (2017). We may thus conclude that the spectral variability reflects the geometry of hard X-ray emitting region.

We must admit, however, that it is practically impossible to detect such rapid hard X-ray variation with the existing nor any planned X-ray satellites for the case with stellar-mass black holes. But the timescale will be much longer in cases with massive black holes; on the order of $\sim 400M = 2 \times 10^4 (M/10^6 M_\odot)$ sec. It might then be feasible to detect spectral variations with future mission with good hard X-ray sensitivity. The application to the massive black hole cases will be a future issue (see next section).

3.4 Discussion

In this section we discuss the observational implications, comparison with the past simulation study, and remaining future issues.

3.4.1 Observational implications: case of ULXs

Rather unique ULX spectra, in comparison with the (sub-Eddington) Galactic X-ray binaries containing black holes, also supports the super-Eddington model. There are several distinct spectral states known for the X-ray spectra of ULXs: the broadened disk (BD) state, hard UL state, soft UL state, the supersoft UL (SSUL) state, etc (see, e.g., figure 2 of Kaaret et al. 2017, for typical spectra). Interestingly, some of them (BD and hard UL states) show a rather broad spectral bump in several to 10 keV range, which is consistent with the present study. To be more precise, the hard UL spectra show rapid decay above several keV, whereas the typical X-ray spectrum extends over 10 keV and is very reminiscent of our calculated spectrum (see the right panel of figure 3.2). It is not clear yet why our model is consistent only with one particular state; this issue is left as future subject.

Kitaki et al. (2017) investigate the spectral properties of super-Eddington accretion flows by the Monte-Carlo approach. Their results can explain the typical spectral feature of ULXs, such as the hard excess above several keV. Although the accretion rate they adopted is near the same as that we adopted, the spectral shapes are distinct among the two. Such differences arise because of different fluid model. We find that the gas temperatures differ by a factor of two or more in the optically thick region near the black hole. Much larger differences are found in the funnel region; the temperature in their simulation is $\sim 10^8$ K (see their figures 1 and 2), which is by more than one order of magnitude lower than our fluid data, $\sim 10^9$ K, at most.

What causes such differences? These major differences may arise from the inclusion/absence of general relativistic (GR) effects and/or of magnetic fields, since the data they use is based on the 2D-RHD simulation (which does not include the GR effects nor MHD processes). This is the main reason why the spectrum of our result is much harder than their one.

Narayan et al. (2017) investigated the spectra of super-Eddington flows, incorporating both of the GR and magnetic field effects. Their spectrum of the model SANE (the green line in

their figure 4) is also in good agreement with the BD-state spectra of the ULX. Big differences from ours are that (1) they adopted a large outer boundary of the fluid data; i.e., $10^5 M$, which is 400 times greater than ours, and that (2) they approximately handle the Compton scattering by using the Kompaneets equation and isotropic scattering, while we handle it nearly perfectly by directly solving the Boltzmann equation except for the induced scattering. The difference of the outer boundary may affect the spectrum, as mentioned above (see also their figure 13), since the optical depth of the outflow can become more than our result and because the soft photons from the disk may increase.

The Kompaneets equation is derived under the assumption that the radiation field would be isotropic and that the Fokker-Planck approximation would be a good approximation. In the funnel, the radiation field is highly anisotropic and the energy shift by the single scattering is very large, $\Delta\epsilon/\epsilon > 1$ (with ϵ being the photon energy). This fact should inevitably affect the calculated spectra at high energy regime. They also show the brightness map (see their figure 5), in which the funnel region is clearly seen when viewed from a low viewing angle direction. This feature shares with that of our result.

3.4.2 On the long-term spectral variability of ULX

The ULXs are known to exhibit rather complex X-ray spectral variations. A good example is displayed for the case with Ho IX X-1 (see figure 3 of Vierdayanti et al. 2010), where significant spectral variabilities were found on timescales of several to 100 days or even longer. Obviously, there is no one-to-one correspondence between the spectral shape and the X-ray luminosity. It seems that the broad soft X-ray component (in the range of 0.5 - 5 keV) and the hard X-ray component (above 5 keV) vary independently. In some epoch the former totally dominates with the latter being missing, but in other epoch the latter dominates with the former being weak. There also exists an epoch, at which both components are bright. How can we understand this?

Since the timescale of the spectral variations of a sort that we encounter here is much longer the flaring timescale (see §3.5) the variations cannot be of flare origin. We need to consider variations over much wider spatial range. It is important to note in light of the present analysis that the soft, broad spectral component and the hard-band component have different origins: the latter originates from the funnel region, while the former from the disk and surrounding outflow. The broad soft X-ray component and the hard X-ray component should change in a similar way, as long as the mass accretion rate ($\dot{M}$) is roughly constant in space. The existence of complex spectral variability thus means that accretion should be time-dependent. Suppose that a mass injection rate suddenly increases at large radii, say at several hundreds of $R_{\rm S}$. Then, the enhanced mass inflow is initiated there and propagates inward on the viscous timescale on the order of several days or even longer (see §3.2.3 in Kato et al. 2008). Accordingly, the broad soft X-ray component first grows, as the $\dot{M}$-burst propagates inward, but the hard X-ray component does not respond immediately, since it is generated only in the funnel region. The hard X-ray component starts to rises only after the $\dot{M}$ burst reaches the innermost region.Hence, there exists some time delay, comparable to the viscous timescale, between the rise of the soft X-ray component and that of the hard X-ray one. In this way, we can qualitatively understand the spectral behavior reported in Vierdayanti et al. (2010).

3.4.3 Future prospects

We finally summarize some remaining issues and future works for improvement of the present code.

First, Narayan et al. (2017) also reported an important fact that the emerged spectrum largely change, if we calculate the gas temperature self-consistently with radiation fields. The temperature at the innermost funnel region is much lower than that obtained by the GRRMHD simulation without such consideration, and thus the spectrum is softer. This ultimately requires the calculation of radiation field and fluid simultaneously.

Second, the initial torus should be placed at much larger radius so as to correctly calculate, especially, lower energy spectra. In our calculation, the disk is truncated at $r \sim 250\ M$ or less, whereas soft photons are expected to emerge from more distant regions (see figure13 in Narayan et al. 2017). For this reason, much larger calculation box size in the GRRMHD calculation is necessary. There is another reason why we should put an initial torus at as much larger radius as possible. Kitaki et al. (2020) performed the long-term, large-box RHD simulation of a super-Eddington accretion flow and could achieve the self-consistent (i.e., quasi-steady) steady accretion flow and outflow structure over a large spatial range at $r < 1200\ M$. They report that the calculated outflow rate is much less, by one order of magnitude or even more, compared with the value obtained by previous study, in which quasi-steady state is achieved within a much smaller range (i.e., less than several tens of the Schwarzschild radius). Setting a much larger computation box is needed to avoid artificial results.

CHAPTER 4

Conclusions and Future Issues

4.1 Conclusions

We investigate the properties of super-Eddington accretion flow via numerical simulations and conclude as below:

- The structure of super-Eddington flow can be decompose to three parts: relatively cool and dense disk region with the scale height $H \sim r$, the optically thick and relatively slow ($\sim 0.1c$) outflow region and the jet funnel filled with fast tenuous hot gas ($T_{\rm gas} \gtrsim 10^9 K$).
- The opening angle of the funnel, which can be defined by the photosphere by the electron scattering, is about 30°.
- The spectrum becomes softer when the accretion rate increases. This trend can be easily understood by the $\dot{M}$-dependence of photon trapping radius ($r_{\rm trap} \propto \dot{M}$), i.e., $4\pi r_{\rm trap}^2 \sigma_{\rm SB} T_{\rm eff}^4 = L_{\rm Edd}$.
- The angular dependence of observed spectra, especially in hard X-ray, clearly reflects the structure of the jet funnel, which means the hard X-ray photons emerge only from the funnel region, and thus the larger inclination angle is, the softer the spectrum becomes.
- The flare occurring at the innermost region can be a good tracer to investigate the inclination angle because the variation of hard X-ray photons is sensitive to the inclination angle.

4.2 Future Issues

We finally discuss the remaining issues and future works in the line with this thesis. The Boltzmann radiation solver in this thesis is a milestone for an goal of a complete radiation

hydrodynamic simulation, i.e., the general relativistic frequency-dependent full transfer with hydrodynamics in future. This will solve the radiation processes correctly and solve the fluid properties self-consistently. For this purpose, there are some issues to be solved.

Our code (of course, Newtonian RHD simulations in chapter 2, but even the GR radiation transfer in chapter 3) now cannot calculate the cases, in which a central black hole is rotating. Since Kerr black holes seem to be more common than Schwarzschild black holes in the universe, we need to upgrade our code so as to solve radiative transfer around a spinning black hole. When the rotation of a black hole is prograde, the Blandford-Znajek mechanism will work to possibly produce energetic jet. Narayan et al. (2017) reported the dependence of the spectra on the black hole spin; the spectrum will be notably harder when the black hole is rapidly spinning. This implies that the hardness ratio of the observed spectra may contain useful information regarding the black hole spin.

Compton scattering must be included more correctly. Although the RHD simulation in chapter 2 include the Compton heating/cooling there are large assumptions because of the grey moment equation solver, which are the isotropy of radiation and the Planck distribution. The GR radiation transfer code in chapter 3 improve the treatment of Compton scattering to some extent since this code solve the distribution function of photons in the phase space. However, even this code does not include induced scattering. Although this is a second-order (f^2) effect in Compton scattering, it may play an important role in the mildly optically thick region. In the effectively optically thick region (i.e., in the disk region), frequent absorption and re-emission take place, giving rise to blackbody radiation, and thus scatterings are not so important. In the effectively optically thin but Thomson thick region (i.e., near the funnel wall), by contrast, the Compton scattering could be effective. Since the radiation field in the comoving frame is highly collimated (i.e., more coherent in the momentum space) in the funnel region, especially near the funnel wall, the induced scattering might not be negligible. Since the anisotropy of radiation field is larger in higher energy band ($\gtrsim 10$ keV) in our calculation, the spectrum will be softer than the present result by the contribution of the induced scattering occurring near the funnel wall (with the temperature $T \sim 10$ keV). Hence, we should more accurately calculate the Compton scattering in a future work.

Finally, it would be interesting to apply our methodology to investigate Fe Kα line diagnosis of the super-Eddington flow and moderately sub-Eddington accretion flow, around massive black holes. Calculated line profile variations will be directly compared with future observations by the Athena satellite to explore gas and radiation dynamics (and hopefully space-time geometry, as well) near the black hole (see, e.g, Dovciak et al. 2013). Incidentally, strong Fe line emission is not expected in the simulation data which we used in this study, since the disk surface is very hot, with temperatures exceeding $\sim 10^7$ K, so that metals including Fe will be fully ionized.

We also are interested in the low accretion rate regime. The Compton scattering is also important in the RIAF, especially in the term of observations. In the hot and tenuous gas, the temperatures of protons and electrons are not same because of the larger relaxation time. Although there are many studies to determine the ratio of temperature between proton and electron including magnetic turbulent heating and synchrotron radiation cooling, the inverse Compton scattering effect is also important to decide the electron temperature. The Boltzmann

radiation transfer code we develop can calculate the radiative impact on the electron temperature including the almost correct (which means the induced scattering is negligible because of the low luminosity) radiative process. This calculation will affect the interpretation of observed image such as M87 in Event Horizon Telescope.

References

Abramowicz, M. A., Chen, X., Kato, S., Lasota, J.-P., & Regev, O. 1995, ApJL, 438, L37

Bachetti, M., Harrison, F. A., Walton, D. J., et al. 2014, Nature, 514, 202

Begelman, M. C., & Meier, D. L. 1982, ApJ, 253, 873

Cheng, R. M., & Bogdanović, T. 2014, PhRvD, 90, 064020

Crowther, P. A., Schnurr, O., Hirschi, R., et al. 2010, MNRAS, 408, 731

Di Stefano, R., & Kong, A. K. H. 2003, ApJ, 592, 884

Dolan, J. F., Crannell, C. J., Dennis, B. R., Frost, K. J., & Orwig, L. E. 1979, ApJ, 230, 551

Dolence, J. C., Gammie, C. F., Mościbrodzka, M., & Leung, P. K. 2009, ApJS, 184, 387

Done, C., Gierliński, M., & Kubota, A. 2007, A&A Rv, 15, 1

Dovciak, M., Matt, G., Bianchi, S., et al. 2013, arXiv e-prints, arXiv:1306.2331

Esin, A. A., McClintock, J. E., & Narayan, R. 1997, ApJ, 489, 865

Fabbiano, G., Gioia, I. M., & Trinchieri, G. 1989, ApJ, 347, 127

Falanga, M., Belloni, T., Casella, P., et al., eds. 2015, The Physics of Accretion onto Black Holes (Springer New York), doi:10.1007/978-1-4939-2227-7

Feng, H., & Soria, R. 2011, NewAR, 55, 166

Galeev, A. A., Rosner, R., & Vaiana, G. S. 1979, ApJ, 229, 318

Gilfanov, M., Churazov, E., Sunyaev, R., et al. 1993, A&AS, 97, 303

Gladstone, J. C., Roberts, T. P., & Done, C. 2009, MNRAS, 397, 1836

Greiner, J., Morgan, E. H., & Remillard, R. A. 1996, ApJL, 473, L107

Gu, W.-M., Sun, M.-Y., Lu, Y.-J., Yuan, F., & Liu, J.-F. 2016, ApJL, 818, L4

Haardt, F., & Maraschi, L. 1991, ApJL, 380, L51

Hashizume, K., Ohsuga, K., Kawashima, T., & Tanaka, M. 2015, PASJ, 67, 58

Hirano, S., Hosokawa, T., Yoshida, N., et al. 2014, ApJ, 781, 60

Ichimaru, S. 1977, ApJ, 214, 840

Kaaret, P., Feng, H., & Roberts, T. P. 2017, ARA&A, 55, 303

Kato, S., Fukue, J., & Mineshige, S. 2008, Black-Hole Accretion Disks — Towards a New Paradigm — (Kyoto University Press)

Kawashima, T., Ohsuga, K., Mineshige, S., et al. 2009, PASJ, 61, 769

Kawashima, T., Ohsuga, K., Mineshige, S., et al. 2012, ApJ, 752, 18

Kitaki, T., Mineshige, S., Ohsuga, K., & Kawashima, T. 2017, PASJ, 69, 92

Kitaki, T., Mineshige, S., Ohsuga, K., & Kawashima, T. 2020, PASJ,submitted

Kong, A. K. H., Di Stefano, R., & Yuan, F. 2004, ApJL, 617, L49

Levermore, C. D., & Pomraning, G. C. 1981, ApJ, 248, 321

Liang, E. P., & Nolan, P. L. 1984, SSRv, 38, 353

Liu, J. 2011, ApJS, 192, 10

Liu, J.-F. 2008, ApJS, 177, 181

Liu, J.-F., Bai, Y., Wang, S., et al. 2015, Nature, 528, 108

Makishima, K. 2007, in Black Holes from Stars to Galaxies – Across the Range of Masses, ed. V. Karas & G. Matt, Vol. 238, 209–218

Makishima, K., Kubota, A., Mizuno, T., et al. 2000, ApJ, 535, 632

Martocchia, A., & Matt, G. 1996, MNRAS, 282, L53

McClintock, J. E., Narayan, R., Davis, S. W., et al. 2011, Classical and Quantum Gravity, 28, 114009

Miller, M. C., & Hamilton, D. P. 2002, MNRAS, 330, 232

Miniutti, G., & Fabian, A. C. 2004, MNRAS, 349, 1435

Miyamoto, S., Iga, S., Kitamoto, S., & Kamado, Y. 1993, ApJL, 403, L39

Mościbrodzka, M., Falcke, H., Shiokawa, H., & Gammie, C. F. 2014, A&A, 570, A7

Motch, C., Pakull, M. W., Soria, R., Grisé, F., & Pietrzyński, G. 2014, Nature, 514, 198

Nagakura, H., Sumiyoshi, K., & Yamada, S. 2014, ApJS, 214, 16

Narayan, R., SaÌ§dowski, A., & Soria, R. 2017, MNRAS, 469, 2997

Narayan, R., & Yi, I. 1994, ApJL, 428, L13

Oda, M., Gorenstein, P., Gursky, H., et al. 1971, ApJL, 166, L1

Ohsuga, K., & Mineshige, S. 2014, SSRv, 183, 353

Ohsuga, K., Mori, M., Nakamoto, T., & Mineshige, S. 2005, ApJ, 628, 368

Pakull, M. W., & Mirioni, L. 2002, arXiv e-prints, astro

Pakull, M. W., & Mirioni, L. 2003, in Revista Mexicana de Astronomia y Astrofisica Conference Series, Vol. 15, Revista Mexicana de Astronomia y Astrofisica Conference Series, ed. J. Arthur & W. J. Henney, 197–199

Pozdnyakov, L. A., Sobol, I. M., & Syunyaev, R. A. 1977, Soviet Ast., 21, 708

Rees, M. J., Begelman, M. C., Blandford, R. D., & Phinney, E. S. 1982, Nature, 295, 17

Rybicki, G. B., & Lightman, A. P. 1979, Radiative processes in astrophysics (A Wiley-Interscience Publication)

Shakura, N. I., & Sunyaev, R. A. 1973, A&A, 500, 33

Shibata, M., Nagakura, H., Sekiguchi, Y., & Yamada, S. 2014, Phys. Rev. D, 89, 084073

Sądowski, A., Narayan, R., Tchekhovskoy, A., et al. 2015, MNRAS, 447, 49

Soria, R., Long, K. S., Blair, W. P., et al. 2014, Science, 343, 1330

Sumiyoshi, K., & Yamada, S. 2012, ApJS, 199, 17

Susa, H., Hasegawa, K., & Tominaga, N. 2014, ApJ, 792, 32

Takahashi, H. R., Mineshige, S., & Ohsuga, K. 2018, ApJ, 853, 45

Takahashi, R., & Umemura, M. 2017, MNRAS, 464, 4567

Takeuchi, S., Ohsuga, K., & Mineshige, S. 2013, PASJ, 65, 88

Takeuchi, S., Ohsuga, K., & Mineshige, S. 2014, PASJ, 66, 48

Tananbaum, H., Gursky, H., Kellogg, E., Giacconi, R., & Jones, C. 1972, ApJL, 177, L5

Urquhart, R., & Soria, R. 2016, MNRAS, 456, 1859

van der Klis, M. 1994, ApJS, 92, 511

Vierdayanti, K., Mineshige, S., & Ueda, Y. 2010, PASJ, 62, 239

Vilhu, O. 1999, in Astronomical Society of the Pacific Conference Series, Vol. 161, High Energy Processes in Accreting Black Holes, ed. J. Poutanen & R. Svensson, 82

Walton, D. J., Roberts, T. P., Mateos, S., & Heard, V. 2011, MNRAS, 416, 1844

Watarai, K., Mizuno, T., & Mineshige, S. 2001, ApJL, 549, L77

Wiktorowicz, G., Sobolewska, M., Sądowski, A., & Belczynski, K. 2015, ApJ, 810, 20

Wu, X.-B., Wang, F., Fan, X., et al. 2015, Nature, 518, 512

Yamada, S., Makishima, K., Done, C., et al. 2013, PASJ, 65, 80

Yuan, F., & Narayan, R. 2014, ARA&A, 52, 529

Yusof, N., Hirschi, R., Meynet, G., et al. 2013, MNRAS, 433, 1114

APPENDIX A

FORMULATION FOR GENERAL RELATIVISTIC RADIATION MOMENT EQUATION

In this section, we will formulate the general relativistic radiation moment equation for numerical simulation.

A.1 Tensor field equation of k-th radiative moments

First of all, we begin with Boltzmann equation for photons.

$$\frac{dx^\alpha}{d\tau}\frac{\partial f}{\partial x^\alpha} + \frac{dp^i}{d\tau}\frac{\partial f}{\partial p^i} = (-p^\alpha u_\alpha) S(p^\mu, x^\mu, f) \tag{A.1}$$

where $\{x^\mu, p^\mu\}$ is a coordinate set on phase space (in mathematical term, a phase space is a subset of tangent bundle), τ is a affine parameter for photon tragectory and u^α is velocity of fluid. Here,

$$p^\mu = \frac{dx^\mu}{d\tau} \tag{A.2}$$

and for massless particle, since its trajectory is null geodesic,

$$\frac{dp^\mu}{d\tau} + \Gamma^\mu_{\nu\rho} p^\nu p^\rho = 0 \qquad . \tag{A.3}$$

Instituting equations (A.2) and (A.3) to Boltzmann equation (A.1), we get the relation

$$p^\alpha \frac{\partial f}{\partial x^\alpha} - \Gamma^i_{\nu\rho} p^\nu p^\rho \frac{\partial f}{\partial p^i} = (-p^\alpha u_\alpha) S(p^\mu, x^\mu, f) \tag{A.4}$$

Next, the definition of k-th moment tensor $M^{A_k}_{(\nu)} := M^{\alpha_1\alpha_2\cdots\alpha_k}_{(\nu)}$ for radiation field with frequency ν can be written as

$$\begin{aligned} M^{\alpha_1\alpha_2\cdots\alpha_k}_{(\nu)} &:= \nu^3 \int f(\nu,\Omega,x^\mu)(u^{\alpha_1}+\ell^{\alpha_1})(u^{\alpha_2}+\ell^{\alpha_2})\cdots(u^{\alpha_k}+\ell^{\alpha_k})d\Omega \\ &= \int \frac{f\delta(\mathbf{p}\cdot\mathbf{u}+\nu)}{(-\mathbf{p}\cdot\mathbf{u})^{k-2}} p^{\alpha_1}p^{\alpha_2}\cdots p^{\alpha_k}(-\mathbf{p}\cdot\mathbf{u})dV_{\boldsymbol{p}} \end{aligned} \tag{A.5}$$

where ℓ^α is a unit spacelike vector with $\ell^\alpha\ell_\alpha = 1, u^\alpha\ell_\alpha = 0$, Ω is solid angle associated with ℓ,$dV_{\boldsymbol{p}} = (-\mathbf{p}\cdot\mathbf{u})\Omega d(-\mathbf{p}\cdot\mathbf{u})$ is the invariant volume element of the momentum space and δ is the Dirac delta function. It is notable that $p^\alpha = (-p^\mu u_\mu)(u^\alpha + \ell^\alpha)$. Since we can choose the Riemann normal coordinates as the local coordinates in any case and it is very convenient to calculate covariant derivatives of tensor field because of vanishing the Christoffel symbols, we choose this coordinates. Then, the Boltzmann equation is transformed to

$$p^\alpha \frac{\partial f}{\partial x^\alpha} = (-p^\alpha u_\alpha) S(p^\mu, x^\mu, f). \tag{A.6}$$

This is the time to formulate the k-th moment tensor equation. We begin with calculating the covariant derivative ∇_β of $M^{A_k\beta}_{(\nu)}$. Since choosing Riemann normal coordinates and the

coordinate derivatives work only on f and $\boldsymbol{u}$,

$$
\begin{aligned}
\nabla_\beta M^{A_k\beta}_{(\nu)} =& \partial_\beta M^{A_k\beta}_{(\nu)} \\
=& \int (\partial_\beta f)\delta(\mathbf{p}\cdot\mathbf{u}+\nu)(-\mathbf{p}\cdot\mathbf{u})^{-k+1}p^{\alpha_1}p^{\alpha_2}\cdots p^{\alpha_k}p^\beta dV_{\boldsymbol{p}} \\
&+ \int f\partial_\beta(\delta(\mathbf{p}\cdot\mathbf{u}+\nu)(-\mathbf{p}\cdot\mathbf{u})^{-k+1})p^{\alpha_1}p^{\alpha_2}\cdots p^{\alpha_k}p^\beta dV_{\boldsymbol{p}} \\
=& \nu^3\int S(u^{\alpha_1}+\ell^{\alpha_1})(u^{\alpha_2}+\ell^{\alpha_2})\cdots(u^{\alpha_k}+\ell^{\alpha_k})d\Omega \qquad \text{(from equation A.6)} \\
&- \int f p^\mu\partial_\beta u_\mu(-k+1)(-\mathbf{p}\cdot\mathbf{u})^{-k}\delta(\mathbf{p}\cdot\mathbf{u}+\nu)p^{\alpha_1}p^{\alpha_2}\cdots p^{\alpha_k}p^\beta dV_{\boldsymbol{p}} \\
&- \int f p^\mu\partial_\beta u_\mu\frac{\partial}{\partial(-\mathbf{p}\cdot\mathbf{u})}\delta(\mathbf{p}\cdot\mathbf{u}+\nu)(-\mathbf{p}\cdot\mathbf{u})^{-k+1}p^{\alpha_1}p^{\alpha_2}\cdots p^{\alpha_k}p^\beta dV_{\boldsymbol{p}} \\
=& S^{A_k}_{(\nu)} + (k-1)M^{A_k\beta\gamma}_{(\nu)}\partial_\beta u_\gamma \\
&- \int \left[f p^\mu\partial_\beta u_\mu(-\mathbf{p}\cdot\mathbf{u})^{-k+2}p^{\alpha_1}p^{\alpha_2}\cdots p^{\alpha_k}p^\beta\delta(\mathbf{p}\cdot\mathbf{u}+\nu)\right]\Big|^{-\mathbf{p}\cdot\mathbf{u}=\infty}_{-\mathbf{p}\cdot\mathbf{u}=0}d\Omega \qquad \text{(integration by parts)} \\
&+ \int \delta(\mathbf{p}\cdot\mathbf{u}+\nu)\frac{\partial}{\partial(-\mathbf{p}\cdot\mathbf{u})}\left[f p^\mu\partial_\beta u_\mu(-\mathbf{p}\cdot\mathbf{u})^{-k+2}p^{\alpha_1}p^{\alpha_2}\cdots p^{\alpha_k}p^\beta\right]d\Omega d(-\mathbf{p}\cdot\mathbf{u}) \\
=& S^{A_k}_{(\nu)} + (k-1)M^{A_k\beta\gamma}_{(\nu)}\partial_\beta u_\gamma \\
&+ \int d\Omega d(-\mathbf{p}\cdot\mathbf{u})\delta(\mathbf{p}\cdot\mathbf{u}+\nu) \\
&\quad \frac{\partial}{\partial(-\mathbf{p}\cdot\mathbf{u})}\left[f\partial_\beta u_\gamma(-\mathbf{p}\cdot\mathbf{u})^4(u^{\alpha_1}+\ell^{\alpha_1})(u^{\alpha_2}+\ell^{\alpha_2})\cdots(u^{\alpha_k}+\ell^{\alpha_k})(u^\beta+\ell^\beta)(u^\gamma+\ell^\gamma)\right] \\
=& S^{A_k}_{(\nu)} + (k-1)M^{A_k\beta\gamma}_{(\nu)}\partial_\beta u^\gamma \\
&+ \int d(-\mathbf{p}\cdot\mathbf{u})\delta(\mathbf{p}\cdot\mathbf{u}+\nu)\left[(-\mathbf{p}\cdot\mathbf{u})M^{A_k\beta\gamma}_{(-\mathbf{p}\cdot\mathbf{u})}\partial_\beta u_\gamma\right] \\
=& \frac{\partial}{\partial\nu}(\nu M^{A_k\beta\gamma}_{(\nu)}\partial_\beta u_\gamma) + S^{A_k} + (k-1)M^{A_k\beta\gamma}_{(\nu)}\partial_\beta u^\gamma \\
=& \frac{\partial}{\partial\nu}(\nu M^{A_k\beta\gamma}_{(\nu)}\nabla_\beta u_\gamma) + S^{A_k} + (k-1)M^{A_k\beta\gamma}_{(\nu)}\nabla_\beta u^\gamma
\end{aligned}
\tag{A.7}
$$

where $dV_{\boldsymbol{p}}$ is invariant against the Lorentz transformation (i.e. invariant against to changing Eulerian observer moving with $\boldsymbol{u}$) and S^{A_k} is defined as

$$
S^{A_k}_{(\nu)} := \nu^3\int S(u^{\alpha_1}+\ell^{\alpha_1})(u^{\alpha_2}+\ell^{\alpha_2})\cdots(u^{\alpha_k}+\ell^{\alpha_k})d\Omega. \tag{A.8}
$$

Therefore, we conclude this formulation as

$$
\nabla_\beta M^{A_k\beta}_{(\nu)} - \frac{\partial}{\partial\nu}(\nu M^{A_k\beta\gamma}_{(\nu)}\nabla_\gamma u_\beta) - (k-1)M^{A_k\beta\gamma}_{(\nu)} = S^{A_k}_{(\nu)}. \tag{A.9}
$$

Particularly, taking the 1st moment equation, we get

$$
\nabla_\beta M^{\alpha\beta}_{(\nu)} - \frac{\partial}{\partial\nu}(\nu M^{\alpha\beta\gamma}_{(\nu)}\nabla_\gamma u_\beta) = S^{\alpha}_{(\nu)}. \tag{A.10}
$$

Integrating equation (A.10) over frequency, we get

$$\nabla_\beta M^{\alpha\beta} = S^\alpha \tag{A.11}$$

where

$$M^{\alpha\beta} := \int_0^\infty d\nu M^{\alpha\beta}_{(\nu)}, \qquad S^{A_k} := \int_0^\infty d\nu S^\alpha_{(\nu)}. \tag{A.12}$$

Considering the radiation decouples the matter, $\nabla_\beta M^{\alpha\beta} = 0$, which is the property of energy-momentum tensor. Yes, $M^{\alpha\beta}$ is nothing other than the energy-momentum tensor of radiation. From the definition, the radiation energy-momentum tensor is clearly traceless.

A.2 Conservative Form of Radiation Moment Equation

By doing 3+1 decomposition of tensor equation, we transform equation (A.10) into the conservative form of radiation moment equation and we get:

$$\begin{aligned}
&\partial_t(\sqrt{\gamma}E_{(\nu)}) + \partial_j[\sqrt{\gamma}(\alpha F^j_{(\nu)} - \beta^j E_{(\nu)})] + \frac{\partial}{\partial\nu}\left(\nu\alpha\sqrt{\gamma}n_\alpha M^{\alpha\beta\gamma}\nabla_\gamma u_\beta\right) \\
&\qquad = \alpha\sqrt{\gamma}[P^{ij}_{(\nu)}K_{ij} - F^j_{(\nu)}\partial_j \ln\alpha - S^\alpha_{(\nu)}n_\alpha] \qquad \text{(A.13)} \\
&\partial_t(\sqrt{\gamma}F_{(\nu)i}) + \partial_j[\sqrt{\gamma}(\alpha P^j_{(\nu)i} - \beta^j F_{(\nu)i})] - \frac{\partial}{\partial\nu}\left(\nu\alpha\sqrt{\gamma}\gamma_{i\alpha}M^{\alpha\beta\gamma}\nabla_\gamma u_\beta\right) \\
&\qquad = \sqrt{\gamma}\left[-E_{(\nu)}\partial_i\alpha + F_{(\nu)k}\partial_i\beta^k + \frac{\alpha}{2}P^{jk}_{(\nu)}\partial_i\gamma_{jk} + \alpha S^\alpha_{(\nu)}\gamma_{i\alpha}\right] \qquad \text{(A.14)}
\end{aligned}$$

where of course

$$E_{(\nu)} := \mathbf{M}_{(\nu)}(\underline{\boldsymbol{n}}, \underline{\boldsymbol{n}}) := M^{\alpha\beta}_{(\nu)}n_\alpha n_\beta \tag{A.15}$$

$$\boldsymbol{F}_{(\nu)} := -\vec{\boldsymbol{\gamma}}(\cdot, \mathbf{M}_{(\nu)}(\underline{\boldsymbol{n}}, \cdot)) := -M^{\alpha\beta}_{(\nu)}n_\alpha\gamma^\mu{}_\beta \tag{A.16}$$

$$\boldsymbol{P}_{(\nu)} := \vec{\boldsymbol{\gamma}}^*\mathbf{M}_{(\nu)} := M^{\alpha\beta}_{(\nu)}\gamma^\mu{}_\alpha\gamma^\nu{}_\beta \tag{A.17}$$

and $\alpha, \boldsymbol{\beta}, \boldsymbol{K}, \boldsymbol{n}, \gamma_{ij}, \gamma$ are the lapse function of its folliation $\{\Sigma_t\}_{t\in\mathbb{R}}$, the shift vector, the extrinsic curvature on Σ_t, unit vector normal to Σ_t, the metric matrix on Σ_t with respect to the coordinates (x^α) and the determinant of γ_{ij}, respectively.

APPENDIX B

DETAIL FOR BOLTZMANN SOLVER

B.1 Derivation of Basic Equation

In this section, we derive the basic equation following Shibata et al. (2014).

In General, Boltzmann equation is written as

$$\frac{dx^\alpha}{d\tau}\frac{\partial f}{\partial x^\alpha} + \frac{dp^i}{d\tau}\frac{\partial f}{\partial p^i} = (-p^\alpha \hat{u}_\alpha)C[f] \tag{B.1}$$

$$\frac{dx^\alpha}{d\tau}\frac{\partial f}{\partial x^\alpha} + \frac{dp^i}{d\tau}\frac{\partial f}{\partial p^i} = (-p^\alpha \hat{u}_\alpha)S_{rad}(f, x^\mu, p^\mu) \tag{B.2}$$

where f is the distribution function which is the function of 4-spacetime (x^1, x^2, x^3, x^4) and 3-momentum space (p^1, p^2, p^3), τ is affine parameter of trajectory, $\hat{u}^\alpha$ is a arbitrary timelike vector (which may be fluid vector or 4-vector of Eulerian observer) and C is the collision term which is the function of distribution function and properties of Collisional source such as gas temperature and density. Hereafter we use the Einstein notation and Latin dummy indices run over 3-space ({1,2,3}) and Greek ones run over 4-spacetime ({0,1,2,3}).

In the case of photons, $p^\alpha = dx^\alpha/d\tau$ and the equation of motion is very simple and can be written as null geodesic equation:

$$\frac{dp^\alpha}{d\tau} + \Gamma^\alpha_{\mu\nu} p^\mu p^\nu = 0 \tag{B.3}$$

where $\Gamma^\alpha_{\mu\nu}$ is the Christoffel symbol defined by spacetime metric $g_{\mu\nu}$ as

$$\Gamma^\alpha_{\beta\gamma} = \frac{1}{2} g^{\alpha\nu}(\partial_\beta g_{\nu\gamma} + \partial_\gamma g_{\nu\beta} - \partial_\nu g_{\beta\gamma}). \tag{B.4}$$

Using this relation, equation (B.1) can be written as

$$p^\alpha \frac{\partial f}{\partial x^\alpha} - \Gamma^i_{\mu\nu} p^\mu p^\nu \frac{\partial f}{\partial p^i} = (-p^\alpha \hat{u}_\alpha) C[f] \tag{B.5}$$

It is notable that this equation will be reduced into the usual radiation transfer equation $\frac{1}{c}\partial_t I_\nu + \boldsymbol{n} \cdot \nabla I_\nu = C\nu^3$ (where I_ν is the specific intensity) in Newtonian case ($\Gamma^\alpha_{\beta\gamma} = 0$).
In equation (B.5), the variables indicates 4-spacetime and 3-momentum space. 3-momentum space can be understood more easily when splitting momentum space into the direction of photon and its energy. So we must rewrite equation (B.5) as the equation explicitly depending on 4-spacetime and frequency and direction. This means we use the spherical coordinate system for 3-momentum space.

When applying to Black hole accretion disk, it is convenient to use the spherical coordinate (r, θ, ϕ) in 3-space and so we use this one. After that, we can set the spherical coordinate $(\nu, \bar{\theta}, \bar{\varphi})$ in the momentum space as figure B.1. In momentum space, we can use the orthonormal basis $e^\beta_{(\alpha)}$ (which satisfies $g_{\mu\nu} e^\mu_{(\alpha)} e^\nu_{(\beta)} = \eta_{\alpha\beta}$) to measure the real length. The timelike vector $e^\mu_{(0)}$ is the 4-velocity of the observer, and the projection of p^α on the vector shows the frequency of photons observed by him (for example, when setting $e^\mu_{(0)}$ to the fluid 4-velocity u^μ, the projection $\nu = -p^\mu u_\mu$ is the frequency measured on the fluid rest frame). After setting the timelike vector $e^\mu_{(0)}$, there are 3 degrees of freedom which corresponds to the dimension of rotational group $SO(3)$. Anyway to set these basis, the photon's 4-momentum p^α (which satisfies the null condition $p^\mu p_\mu = 0$) can be decomposed as

$$p^\alpha = \nu(e^\alpha_{(0)} + \sum_{i=1}^{3} C_{(i)} e^\alpha_{(i)}) \tag{B.6}$$

where the coefficients $C_{(i)}$ can be written as

$$C_{(1)} = \cos\bar{\theta}, \;\; C_{(2)} = \sin\bar{\theta}\cos\bar{\varphi}, \;\; C_{(3)} = \sin\bar{\theta}\sin\bar{\varphi} \tag{B.7}$$

where the angles $\bar{\theta}, \bar{\varphi}$ are the polar angle measured from $e^\mu_{(1)}$ and the azimuthal angle measured from $e^\mu_{(2)}$, respectively. This is just an analog to the usual cartesian coordinate written by spherical values (i.e. $(x, y, z) = (r\sin\theta\cos\phi, r\sin\theta\sin\phi, r\cos\theta)$). Here we set orthonormal basis as figure B.1, so that $(e^\mu_{(1)}, e^\mu_{(2)}, e^\mu_{(3)})$ are the unit vectors directing to r, θ, ϕ directions, respectively. After setting coordinates on the phase space, we can transform the basic equation (B.1) into the coordinate description as

$$\frac{dx^\alpha}{d\tau}\frac{\partial f}{\partial x^\alpha} + \frac{d\nu}{d\tau}\frac{\partial f}{\partial \nu} + \frac{d\bar{\theta}}{d\tau}\frac{\partial f}{\partial \bar{\theta}} + \frac{d\bar{\varphi}}{d\tau}\frac{\partial f}{\partial \bar{\varphi}} = (-p^\alpha \hat{u}_\alpha) S_{rad}(f, x^\mu, p^\mu) \tag{B.8}$$

and these derivatives of coordinates $(\nu, \bar{\theta}, \bar{\varphi})$ are

$$\begin{aligned}
\frac{d\nu}{d\tau} &= -\frac{d}{d\tau}(p^\alpha e_{(0)\alpha}) \\
&= -p^\beta \nabla_\beta (p^\alpha e_{(0)\alpha}) \\
&= -p_\alpha p^\beta \nabla_\beta e^\alpha_{(0)} \\
\frac{d\bar{\theta}}{d\tau} &= \frac{d}{d\tau} \tan^{-1}\left(\frac{\sqrt{p^2_{(2)} + p^2_{(3)}}}{p_{(1)}}\right) \\
&= \frac{1}{\nu}\left(-\sin\bar{\theta}\frac{dp_{(1)}}{d\tau} + \cos\bar{\theta}\cos\bar{\varphi}\frac{dp_{(2)}}{d\tau} + \cos\bar{\theta}\sin\bar{\varphi}\frac{dp_{(3)}}{d\tau}\right) \\
&= \frac{1}{\nu}\sum_{j=1}^{3}\frac{\partial C_{(j)}}{\partial\bar{\theta}}\frac{dp_{(j)}}{d\tau} = \frac{1}{\nu}\sum_{j=1}^{3}\frac{\partial C_{(j)}}{\partial\bar{\theta}} p^\alpha p_\beta \nabla_\alpha e^\beta_{(j)} \\
\frac{d\bar{\varphi}}{d\tau} &= \frac{d}{d\tau}\tan^{-1}\left(\frac{p_{(3)}}{p_{(2)}}\right) \\
&= \frac{1}{\nu\sin^2\bar{\theta}}\left(-\sin\bar{\theta}\sin\bar{\varphi}\frac{dp_{(2)}}{d\tau} + \sin\bar{\theta}\cos\bar{\varphi}\frac{dp_{(3)}}{d\tau}\right) \\
&= \frac{1}{\nu\sin^2\bar{\theta}}\sum_{j=1}^{3}\frac{\partial C_{(j)}}{\partial\bar{\varphi}}\frac{dp_{(j)}}{d\tau} = \frac{1}{\nu\sin^2\bar{\theta}}\sum_{j=1}^{3}\frac{\partial C_{(j)}}{\partial\bar{\varphi}} p^\alpha p_\beta \nabla_\alpha e^\beta_{(j)}.
\end{aligned} \tag{B.9}$$

According to these equations and $p^\beta \nabla_\beta p^\alpha = 0$, we can get the conservative form of the Boltzmann equation as

$$\begin{aligned}
&\frac{1}{\sqrt{-g}}\left.\frac{\partial\left(\sqrt{-g}\nu^{-1}p^\alpha f\right)}{\partial x^\alpha}\right|_{q_{(i)}} + \frac{1}{\nu^2}\frac{\partial}{\partial\nu}\left(-\nu f p^\alpha p_\beta \nabla_\alpha e^\beta_{(0)}\right) \\
&+ \frac{1}{\sin\bar{\theta}}\frac{\partial}{\partial\bar{\theta}}\left(\nu^{-2}\sin\bar{\theta} f\sum_{j=1}^{3} p^\alpha p_\beta \nabla_\alpha e^\beta_{(j)}\frac{\partial C_{(j)}}{\partial\bar{\theta}}\right) \\
&+ \frac{1}{\sin^2\bar{\theta}}\frac{\partial}{\partial\bar{\varphi}}\left(\nu^{-2} f\sum_{j=2}^{3} p^\alpha p_\beta \nabla_\alpha e^\beta_{(j)}\frac{\partial C_{(j)}}{\partial\bar{\varphi}}\right) = S_{\mathrm{rad}}.
\end{aligned} \tag{B.10}$$

Another description of the conservative form is written clearly as

$$\begin{aligned}
&\frac{1}{\sqrt{-g}}\frac{\partial}{\partial x^\alpha}\Big|_{q_{(i)}}\left[\left(e^\alpha_{(0)} + \sum_{i=1}^{3}\ell_{(i)}e^\alpha_{(i)}\right)\sqrt{-g}f\right] \\
&- \frac{1}{\nu^2}\frac{\partial}{\partial\nu}\left(\nu^3 f\omega_{(0)}\right) + \frac{1}{\sin\bar{\theta}}\frac{\partial}{\partial\bar{\theta}}\left(\sin\bar{\theta} f\omega_{(\bar{\theta})}\right) \\
&+ \frac{1}{\sin^2\bar{\theta}}\frac{\partial}{\partial\bar{\varphi}}\left(f\omega_{(\bar{\varphi})}\right) = S_{\mathrm{rad}}
\end{aligned} \tag{B.11}$$

where the coefficients are defined by

$$\omega_{(0)} \equiv \nu^{-2} p^\alpha p_\beta \nabla_\alpha e^\beta_{(0)} = \sum_{i=1}^{3} C_{(i)} \left(\gamma_{i00} + \sum_{j=1}^{3} \gamma_{i0j} C_{(j)} \right) \tag{B.12}$$

$$\omega_{(\bar{\theta})} \equiv \sum_{j=1}^{3} \omega_{(j)} \frac{\partial C_{(j)}}{\partial \bar{\theta}} \tag{B.13}$$

$$\omega_{(\bar{\varphi})} \equiv \sum_{j=2}^{3} \omega_{(j)} \frac{\partial C_{(j)}}{\partial \bar{\varphi}} \tag{B.14}$$

$$\omega_{(j)} \equiv \nu^{-2} p^\alpha p_\beta \nabla_\alpha e^\beta_{(j)} = \gamma_{0j0} + \sum_{i=1}^{3} C_{(i)} \left\{ (\gamma_{0ji} + \gamma_{ij0}) + \sum_{k=1}^{3} \gamma_{ijk} C_{(k)} \right\} \tag{B.15}$$

$$\gamma_{\alpha\beta\gamma} \equiv e^a_{(\alpha)} e^b_\gamma \nabla_b \left(e_{(\beta)} \right)_a \tag{B.16}$$

and $\gamma_{\alpha\beta\gamma}$ are called Ricci rotational coefficients which measure the rotation of frame vector when moved in every direction.

The conservative form of the Boltzmann equation can be derived straightforwardly as below.

$$p^\alpha \left.\frac{\partial f}{\partial x^\alpha}\right|_{p^j} = \frac{1}{-g} \frac{\partial \left[f \left(-g \right) p^\alpha \right]}{\partial x^\alpha} - 2 p^\alpha \Gamma^\beta_{\alpha\beta} f - f \left.\frac{\partial p^t}{\partial t}\right|_{p^j} \tag{B.17}$$

$$\left.\frac{\partial p^t}{\partial t}\right|_{p^j} = - \frac{1}{p_t} \frac{dp_t}{dt} \tag{B.18}$$

$$- \Gamma^i_{\alpha\beta} p^\alpha p^\beta \left.\frac{\partial f}{\partial p^i}\right|_{x^\mu} = - \left.\frac{\partial}{\partial p^i} \left(f \Gamma^i_{\alpha\beta} p^\alpha p^\beta \right)\right|_\mu + 2 f p^\alpha \left(\Gamma^i_{i\alpha} + \Gamma^i_{t\alpha} \left.\frac{\partial p^t}{\partial p^i}\right|_{x^\mu} \right) \tag{B.19}$$

$$\Gamma^i_{t\alpha} \left.\frac{\partial p^t}{\partial p^i}\right|_{x^\mu} = - \Gamma^i_{t\alpha} \frac{p_i}{p_t} = - \Gamma^i_{t\alpha} \frac{p_\beta}{p_t} + \Gamma^t_{t\alpha} \tag{B.20}$$

$$\begin{aligned} \frac{dp_t}{d\tau} &= \frac{dx^\alpha}{d\tau} \left.\frac{\partial p_t}{\partial x^\alpha}\right|_{p^i} + \left.\frac{dp^i}{d\tau} \frac{\partial p_t}{\partial p^i}\right|_{x^\mu} \\ &= p^\alpha \left.\frac{\partial p_t}{\partial x^\alpha}\right|_{p^i} - \Gamma^i_{\alpha\beta} p^\alpha p^\beta \left.\frac{\partial p_t}{\partial p_i}\right|_{x^\mu} \end{aligned} \tag{B.21}$$

Combining equations (B.17),(B.18),(B.19),(B.20),(B.21) and (B.5), we can achieve the conservative form of natural coordinates as

$$\frac{p_t}{(-g)} \left[\frac{\partial}{\partial x^\alpha} \left(\frac{f \left(-g \right) p^\alpha}{p_t} \right) - \frac{\partial}{\partial p^i} \left(\frac{f \left(-g \right)}{p_t} \Gamma^i_{\alpha\beta} p^\alpha p^\beta \right) \right] = \left(-p_a \hat{u}^\alpha \right) S_{\text{rad}} \tag{B.22}$$

B.1.1 Conservative form of Schwarzschild spacetime

In the Schwarzschild spacetime, the metric is written as

$$ds^2 = - \left(1 - \frac{2M}{r} \right) dt^2 + \left(1 - \frac{2M}{r} \right)^{-1} dr^2 + r^2 \left(d\theta^2 + \sin^2 \theta d\varphi^2 \right), \tag{B.23}$$

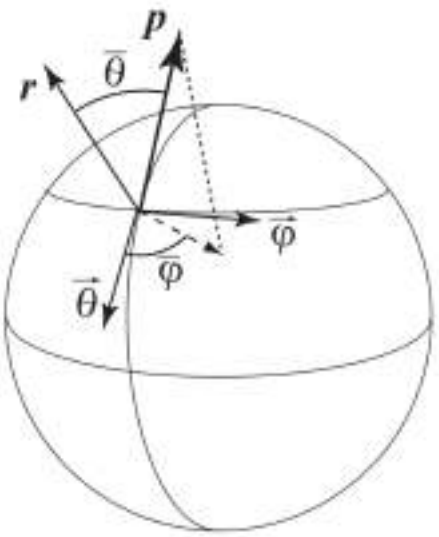

Fig. B.1 The schematic image for setting coordinate system on momentum space. The polar angle $\bar{\theta}$ on momentum space of (spatial) point $\boldsymbol{r}$ is defined as the angle between position vector $\boldsymbol{r}$ and 3-momentum vector $\boldsymbol{p}$, and the azimuthal angle $\bar{\varphi}$ is defined as the angle between the vertical component of $\boldsymbol{p}$ with respect to $\boldsymbol{r}$ and the unit vector $\vec{\theta}$ parallel to θ direction on 3-space. (from Shibata et al. 2014)

where the coordinates (t, r, θ, φ) are the usual Schwarzschild coordinates. We can choose a tetrad as below:

$$
\begin{aligned}
e^{\alpha}_{(0)} &= \left(1 - \frac{2M}{r}\right)^{-1/2} \left(\frac{\partial}{\partial t}\right)^{\alpha}, \\
e^{\alpha}_{(1)} &= \left(1 - \frac{2M}{r}\right)^{1/2} \left(\frac{\partial}{\partial r}\right)^{\alpha}. \\
e^{\alpha}_{(2)} &= \frac{1}{r} \left(\frac{\partial}{\partial \theta}\right)^{\alpha}, \\
e^{\alpha}_{(3)} &= \frac{1}{r \sin\theta} \left(\frac{\partial}{\partial \varphi}\right)^{\alpha}.
\end{aligned} \tag{B.24}
$$

where $e^{\alpha}_{(0)}$ is a timelike vector and $e^{\alpha}_{(i)}$ are spacelike vectors only in the region $r > 2M$. After setting the tetrad, we can calculate the Ricci rotation coefficients:

$$
\gamma_{122} = -\gamma_{212} = \gamma_{133} = -\gamma_{313} = -\frac{1}{r}\left(1 - \frac{2M}{r}\right)^{1/2}, \tag{B.25}
$$

$$
\gamma_{233} = -\gamma_{323} = -\frac{\cot\theta}{r}, \tag{B.26}
$$

$$
\gamma_{100} = -\gamma_{010} = \frac{M}{r^2}\left(1 - \frac{2m}{r}\right)^{-1/2}. \tag{B.27}
$$

Using $\gamma_{\alpha\beta\gamma}$ and equations (B.12)(B.13)(B.14)(B.15), the coefficients in conservative form of orthonormal frame can be calculated as

$$\omega_{(0)} = \frac{M}{r^2}\left(1-\frac{2M}{r}\right)^{-1/2}\cos\bar{\theta}, \tag{B.28}$$

$$\omega_{(1)} = -\frac{m}{r^2}\left(1-\frac{2M}{r}\right)^{-1/2} + \frac{1}{r}\left(1-\frac{2M}{r}\right)^{1/2}\sin^2\bar{\theta}, \tag{B.29}$$

$$\omega_{(2)} = -\frac{1}{r}\left(1-\frac{2M}{r}\right)^{1/2}\sin\bar{\theta}\cos\bar{\theta}\cos\bar{\varphi} + \frac{\cot\theta}{r}\sin^2\bar{\theta}\sin^2\bar{\varphi}, \tag{B.30}$$

$$\omega_{(3)} = -\frac{1}{r}\left(1-\frac{2M}{r}\right)^{1/2}\sin\bar{\theta}\cos\bar{\theta}\sin\bar{\varphi} - \frac{\cot\theta}{r}\sin^2\bar{\theta}\sin\bar{\varphi}\cos\bar{\varphi}, \tag{B.31}$$

$$\omega_{(\theta)} = \frac{3M-r}{r^2}\left(1-\frac{2M}{r}\right)^{-1/2}\sin\bar{\theta}, \tag{B.32}$$

$$\omega_{(\bar{\varphi})} = -\frac{\cot\theta}{r}\sin^3\bar{\theta}\sin\bar{\varphi}. \tag{B.33}$$

Substituting these relations into equation (B.11), we finally get the conservative form Boltzmann equation in Schwarzschild coordinates:

$$\begin{aligned}
&\left(1-\frac{2M}{r}\right)^{-1/2}\frac{\partial f}{\partial t} + \frac{1}{r^2}\frac{\partial}{\partial r}\left[f\cos\bar{\theta}r^2\left(1-\frac{2M}{r}\right)^{1/2}\right] \\
&+\frac{1}{r\sin\theta}\frac{\partial}{\partial\theta}\left(f\sin\theta\sin\bar{\theta}\cos\bar{\varphi}\right) \\
&+\frac{1}{r\sin\theta}\frac{\partial}{\partial\varphi}\left(f\sin\bar{\theta}\sin\bar{\varphi}\right) \\
&-\frac{1}{\nu^2}\frac{\partial}{\partial\nu}\left[f\nu^3\cos\bar{\theta}\frac{M}{r^2}\left(1-\frac{2M}{r}\right)^{-1/2}\right] \\
&-\frac{1}{\sin\bar{\theta}}\frac{\partial}{\partial\bar{\theta}}\left[f\sin^2\bar{\theta}\frac{r-3M}{r^2}\left(1-\frac{2M}{r}\right)^{-1/2}\right] \\
&-\frac{\partial}{\partial\bar{\varphi}}\left(f\frac{\cot\theta}{r}\sin\bar{\theta}\sin\bar{\varphi}\right) = S_{rad}
\end{aligned} \tag{B.34}$$

The derivative term of frequency ν is the term of the gravitational red/blue shift and thus vanishes when $M = 0$, and that of the angle $\bar{\theta}$ measured from the position vector shows the photon circular orbit by the term $r - 3M$, which means at $r = 3M$ the direction of photons traveling along the sphere $r = 3M$ does never change and thus remain on this sphere.

B.2 Monte-Carlo simulation

Klein-Nishina scattering cross section is described as

$$\frac{d\sigma}{d\Omega} = \frac{r_e}{2}\left(\frac{\lambda}{\lambda'}\right)^2\left[\frac{\lambda}{\lambda'}+\frac{\lambda'}{\lambda}-\sin^2\theta\right], \tag{B.35}$$

$$\lambda' = \lambda + \lambda_e(1-\cos\theta) \tag{B.36}$$

where λ_e is the Compton wavelength of electron, which is equal to $h/m_e c^2$, $r_e = \alpha r_c$ ($\alpha \sim 1/137.036$: the fine structure constant, $r_c = \hbar/m_e c^2$: the reduced Compton wavelength) is the classical electron radius.
Also, we can write down this equation by normalized energy $x = h\nu/m_e c^2$ as

$$\frac{d\sigma}{d\Omega} = \frac{r_e}{2}\left[\left(\frac{1}{1+x(1-\cos\theta)}\right)^3 + \frac{1}{1+x(1-\cos\theta)} - \left(\frac{1}{1+x(1-\cos\theta)}\right)^2 (1-\cos^2\theta)\right]. \tag{B.37}$$

Then, Integrating equation (B.37) over solid angle, we can get a formula below:

$$\begin{aligned}\sigma &= \int \frac{d\sigma}{d\Omega} d\Omega \\ &= \frac{3}{4}\sigma_{\mathrm{T}}\left[\frac{2}{x^2} + \frac{1+x}{(1+2x)^2} + \left(\frac{1}{2x} - \frac{1}{x^2} - \frac{1}{x^3}\right)\log(1+2x)\right].\end{aligned} \tag{B.38}$$

Of course, in the low energy limit $x \to 0$, the total cross section becomes the Thomson cross section $\sigma \to \sigma_{\mathrm{T}} = \frac{8\pi}{3} r_e^2$ (cf. $\log(1+2x) \sim 2x - 2x^2 + 8x^3/3$ $(for\ |x| \ll 1)$).
When considering the electron temperature, because the above equations are correct in electron rest frame, we must rewrite correctly for the normalized frequency in the laboratory frame.
Assuming that $u^\mu = (\Gamma, \Gamma v^i)$ is the electron 4-velocity in the laboratory orthonormal frame, x and x_c are the normalized energy on laboratory and electron rest-frame, respectively, the relation between x and x_c can be written as

$$\begin{aligned}x_c &= xD(\boldsymbol{v}, \boldsymbol{\ell}) \\ &= x\Gamma(1 - \boldsymbol{v}\cdot\boldsymbol{\ell})\end{aligned} \tag{B.39}$$

where $D(\boldsymbol{v}, \boldsymbol{\ell}) \equiv \Gamma(1 - \boldsymbol{v}\cdot\boldsymbol{\ell})$ is the Doppler factor with respect to electron 3-velocity $\boldsymbol{v}$ and the unit vector $\boldsymbol{\ell}$ along to photon 3-momentum. If fixing the scattering electron velocity, we can use equations (B.37) and (B.38) by replacing x with $xD(\boldsymbol{v}, \boldsymbol{\ell})$. When the electrons have some velocity distribution $f(\boldsymbol{p})$ depending on temperature T, we can define so-called "hot cross section" $\sigma_{\mathrm{hot}}(T)$, which includes the velocity dispersion of electrons, by integrating over electron's momentum space:

$$\begin{aligned}\sigma_{\mathrm{hot}} &= \int \sigma f(\boldsymbol{p}) d^3\boldsymbol{p} \\ &= \int d^3\boldsymbol{p} f(\boldsymbol{p}) \frac{3}{4}\sigma_{\mathrm{T}} \times \\ &\left[\frac{2}{(xD(\boldsymbol{p}))^2} + \frac{1+xD(\boldsymbol{p})}{(1+2xD(\boldsymbol{p}))^2} + \left(\frac{1}{2xD(\boldsymbol{p})} - \frac{1}{(xD(\boldsymbol{p}))^2} - \frac{1}{(xD(\boldsymbol{p}))^3}\right)\log(1+2xD(\boldsymbol{p}))\right]\end{aligned} \tag{B.40}$$

Assuming the canonical distribution of relativistic electrons, the distribution function must be proportional to $\exp(-E/k_{\mathrm{B}})$ and $E = \gamma m_e c^2$, then the distribution function can be written by $f = \Xi^{-1}\exp(-\gamma/\theta)$ where Ξ is the normalization factor (or so-called the partition function). Ξ

can be calculated by $\int f d^3\boldsymbol{p} = 1$ as

$$\begin{aligned}
\Xi &= \int \exp(-\frac{\gamma}{\theta}) d^3\boldsymbol{p} \\
&= 4\pi \int_1^\infty \gamma^2 \beta m_e^3 c^3 \exp(-\frac{\gamma}{\theta}) d\gamma && (\because d^3\boldsymbol{p} = m_e^3 c^3 \gamma^2 \beta d\gamma d\Omega) \\
&= 4\pi m_e^3 c^3 \left[\gamma\sqrt{\gamma^2-1}(-\theta)\exp(-\frac{\gamma}{\theta})\right]_1^\infty && (\text{partial integral}) \\
&\quad + 4\pi m_e^3 c^3 \theta \int_1^\infty \left(\sqrt{\gamma^2-1} + \frac{\gamma^2}{\sqrt{\gamma^2-1}}\right) \exp(-\frac{\gamma}{\theta}) d\gamma \\
&= 4\pi\theta m_e^3 c^3 \int_0^\infty \left(\sinh t + \frac{\cosh^2 t}{\sinh t}\right) \exp(-\theta^{-1}\cosh t) \sinh t \, dt && (\gamma = \cosh t) \\
&= 4\pi\theta m_e^3 c^3 \int_0^\infty \cosh 2t \exp(-\theta^{-1}\cosh t) dt \\
&= 4\pi\theta m_e^3 c^3 K_2(\theta^{-1}) && \text{(B.41)}
\end{aligned}$$

where γ, β and θ are the Lorentz factor of the electron, the velocity in the unit of light speed c and the normalized temperature $\theta = k_\mathrm{B}T/m_e c^2$, respectively, the function $K_2(x)$ is the modified Bessel function of the second kind and the modified Bessel function of the α-th kind (but α does not always have to be an integer) can be defined as

$$K_\alpha(x) = \int_0^\infty \cosh \alpha t \exp(-x\cosh t) dt \tag{B.42}$$

and K_α is one of two linearly independent solution of the modified Bessel equation:

$$x^2 \frac{d^2y}{dx^2} + x\frac{dy}{dx} - (x^2+\alpha^2)y = 0. \tag{B.43}$$

After that, we can get the distribution function of canonical relativistic electrons called the Maxwell-Jüttner distribution f_MJ described as

$$f_\mathrm{MJ}(\boldsymbol{p}) = \frac{1}{4\pi m_e^3 c^3 \theta K_2(1/\theta)} \exp(-\frac{\gamma(p)}{\theta}) \tag{B.44}$$

or

$$f_\mathrm{MJ}(\gamma) = \frac{\gamma^2\beta}{\theta K_2(1/\theta)} \exp(-\frac{\gamma}{\theta}) \tag{B.45}$$

B.3 Post-processing by Boltzmann solver

In this section, we introduce the numerical technic and method for chapter 3.

B.3.1 Advection terms

In our simulations, the time interval Δt is determined by the CFL condition for the advection terms. Hereafter, we write each grid in the 5-D real-momentum space by $(r_j, \theta_k, \nu_i, \bar{\theta}_m, \bar{\varphi}_n)$. The grid of the photon frequency is set regularly in the fluid-rest frame for the convenience

of calculating the source term, since the scattering table which we refer to is defined in the fluid-rest frame. Note that the scattering probability depends on the scattering angle and the frequency of an incoming photon in the fluid-rest frame. In contrast, the grid for the direction of the photon propagation ($\bar{\theta}$ and $\bar{\varphi}$) is set regularly not in the fluid-rest frame but in the laboratory frame, since then the advection term can be solved more easily and since the grid regularity in the fluid-rest frame does not facilitate the calculation.

This sort of the grid setting is the same as that adopted by Nagakura et al. (2014). In such a grid setting the grid of frequency in the laboratory frame is different for each grid $(r, \theta, \phi, \bar{\theta}, \bar{\varphi})$ (see Appendix.**??** for more detail). For instance, if two neighboring grids have different fluid velocity, the i-th frequency in the laboratory frame (which corresponds to i-th frequency in the fluid-rest frame, ν_i) is different. This is because the frequency in the laboratory frame depends on the Doppler factor, which is a function of the direction of the photon propagation and the fluid velocity. We thus need to the variable frequency grid into a regular one in the laboratory frame to solve the advection terms.

The numerical procedures can be summarized as below.

1. Interpolate the distribution function in the co-moving regular grid points to obtain the values in the laboratory regular grid points.

2. Calculate numerical fluxes in each direction other than the frequency differential in the laboratory regular grid points.

3. Interpolate the numerical fluxes in the laboratory regular grid to obtain the values in the co-moving regular grid and evaluate the numerical flux in the frequency direction.

4. Update the values of the radiation intensity by using the numerical fluxes obtained in step 3

We explain some technical details for the conversion of the grid points between the laboratory frame and the fluid-rest frame below:
(STEP 1)

When calculating the numerical flux of the advection term [i.e., the left-hand-side of the equation (3.1)], we should keep in mind that photon frequencies are calculated in the fluid-rest frame, while the frequency ν used in the equation (3.1) is evaluated in the laboratory frame. The difficulty resides in the fact that the 2D distribution of the frequency grid and other grid of some quantity, X (either of $r, \theta, \varphi, \bar{\theta}$ or $\bar{\varphi}$) is not in lattice-shaped in the laboratory frame (see figure 7, see also Nagakura et al. 2014). This is because the energy shift by the Doppler effect is a function of all the variables.

Suppose that we solve the numerical flux on the interface at (j+1/2) between the j-th and the $(j+1)$-th cells of some variable X. The number of the regular grids in the laboratory frame (LRG: Laboratory Regular Grid) is set in such a way that each grid point should be in between the neighboring grid in meshes regular in the fluid-rest frame (CRG: Co-moving Regular Grid). If the cell center ν_s in the LRG frame lies between the CRG cells of ν_i and of ν_{i+1} (which we

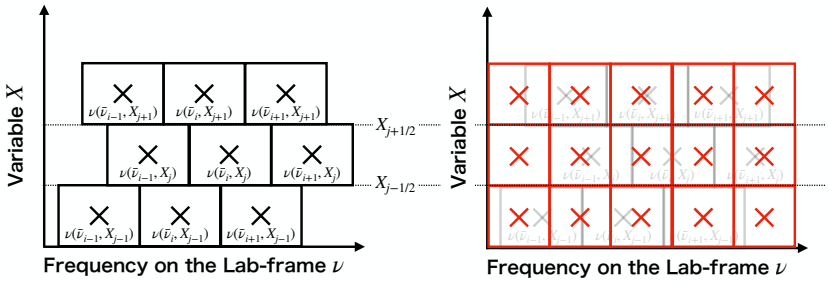

Fig. B.2 Schematic diagrams showing the different 2-D grid distributions, the frequency grid in the horizontal axis vs. that of some other quantity, X, in the vertical axis, in the Co-moving Regular Grid (the black boxes in the left panel) and in the Laboratory Regular Grid (the red boxes in the right panel). The grid distribution is regular in the LRG (right), while is not in the CRG (left).

denote as $\bar{\nu}_i$ and $\bar{\nu}_{i+1}$ in the co-moving frame), the interpolated value, $f_{s,j}$ at ν_s, is calculated by

$$f_{s,j} = f_{i,j} + \frac{f_{i+1,j} - f_{i,j}}{\ln \nu_{i+1} - \ln \nu_i}(\ln \nu_s - \ln \nu_i). \tag{B.46}$$

(STEP 2)

After the interpolation, we calculate the advection terms of each differential, X(other than that of the frequency differential) in the LRG by the 2nd-order up-wind method.

(STEP 3)

The numerical fluxes we obtain in the STEP 2 are those in the LRG frame, however we need to update the distribution function in the CRG frame. Therefore, we should interpolate again now from the LRG frame to the CRG frame. Since the interface of an LRG cell (denoted as s) lies between the two CRG cells i-th and $(i+1)$-th cells), the numerical flux in the X-direction in the s-th cell in the LRG, $F^{j+1/2}_{s,\mathrm{LRG}}$, should be split into these two CRG cells. Here, we define the CRG numerical fluxes in the cell surface $(j+1/2)$, $(j-1/2)$ of the j-th cell of a variable X,$F^{j+}_{i,\mathrm{CRG}}$, are defined as

$$F^{j+}_{i,\mathrm{CRG}} = \sum_{s\in\Lambda^j_i} \frac{\ln \min(\nu_{s+1/2}, \nu^j_{i+1/2}) - \ln \max(\nu_{s-1/2}, \nu^j_{i-1/2})}{\ln \nu^j_{i+1/2} - \ln \nu^j_{i-1/2}} F^{j+1/2}_{s,\mathrm{LRG}} \tag{B.47}$$

$$F^{j-}_{i,\mathrm{CRG}} = \sum_{s\in\Lambda^j_i} \frac{\ln \min(\nu_{s+1/2}, \nu^j_{i+1/2}) - \ln \max(\nu_{s-1/2}, \nu^j_{i-1/2})}{\ln \nu^j_{i+1/2} - \ln \nu^j_{i-1/2}} F^{j-1/2}_{s,\mathrm{LRG}} \tag{B.48}$$

$$\Lambda^j_i = \{s | [\nu^j_{i-1/2}, \nu^j_{i+1/2}] \cap [\nu_{s-1/2}, \nu_{s+1/2}] \neq \emptyset\} \tag{B.49}$$

where the quantity ν^j_i is the frequency in the laboratory frame of the i-th cell of the frequency (which is defined in the comoving frame) and the j-th cell of the variable X. It is notable that the numerical fluxes $F^{j+}_{i,\mathrm{CRG}}$ and $F^{(j+1)-}_{i,\mathrm{CRG}}$ are the flux at the interface at $(j+1/2)$ but are not alway the same, since the numerical fluxes also depend on physical quantities at the cells of

$(i+1,j)$, $(i-1,j)$ etc because of the Doppler (frequency) shift.
(STEP 4)
After calculating the numerical flux in the CRG, we update the primitive value f (distribution function), following the equation,

$$f_{i,j}(t+\Delta t) = f_{i,j}(t) - \frac{\Delta t}{\Delta x_j}(F^{j+}_{i,\mathrm{CRG}} - F^{j-}_{i,\mathrm{CRG}}) \tag{B.50}$$

Note that the grid-based Boltzmann solver inevitably suffers from the incorrectness for the dynamic diffusion problem. Suppose the interacting fluid has a velocity $\boldsymbol{v}$ and the mildly large optical depth τ. In this case, the radiation moves in the same velocity as that of fluid and diffuses by the amount determined by optical depth. This is the dynamic diffusion problem. In the case of the grid-based Boltzmann solver, the limitation of resolution for the direction and the time make difficult to solve correctly the diffusion-advection problem. To avoid this issue, we adopt the method analogous to that described by the equation (34) in **?**, where the numerical flux is made by the combination of numerical flux from the Boltzmann equation and that from the assumption that the radiation moves with the fluid.

B.3.2 Source Term

Although the distribution function should be updated by solving $(1-2M/r)^{-1/2}\partial f/\partial t = S_{\mathrm{rad}}$, evaluating the source term is basically difficult, especially when the Compton scattering process is involved. Because information in the any positions of the 3-D momentum space $(\nu, \bar{\theta}, \bar{\varphi})$ is coupled and entangled with each other unlike the cases with absorptions and/or Thomson (and other elastic) scattering only. In other words, the non-elastic scattering process (e.g. Compton scattering or even Thomson scattering by thermal electrons) can be considered as the flow in the 3-D momentum space of photons, while the elastic scattering (e.g. Thomson scattering by electrons, whose motion is negligibly slow) can be considered as the flow on the constant energy surface, which has a 2-D structure, in the 3-D momentum space of photons. It is thus difficult to integrate the scattering kernel whenever the Compton scattering is effective.

For this reason, we calculate two interaction tables ($S^{\mathrm{abs,scat}}_{i,m,n;i',m',n'}$ and $S^{\mathrm{emit}}_{i,m,n}$) beforehand and update the distribution function by

$$f(\nu_i, \bar{\theta}_m, \bar{\varphi}_n; t+\Delta t) = \sum_{i',m',n'} S^{\mathrm{abs,scat}}_{i,m,n;i',m',n'} f(\nu_{i'}, \bar{\theta}_{m'}, \bar{\varphi}_{n'}; t) + S^{\mathrm{emit}}_{i,m,n}. \tag{B.51}$$

The first term of the right hand side corresponds to that the photons travels from $(\nu_{i'}, \bar{\theta}_{m'}, \bar{\varphi}_{n'})$ to $(\nu_i, \bar{\theta}_m, \bar{\varphi}_n)$ in 3-D momentum space while suffering from the absorption and the scattering. Also, $S^{\mathrm{emit}}_{i,m,n}$ means an increase of the distribution function by the emission. In the following subsections, we introduce how we obtain $S^{\mathrm{abs,scat}}_{i,m,n,i',m',n'}$ and $S^{\mathrm{emit}}_{i,m,n}$.

In this subsection, we omit the subscripts indicating the spatial grid points, since the gas-radiation interaction occurs in a local grid.

Single scattering function

To prepare for numerical calculations we first estimate the single scattering distribution function by the Monte-Carlo simulations, in which we take into account the Compton scattering by thermal electrons and the Klein-Nishina cross-section. These Monte-Carlo simulations provide us with the total cross-section $\kappa_{\rm total}(\nu_{\rm in},\, T_{\rm e})$ and the single scattering distribution function $P_1(\nu_{\rm out}, \Theta, \nu_{\rm in}, T_{\rm e})$ where $\nu_{\rm out}$, Θ, $\nu_{\rm in}$, and $T_{\rm e}$ are the photon frequency after the scattering, the angle between the incoming photon direction and the outgoing photon direction, the frequency of the incoming photon, and the electron temperature.

For a set of $(\nu_{\rm in}, T_{\rm e})$, we perform Monte Carlo simulations, of which the number of injected photons is 10^8, and scattered photons are collected for each $\Delta\Theta = \pi/100$ bin in the range of $0 \le \Theta \le \pi$ and each $\Delta \log h\nu_{\rm out}[{\rm keV}] = 0.055$ bin in the range of $4\times10^{-7} \le h\nu_{\rm out}[{\rm keV}] \le 4\times10^{4}$. We repeat above procedure 200×30 times for each pair of $(\nu_{\rm in}, T_{\rm e})$ in order to cover the range of $4 \times 10^{-7} \le h\nu_{\rm in}[{\rm keV}] \le 4 \times 10^4$ and $10^{-3} \le T_{\rm e}[{\rm keV}] \le 10^3$.

Interaction table for multi-scattering and absorption

Using the single scattering distribution function P_1 obtained above, we produce the table for the multiple scattering and the absorption. The time interval Δt in the present simulations becomes much larger than the scattering timescale in the high-density cells where the multiple scattering intricately changes the distribution function. Thus, we employ sub-time interval, $\Delta t_{\rm scat} (= \Delta t/N)$, for treating multi-scattering more accurately where a controll parameter, N, is fixed to 7 in our simulations. By starting from $\tilde{f}^0 = \delta^i_{i0}\delta^m_{m0}\delta^n_{n0}$ initially, we solve the following equation,

$$
\begin{aligned}
& \tilde{f}^{l+1}(\nu_i, \bar{\theta}_m, \bar{\varphi}_n) \\
= \;& (1 - \phi[\nu_i, \bar{\theta}_m, \bar{\varphi}_n, T, \rho, \boldsymbol{v}, \Delta t_{\rm scat}])(1 - \phi_{\rm abs}[\nu_i, \bar{\theta}_m, \bar{\varphi}_n, T, \rho, \boldsymbol{v}, \Delta t_{\rm scat}])\tilde{f}^l(\nu_i, \bar{\theta}_m, \bar{\varphi}_n) \\
& + \sum_{i',m',n'} \phi([\nu_{i'}, \bar{\theta}_{m'}, \bar{\varphi}_{n'}, T, \rho, \boldsymbol{v}, \Delta t_{\rm scat}])(1 - \phi_{\rm abs}[\nu_{i'}, \bar{\theta}_{m'}, \bar{\varphi}_{n'}, T, \rho, \boldsymbol{v}, \Delta t_{\rm scat}]) \\
& \times P_1(\nu_i, \Theta_{m,n;m',n'}, \nu_{i'}, T)\tilde{f}^l(\nu_{i'}, \bar{\theta}_{m'}, \bar{\varphi}_{n'})\Delta p^3_{i',m',n'} \qquad \text{(B.52)}
\end{aligned}
$$

for $i = 1\text{-}N_\nu$, $m = 1\text{-}N_{\bar{\theta}}$, $n = 1\text{-}N_{\bar{\varphi}}$, where $\tilde{f}$ is the working distribution function, ϕ is the scattering probability function, $\phi_{\rm abs}$ is the absorption probability function, $\Theta_{m,n;m',n'}$ indicates the angle between the photon directions of $(\bar{\theta}, \bar{\varphi}) = (\bar{\theta}_{m'}, \bar{\varphi}_{n'})$ and $(\bar{\theta}_m, \bar{\varphi}_n)$ and the superscript l denotes the number of iteration of the sub time-step. It is notable that scattering/absorption probability depends on the fluid velocity and the direction of the photon propagation. After solving the above equation N times repeatedly, we obtain the table for the multiple scattering and the absorption as $S^{\rm abs,scat}_{i,m,n;i0,m0,n0} = \tilde{f}^N(\nu_i, \theta_m, \phi_n)$ for $i = 1\text{-}N_\nu$, $m = 1\text{-}N_{\bar{\theta}}$, $n = 1\text{-}N_{\bar{\varphi}}$.

By repeating the above procedure $N_\nu \times N_{\bar{\theta}} \times N_{\bar{\varphi}}$ times while changing $(\nu_{i0}, \bar{\theta}_{m0}, \bar{\varphi}_{n0})$, we obtain the full set of the coefficient of $S^{\rm abs,scat}$ in the equation (B.51). This is the table for the multiple scattering and the absorption.

Emission

In the previous subsection, the emitted photons during the time interval $\Delta t_{\rm scat}$ is not considered. The emitted photons are also suffered from the multiple scattering and absorption, so that the coefficient for the emission can be obtained by repeating the following equation N times,

$$\begin{aligned}
&\tilde{f}^{l+1}(\nu_i, \bar{\theta}_m, \bar{\varphi}_n) \\
= \;& (1 - \phi[\nu_i, \bar{\theta}_m, \bar{\varphi}_n, T, \rho, \boldsymbol{v}, \Delta t_{\rm scat}]) \frac{\tilde{f}^l(\nu_i, \bar{\theta}_m, \bar{\varphi}_n) + \kappa_{\rm abs}(\nu_i, \bar{\theta}_m, \bar{\varphi}_n, T, \boldsymbol{v}) \rho \Delta t_{\rm scat} B_\nu(T)}{1 + \kappa_{\rm abs}(\nu_i, \bar{\theta}_m, \bar{\varphi}_n, T, \boldsymbol{v}) \rho \Delta t_{\rm scat}} \\
&+ \sum_{i', m', n'} \phi([\nu_{i'}, \bar{\theta}_{m'}, \bar{\varphi}_{n'}, T, \rho, \boldsymbol{v}, \Delta t_{\rm scat}]) P_1(\nu_i, \Theta_{m,n;m',n'}, \nu_{i'}, T) \\
&\times \frac{\tilde{f}^l(\nu_{i'}, \bar{\theta}_{m'}, \bar{\varphi}_{n'}) + \kappa_{\rm abs}(\nu_{i'}, \bar{\theta}_{m'}, \bar{\varphi}_{n'}, T, \boldsymbol{v}) \rho \Delta t_{\rm scat} B_\nu(T)}{1 + \kappa_{\rm abs}(\nu_{i'}, \bar{\theta}_{m'}, \bar{\varphi}_{n'}, T, \boldsymbol{v}) \rho \Delta t_{\rm scat}} \Delta p^3_{i', m', n'}
\end{aligned} \tag{B.53}$$

for $i = 1\text{-}N_\nu$, $m = 1\text{-}N_{\bar{\theta}}$, $n = 1\text{-}N_{\bar{\varphi}}$ as $S^{\rm emit}_{i,m,n} = \tilde{f}^N(\nu_i, \theta_m, \phi_n)$, where $\kappa_{\rm abs}$ is the opacity for the absorption, B_ν is the Planck function and $\tilde{f}^0$ is set to be zero.

In the present simulations, we investigate the time evolution of f with using the equation (B.51). Performing the Monte-Carlo simulations is needed to produce the table but not required for every step.